Université Hassan 1er
Centre d'Études Doctorales

Faculté des Sciences et Techniques
Settat

THÈSE DE DOCTORAT

Pour l'obtention de grade de Docteur en *chimie*

Formation Doctorale: Chimie Appliquée et Environnement

Spécialité: *Chimie physique et sciences des matériaux*

Sous le thème

Synthesis, structural refinement and spectroscopic study by Raman scattering of new solid solutions $Ba_{2-x}Sr_xMeMO_6$; $0 \leq x \leq 2$ (Me= Ni, Mg, Cd ; M=Mo, W) of double perovskite type.

Présentée par :

EL AAMRANI Moulay Abdelaziz

Soutenue le: *23 décembre 2020*
A la Faculté des Sciences et Techniques de Settat devant le jury composé de :

Pr. Mouhsen Azeddine	**PES**	**FST Settat**	Président
Pr. El MHAMMEDI My Abderrahim	**PES**	**FP Khouribga**	Rapporteur
Pr. BELAOUAD Said	**PES**	**FS Ben M'Sik**	Rapporteur
Pr. IBNLFASSI Amina	**PES**	**FST Settat**	Examinateur
Pr. EL HAIMOUTI Aziz	**PH**	**FP Khouribga**	Examinateur
Pr. MANOUN Bouchaib	**PES**	**FST Settat**	Directeur de thèse

Année Universitaire: 2020/2021

Dedication

This research study is dedicated :

in the memory of my mother *Bia*,

to my father *Ali*,

to my wife *Zineb*,

to my children *Amal* and *Yaâqoub*,

to my brothers and sisters.

Acknowledgements

This thesis has been kept on track and been seen through to completion with support and encouragement of many people. At the end of the thesis I would like to thank all those people who made the thesis possible and an unforgettable experience for me. It is a great pleasure to express my thanks to all those who contributed directly or indirectly towards the success of this study.

First and foremost I am extremely grateful to my great and humble supervisor, Prof. Bouchaib MANOUN for his invaluable advice, continuous support, and patience during my PhD study. His immense knowledge and plentiful experience have encouraged me in all the time of my academic research and daily life. This thesis would not have been possible without his help.

I acknowledge my gratitude to the Department of Earth Sciences at Uppsala University, Sweden for the absolute support to the thesis. Special thanks to Peter Lazor for giving us the absolute access to the Raman spectrometer and for his technical assistance.

I acknowledge my gratitude to the “Centre Régional d’Analyses et de Caractérisation (CRAC)” at University Hassan 1 for the absolute support to the thesis and for giving us the absolute access to the “D2 PHASER” diffractometer.

I thank also M. El MHAMMEDI My Abderrahim, M. BELAOUAD Said and M. SAAD Elmadani who agreed to correct my report thesis and to be protractor. Also my sincere thanks to Mouhsen Azeddine who agreed to be chairman of the defense, and Mrs. IBNLFASSI Amina and M. EL HAIMOUTI Aziz who agreed to be thesis examiners.

I would like to thank my friends, lab mates, colleagues and research team Y. TAMRAOUI, F. MIRINOUI, A. ELHACHMI, R. ABKAR, R. HALOUI and S. LOUIHI for a cherished time spent together in the lab, and in social settings. My appreciation also goes out to my friends for their encouragement and support all through my studies.

Special thanks go to my family for their love and continued support throughout my academic research. My mother who, if she was still with us, would be so proud of her son. My father he's always been there to support me, to give me a push when I needed it, and most importantly, to listen. My wife, my children, my brothers and sisters, always provided extra encouragement towards completion of my career goals.

Abstract

The double-perovskite oxides of general formula AA'MM'O_6, in which A and A' are rare earth metal and M and M' are transition metal cations, constitute a wide family of materials displaying varied and appealing properties. Three key features are the basis of the intensification of studies on these compounds: their technological importance which is mainly related to the properties that characterize them, the discovery for some of them the colossal magnetoresistance effect and the fact that all the metallic elements of the periodic table are stable in a perovskite. These major elements have further widened the field of studies which are interested in perovskite materials and their properties and made of these materials real attractors of researchers.

The main objective of this thesis work was based on the synthesis, characterization, structural determination and study of phase transitions induced by the composition and temperature of new solid solutions $Ba_{2-x}Sr_xMeMO_6$; (Me= Ni, Mg, Cd; M=Mo, W and $0 \leq x \leq 2$) of double perovskite type. The samples were prepared in polycrystalline form by thermal treatment, in air. Their crystal structures have been investigated using X-ray diffraction technique, Rietveld refinement and Raman spectroscopy.

As a function of composition, the samples exhibit a sequence of phase transitions, in the intervals shown in the following table:

	$Ba_{2-x}Sr_xNiMoO_6$	$Ba_{2-x}Sr_xMgMoO_6$	$Ba_{2-x}Sr_xCdWO_6$
Fm-3m → I4/m	1,3 < x < 1,5	0.9 < x < 1	0.6 < x < 0.8
I4/m → I2/m	1,8 < x < 2	1.5 < x < 1.75	1 < x < 1.2
I2/m → $P2_1/n$	xxxxxxxxxx	xxxxxxxxxx	1.6 < x < 1.8

The study by high temperature Raman spectroscopy of $Ba_{2-x}Sr_xMeMoO_6$; (Me= Ni, Mg and $0 \leq x \leq 2$) has shown a sequence of phase transitions, whose symmetry increases with temperature, as indicated in the table below

	$Ba_{2-x}Sr_xNiMoO_6$				$Ba_{2-x}Sr_xMgMoO_6$			
X	1,5	1,6	1,8	2	1	1,5	1,75	2
I4/m → Fm-3m	130°C	190°C	334°C	474°C	105°C	395°C	436°C	466°C
I2/m → I4/m	xxxx	xxxx	xxxx	175°C	xxxx	xxxx	96°C	205°C

Keywords: *doubles perovskites oxides, phase transition, Rietveld refinement, X-ray diffraction, temperature Raman spectroscopy.*

Résumé

Les oxydes de double pérovskite de formule générale $AA'MM'O_6$, dans lesquels A et A' sont des terres rares et M et M' sont des cations de métaux de transition, constituent une large famille de matériaux ayant des propriétés variées et attrayantes. Trois éléments clés sont à la base de l'intensification des études sur ces composés: leur importance technologique qui est principalement liée aux propriétés qui les caractérisent, la découverte pour certains de l'effet de magnétorésistance colossal et le fait que tous les éléments métalliques du tableau périodique sont stables dans une pérovskite. Ces éléments majeurs ont encore élargi le champ des études qui s'intéressent aux matériaux pérovskites et à leurs propriétés et ont fait de ces matériaux de véritables attracteurs de chercheurs.

L'objectif principal de ce travail de thèse était basé sur la synthèse, la caractérisation, la détermination structurale et l'étude des transitions de phase induites par la composition et par la température de nouvelles solutions solides $Ba_{2-x}Sr_xMeMO_6$; (Me = Ni, Mg, Cd; M = Mo, W et $0 \leq x \leq 2$) de type doubles pérovskites. Les échantillons ont été préparés sous forme polycristalline par traitement thermique à l'air. Leurs structures cristallines ont été étudiées en utilisant la technique de diffraction des rayons X, l'affinement de Rietveld et la Spectroscopie Raman.

En fonction de la composition, les échantillons présentent une séquence de transitions de phases dans les intervalles indiqués dans le tableau suivant:

	$Ba_{2-x}Sr_xNiMoO_6$	$Ba_{2-x}Sr_xMgMoO_6$	$Ba_{2-x}Sr_xCdWO_6$
Fm-3m → I4/m	1,3 < x < 1,5	0.9 < x < 1	0.6 < x < 0.8
I4/m → I2/m	1,8 < x < 2	1.5 < x < 1.75	1 < x < 1.2
I2/m → $P2_1/n$	xxxxxxxxxx	xxxxxxxxxx	1.6 < x < 1.8

L'étude par spectroscopie Raman à haute température de $Ba_{2-x}Sr_xMeMoO_6$; (Me = Ni, Mg et $0 \leq x \leq 2$) a montré une séquence de transitions de phases, dont la symétrie augmente avec la température, comme indiqué dans le tableau ci-dessous

	$Ba_{2-x}Sr_xNiMoO_6$				$Ba_{2-x}Sr_xMgMoO_6$			
X	1,5	1,6	1,8	2	1	1,5	1,75	2
I4/m → Fm-3m	130°C	190°C	334°C	474°C	105°C	395°C	436°C	466°C
I2/m → I4/m	xxxx	xxxx	xxxx	175°C	xxxx	xxxx	96°C	205°C

Mots clés: *doubles pérovskites, transition de phase, diffraction des rayons X, spectroscopie Raman, affinement Rietveld*

Table of Contents

Part 2

Results

Figures list

Figure II.7 Illustration of a complete Raman spectra and the three possible modes of scattering during excitation by a monochromatic light source (E = energy level, G.s. = Ground state, Vib.s. = Vibrational state, Vir.s. = Virtual state).

Figure II.8: A schematic diagram of the experimental spectrometer installation

Figure II.9: Real installation of the Raman spectroscopic system

Figure III.1: X-ray powder diffraction patterns for $Ba_{2-x}Sr_xNiMoO_6$ ($0 \leq x \leq 2$). The star corresponds to the most intense reflection of the minor impurity. The Enlarged sections show the evolution of the basic (400), (422), (440) and (620) reflections.

Figure III.2: X-ray powder diffraction patterns for $Ba_{2-x}Sr_xMgMoO_6$ ($0 \leq x \leq 2$). The star corresponds to the most intense reflection of the minor impurity. The Enlarged sections show the evolution of the basic (400), (422), (440) and (620) reflections.

Figure III.3: Variation of the lattice parameters as a function of composition for the series $Ba_{2-x}Sr_xNiMoO_6$ (up) and $Ba_{2-x}Sr_xMgMoO_6$ (down). The *a* and *b* values in the tetragonal and monoclinic cells have been multiplied by $2^{1/2}$ for clarity. The cubic to tetragonal transition is observed between x = 1.3 and x = 1.5 for the series $Ba_{2-x}Sr_xNiMoO_6$ and between x = 0.9 and x = 1 for the series $Ba_{2-x}Sr_xMgMoO_6$, while the tetragonal to monoclinic transition is observed between x = 1.8 and x = 2 and between x = 1.5 and x = 1.75 for the series $Ba_{2-x}Sr_xNiMoO_6$ and $Ba_{2-x}Sr_xMgMoO_6$ successively.

Figure III.4-a: Final Rietveld plots for compounds $Ba_{2-x}Sr_xNiMoO_6$; $0 \leq x \leq 1.3$ (Fm-3m). The upper symbols illustrate the observed data (circles) and the calculated pattern (solid line). The vertical markers show calculated positions of Bragg reflexions. The lower curve is the difference diagram. (1/5)

Figure III.4-b: Final Rietveld plots for compounds $Ba_{2-x}Sr_xMgMoO_6$; $0 \leq x \leq 0.9$ (Fm-3m). The upper symbols illustrate the observed data (circles) and the calculated pattern (solid line). The vertical markers show calculated positions of Bragg reflexions for $Ba_{2-x}Sr_xMgMoO_6$ (up) and for the minor impurity $BaMoO_4$ (down). The lower curve is the difference diagram. (2/5)

Figure III.4-c: Final Rietveld plots for compounds $Ba_{2-x}Sr_xNiMoO_6$; $1.5 \leq x \leq 1.8$ (I4/m). The upper symbols illustrate the observed data (circles) and the calculated pattern (solid line). The vertical markers show calculated positions of Bragg. The lower curve is the difference diagram. (3/5)

Figure III.4-d: Final Rietveld plots for compounds $Ba_{2-x}Sr_xMgMoO_6$; $1 \leq x \leq 1,5$ (I4/m). The upper symbols illustrate the observed data (circles) and the calculated pattern (solid line). The

vertical markers show calculated positions of Bragg reflexions. The lower curve is the difference diagram. (4/5)

Figure III.4-e: Final Rietveld plots for compounds Sr_2NiMoO_6 (I2/m) (up- left) and $Ba_{2-x}Sr_xMgMoO_6$; $1,75 \leq x \leq 2$ (I2/m). The upper symbols illustrate the observed data (circles) and the calculated pattern (solid line). The vertical markers show calculated positions of Bragg reflexions. The lower curve is the difference diagram. (5/5)

Figure III.5: The typical polyhedral arrangement, the Ba/Sr environment and illustrations of the effect of tilting of the MoO_6, NiO_6 and MgO_6 octahedra in the different space group structure in $Ba_{2-x}Sr_xMeMoO_6$ (Me=Ni, Mg and $0 \leq x \leq 2$).

Figure III.6: Observed tolerance factor (obtained from the distances obtained from the Rietveld refinements) as a function of the strontium amount in $Ba_{2-x}Sr_xNiMoO_6$ ($0 \leq x \leq 2$) (up) and $Ba_{2-x}Sr_xMgMoO_6$ ($0 \leq x \leq 2$) (down).

Figure III.7: Raman spectra of $Ba_{2-x}Sr_xNiMoO_6$; $0 \leq x \leq 2$ (up) and $Ba_{2-x}Sr_xMgMoO_6$; $0 \leq x \leq 2$ (down) recorded at ambient conditions.

Figure III.8: Correlations diagrams for the Raman-active vibrations in the monoclinic (I2/m), the tetragonal (I4/m) and the cubic (Fm-3m) phases of $Ba_{2-x}Sr_xMeMoO_6$; $0 \leq x \leq 2$ (Me=Ni,Mg).

Figure III.9: Evolution of the 140 cm^{-1}, 445 cm^{-1}, 550 cm^{-1} and 800 cm^{-1} Raman mode as a function of the strontium amount in $Ba_{2-x}Sr_xNiMoO_6$ ($0 \leq x \leq 2$) materials.

Figure III.10: Evolution of the 130 cm^{-1}, 440 cm^{-1} and 800 cm^{-1} Raman mode as a function of the strontium amount in $Ba_{2-x}Sr_xMgMoO_6$ ($0 \leq x \leq 2$) materials.

Figure III.11: Evolution of the Intensity and the FWHM for 800cm^{-1} modes of $Ba_{2-x}Sr_xNiMoO_6$ and $Ba_{2-x}Sr_xMgMoO_6$ successively, as a function of the strontium amount in the compositions.

Figure III.12: The Raman spectra of $Ba_{2-x}Sr_xNiMoO_6$ (x=1,5; x=1,6; x=1,8 and x=2) obtained for selected temperatures, as indicated.

Figure III.13: Enlargement and discontinuous alteration of the slope of the Raman modes centered at 800cm^{-1} illustrating the phase transitions of $Ba_{2-x}Sr_xNiMoO_6$ (x=1,5; x=1,6; x=1,8 and x=2).

Figure III.14: Raman modes for 550 cm^{-1} and 800 cm^{-1} modes and the intensity ratio I_{800}/I_{550} of $Ba_{0.5}Sr_{1.5}NiMoO_6$ and Raman modes for 445 cm^{-1} and 800 cm^{-1} modes and the FWHM for 800cm^{-1} modes of $Ba_{0.4}Sr_{1.6}NiMoO_6$, as a function of temperature.

Figure III.15: Raman modes for 800 cm^{-1} and the FWHM for 550cm^{-1} modes of $Ba_{0.2}Sr_{1.8}NiMoO_6$ and Raman modes for 550 cm^{-1} and the intensity ratio I_{800}/I_{550} of Sr_2NiMoO_6, as a function of temperature.

Figure III.16: Transition temperature as a function of the composition of strontium in $Ba_{2-x}Sr_xNiMoO_6$.

Figure III.17: The Raman spectra of $Ba_{2-x}Sr_xMgMoO_6$ (x=1, x=1,5, x=1,75 and x=2) obtained for selected temperatures, as indicated.

Figure III.18: Enlargement and discontinuous alteration of the slope of the Raman modes centered at 440 cm^{-1} and 800cm^{-1} and illustrating the phase transitions of $Ba_{2-x}Sr_xMgMoO_6$ (x=1, x=1,5, x=1,75 and x=2).

Figure III.19: Raman modes, the mode ratio, the intensity ratio and the FWHM of $Ba_{2-X}Sr_XMgMoO_6$ (x=1 and x=1,5), as a function of temperature.

Figure III.20: Raman modes, Ratio Raman mode, and the FWHM of $Ba_{2-X}Sr_XMgMoO_6$ (x=1,75 and x=2), as a function of temperature.

Figure III.21: Transition temperature as a function of the composition of strontium in $Ba_{2-x}Sr_xMgMoO_6$.

Figure IV.1: X-ray powder diffraction patterns for $Ba_{2-x}Sr_xCdWO_6$ ($0 \leq x \leq 2$). The Enlarged sections show the evolution of the basic (400), (422), (440) and (620) reflections.

Figure IV.2: Variation of the lattice parameters as a function of composition for the series $Ba_{2-x}Sr_xCdWO_6$. The *a* and *b* values in the tetragonal and monoclinic cells have been multiplied by $2^{1/2}$ for clarity. The cubic to tetragonal transition is observed between x=0.6 and x=0.8, the tetragonal to monoclinic I2/m transition is observed between x=1 and x=1.2, while the monoclinic I2/m to monoclinic $P2_1/n$ is observed between x=1.6 and x=1.8.

Figure IV.3: Variation of the volume of the cell with increasing strontium concentration in the studied composition range in $Ba_{2-x}Sr_xCdWO_6$ ($0 \leq x \leq 2$).

Figure IV.4: Final Rietveld plots for compounds $Ba_{2-x}Sr_xCdWO_6$. The upper symbols illustrate the observed data (circles) and the calculated pattern (solid line). The vertical

markers show calculated positions of Bragg reflections. The lower curve is the difference diagram. (1/3)

Figure IV.4: Final Rietveld plots for compounds $Ba_{2-x}Sr_xCdWO_6$. The upper symbols illustrate the observed data (circles) and the calculated pattern (solid line). The vertical markers show calculated positions of Bragg reflections. The lower curve is the difference diagram. (2/3)

Figure IV.4: Final Rietveld plots for compounds $Ba_{2-x}Sr_xCdWO_6$. The upper symbols illustrate the observed data (circles) and the calculated pattern (solid line). The vertical markers show calculated positions of Bragg reflections. The lower curve is the difference diagram. (3/3)

Figure IV.5: Illustrations of the tilting and rotation effect of the $(Cd/W)O_6$ octahedra for tetragonal and monoclinic symmetries (b, c and d) in $Ba_{2-x}Sr_xCdWO_6$ ($0 \leq x \leq 2$).

Figure IV.6: Observed tolerance factor (calculated from the distances obtained from the Rietveld refinements) as a function of the strontium amount in $Ba_{2-x}Sr_xCdWO_6$ ($0 \leq x \leq 2$).

Tables list

Table IV.3: Details of Rietveld refinement conditions of the monoclinic (I2/m and $P2_1/n$) compositions in $Ba_{2-x}Sr_xCdWO_6$ ($1.2 \leq x \leq 2$).

Table IV.4: Positional and thermal parameters of the cubic and tetragonal compositions in $Ba_{2-x}Sr_xCdWO_6$ ($0 \leq x \leq 1$) after Rietveld refinement from XRD data collected at room temperature.

Table IV.5: Positional and thermal parameters of the monoclinic compositions in $Ba_{2-x}Sr_xCdWO_6$ ($1.2 \leq x \leq 2$) after Rietveld refinement from XRD data collected at room temperature.

Table IV.6: Selected inter-atomic distances (Å) and [O-W-O] angles (°) for the cubic compositions in $Ba_{2-x}Sr_xCdWO_6$ ($0 \leq x \leq 0.6$) series at room temperature.

Table IV.7: Selected inter-atomic distances (Å) and [O-W-O] angles (°) for the tetragonal compositions in $Ba_{2-x}Sr_xCdWO_6$ ($0.8 \leq x \leq 1$) series at room temperature.

Table IV.8: Selected inter-atomic distances (Å) and [O-W-O] angles (°) for the monoclinic I2/m compositions in $Ba_{2-x}Sr_xCdWO_6$ ($1.2 \leq x \leq 1.6$) series at room temperature.

Table IV.9: Selected inter-atomic distances (Å) and [O-W-O] angles (°) for the monoclinic $P2_1/n$ compositions in $Ba_{2-x}Sr_xCdWO_6$ ($1.8 \leq x \leq 2$) series at room temperature.

Figure IV.7: Raman spectra of $Ba_{2-x}Sr_xCdWO_6$ ($0 \leq x \leq 2$) recorded at ambient conditions.

Figure IV.8: Enlargement of the modes centered at 135 cm^{-1} for the monoclinic symmetries I2/m and $P2_1/n$ (a) and discontinuous alteration of the slope of the modes centered at 435cm^{-1} corresponding to the phase transitions (b).

Figure IV.9: Raman modes (a) and Intensity of the modes centered at 435cm^{-1} (b), the FWHM of the modes centered at 845 cm^{-1} (c) and Intensity ratio I_{800}/I_{130} (d) as a function of the composition x of $Ba_{2-x}Sr_xCdWO_6$ ($0 \leq x \leq 2$). The symmetry transition shows considerable changes in composition dependence of the modes.

General introduction

Although certain properties of materials have been known since antiquity, others have attracted increased scientific and commercial attention in recent years because of their important applications in various fields. In this framework, and since the discovery of certain important properties such as: the colossal magnetoresistance phenomena, superconductivity, ferromagnetism, magnetic frustration, catalytic activity, ionic conductivity [1] ... etc, perovskite materials have aroused a major interest due to their multiple uses and their technological importance which is mainly related to the properties that characterize them. It should also be noted that all the metallic elements of the periodic table are stable in a perovskite; this has further widened the field of studies which are interested in perovskite materials and their properties and made of these materials real attractors of researchers.

Seen the practical interests that these compounds could present, studies to understand and improve their properties are conducted around the world. Thus, the existence of a large number of compounds with this structure on the one hand, and the fact that this one offer an unlimited possibility of insertion and substitution of chemical elements on the other hand, led to members of the double perovskite family exhibiting a wide range of fascinating properties [1, 2]. Consequently, many double perovskites have been synthesized and studied in the last five decades.

It is important to note that, the properties of perovskites are linked to subtle structural variations, for example, tilts and octahedral deformations and the partial cation ordering affecting the electronic properties such as conductivity, magnetism and certain dielectric properties [3]. Indeed, knowing the correct crystal structure for a compound is vital to understanding its properties. For this reason, optimizing the properties of perovskites require precise control of the structural variations.

In virtue of their properties, the perovskites form a class of materials of great technological value in many application areas: monitoring and security piezoelectric devices, piezoelectric sonars, multilayer capacitor, waveguide modulators, non-volatile memories, random access memories (DRAM), radiocommunication, ultrasonic sensors, multilayer capacitor, High TC superconductor ... etc.

In the light of the above considerations, considerable interest has been given in recent years to double perovskites of the type $A_2BB'O_6$ (B = Ni, Co, Fe, Zn ...; B' = W, Mo, Te ...).

We focused during this work on the elaboration of the new compounds of type $A_2BB'O_6$ of double perovskite structure and of formula $Ba_{2-x}Sr_xMeMO_6$ (Me=Ni, Mg, Cd ; M=Mo, W and

$0 \leq x \leq 2$). We paid particular attention to obtaining single-phase polycrystalline compounds. The structural characterization of the compounds obtained was carried out by the X-ray powder diffraction technique at the research center of Faculty of Science and Technology of Settat Morocco and by Raman spectroscopy in collaboration with the laboratory of Earth Sciences, Uppsala University Sweden.

This Memoir is divided into four chapters;

The first chapter will be devoted to a bibliographical review on the physical and structural properties of perovskites, in particular, the double perovskites of type $A_2BB'O_6$.

In a second chapter, we describe the synthesis of samples, the experimental techniques, the different structural characterization method and the corresponding material used in this study.

The third chapter is dedicated to describe the crystal structure and the composition and temperature induced structural phase transitions in new series of double perovskites $Ba_{2-x}Sr_xMeMoO_6$ ($0 \leq x \leq 2$), (Me= Ni and Mg).

In chapter 4, we will present the structural results obtained by X-ray diffraction and by Raman spectroscopy at the ambient of new solid solutions $Ba_{2-x}Sr_xCdWO_6$ ($0 \leq x \leq 2$), as well as the structural phase transitions induced by chemical composition in these double perovskite.

Finally, a general conclusion will summarize all the results and thereby paving the way for some prospects for further studies.

References:

[1] R.H. Mitchell, Perovskites Modern and Ancient, Almaz Press, Ontario, 2002.

[2] M.T. Anderson, K.B. Greenwood, G.A. Taylor, K.R. Poeppelmeier, Prog. Solid State Chem. 22 (1993) 197-233.

[3] P.A. Cox, Transition Metal Oxides: An Introduction to Their Electronic Structure and Properties, Clarendon Press, Oxford, 1992.

Chapter I

General presentation of perovskites

In this chapter we will present a brief review of the principal characteristics of the simple and double perovskites: crystal structure, order/disorder configuration, distorted structures and ordering properties.

1- Composition of perovskite-type oxide

Perovskites form a large family of crystalline materials whose name comes from a natural mineral: calcium titanate ($CaTiO_3$). This mineral was discovered and named by Gustav Rose in 1839, in honor of a Russian mineralogist, Count Lev Aleksevich von Perovski [1].

Perovskites have as general formula ABX_3, where A is an alkaline, an alkaline earth or a rare earth, B is a transition metal and X is oxygen, sulfur or halogen. There are two main types of perovskite materials:

- The simple perovskites, for which sites A and B are occupied by a single type of cation, such as $SrTiO_3$, $BaTiO_3$, $LaNiO_3$, $LaMnO_3$...
- The complex perovskites, where the A and/or B sites are simultaneously occupied by at least two different cations, as for the compositions $Ca_{1/4}Cu_{3/4}MnO_3$, $CaFeTi_2O_3$, $(Ba_{1-x}Ca_x)(Ti_{1-y}Zr_y)O_3$, $Ba_{2-x}Sr_xMgTeO_6$, $Sr_{3-x}Ca_xFe_2TeO_9$... This category includes solid solutions between several compounds with perovskite structure (simple or complex) such as $(Ba_2CaWO_6)_{1-x}(Sr_2CaWO_6)_x$.

2- The crystal structure of perovskite

2.1- Basic ABO_3-type perovskites

The typical crystalline cell of a simple perovskite has a cubic symmetry in the space group $Pm\bar{3}m$ (space group N° 221 in the international crystallographic tables), with the parameter $a_p \approx 4$ Å. The $SrTiO_3$ compound is often described as the archetype of cubic perovskites. However, a large number of exceptions are known, they present neighboring structures more or less distorted. Several effects can be at the origin of these deformations, inter alia, that due to the difference of the ionic rays of the cations A and B (disagreement between the two sub-lattices AO and BO) or the one due to deformations possible of octahedra, such as the Jahn-Teller effect.

In perovskite-type oxides the A-cations, usually bigger than the B-site cations, are surrounded by twelve oxygen anions in a cubo-octahedral arrangement and occupy the space between the corner sharing BO_6 octahedra. Depending on the choice of origin, it is possible to describe the ideal crystal cell of a simple perovskite in two ways. In the first (Fig. I.1-a), the cation A is located in the position 1a(0, 0, 0), the cation B in the center of the cube, in the

position 1b(1/2, 1/2, 1/2), and the oxygen is placed in the middle of each face in the position 3c(0, 1/2, 1/2). In the second description (Fig. I.1-b), the origin is displaced by a vector (1/2, 1/2, 1/2), thus, A occupies the position 1b(1/2, 1/2, 1/2), B the position 1a(0, 0, 0), while the oxygen is placed in the middle of each side in the position 3d(0, 0, 1/2).

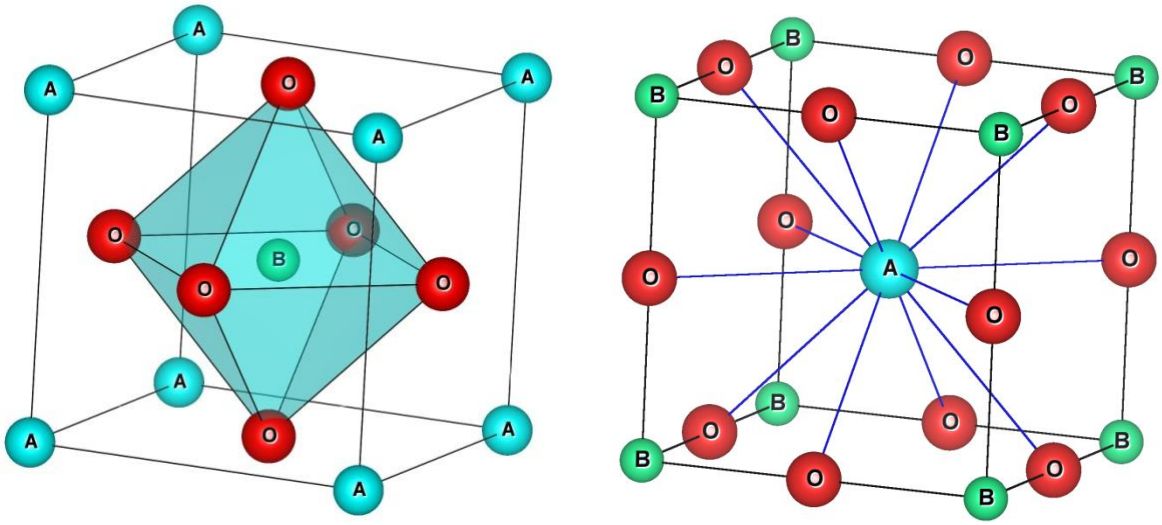

Figure I.1: Two depictions of the unit cell of the ideal cubic perovskite structure ABO_3 highlighting the A-site cation environment: **a** (right) and the B-site cation environment: **b** (left).

2.2- Double perovskite

The perovskite lattice is a very compact set that does not allow the formation of interstitial compositions. However, complicating the possible structures of perovskites is the observation that two or more cations may share the A- or B-sites [2]. When sites A and/or B are simultaneously occupied by at least two different cations we obtain double perovskites of general formula $AA'BB'O_6$ (Fig. I.2), where the cations A and A' and the cations B and B' may be of the same type or of a different type.

In the case of a random distribution of the cations (A, A') and / or (B, B'), no superlattice is observed. Conversely, ordering the cations (A, A') and / or (B, B') leads to a superlattice. Generally, there are three possible patterns of arrangements for either the A- or B-site cations in double perovskites: Layered, first found to be adopted by La_2CuSnO_6 [3], Columnar and Rock Salt. These three types of ordering correspond to interleaving planes of different cations along the crystallographic directions in the perovskite unit cell along [001], [110] and [111] respectively.

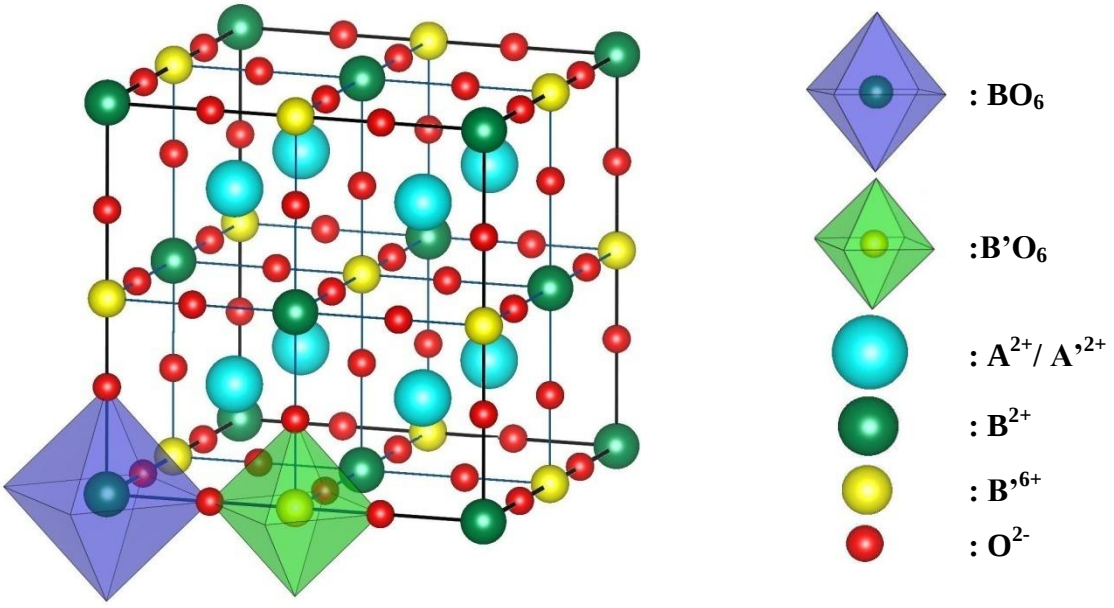

Figure I.2: Schematic representation of the $AA'BB'O_6$ ideal double perovskite structure.

In double perovskites, the cations of A- and A'-sites have the tendency to occur in a layered fashion, rather than in the rock salt pattern commonly observed for B- and B'-sites cations [4] (Figure I.3). Generally, for all these arrangements, ordering of the cations is favored when there is a significant difference in size and/or charge of the cations [5]. Indeed, the establishment of an order in the octahedral sites, is favored when the difference of the charges of the ions B and B' is greater than or equal to four [6, 7]. However, the difference in charges alone is not enough for the cations to be in order, the case of perovskite Ba_2NbFeO_6 where the Nb^{5+} (0.64Å) and Fe^{3+} (0.64Å) cations are disordered [8].

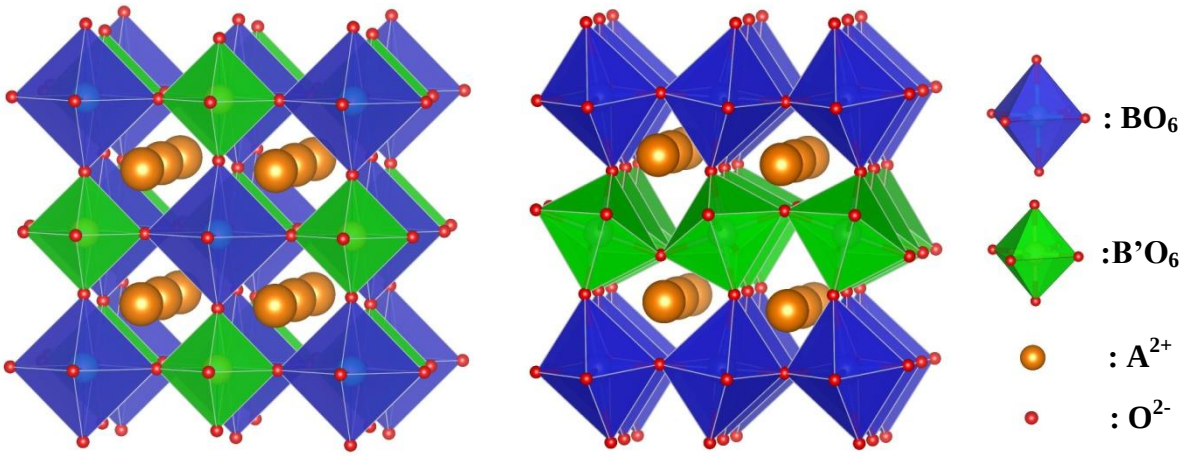

Figure I.3: The two most frequents types of ordering in $A_2BB'O_6$ perovskites; the variant of the rock salt ordered structure (left) and the layered ordering (right).

3- Distorted perovskites

The perovskite structure, of cubic symmetry in the ideal case, often presents deformations which can have an effect on the physical properties. Three mechanisms can be at the origin of these deformations: octahedral tilting, distortions in the length of the BO_6 octahedral bonds and B-cations displacements within the octahedra [9, 10]. All of these distortions occur to achieve the best possible compromise between the bonding requirements of the A- and B-site cations and thereby attain the structure with the lowest possible energy. These distortions lead to the formation of phases with lower symmetry. It should be noted that a simple geometric analysis makes it possible to quantify the phenomena mentioned above, and thus to predict the deformation of the perovskite structure with respect to the ideal structure.

Considering the ions as rigid spheres (Figure I.4), it is possible, in an ideal perovskite structure, to link the parameter of the unit cell to the ionic rays of the A, B and O atoms.

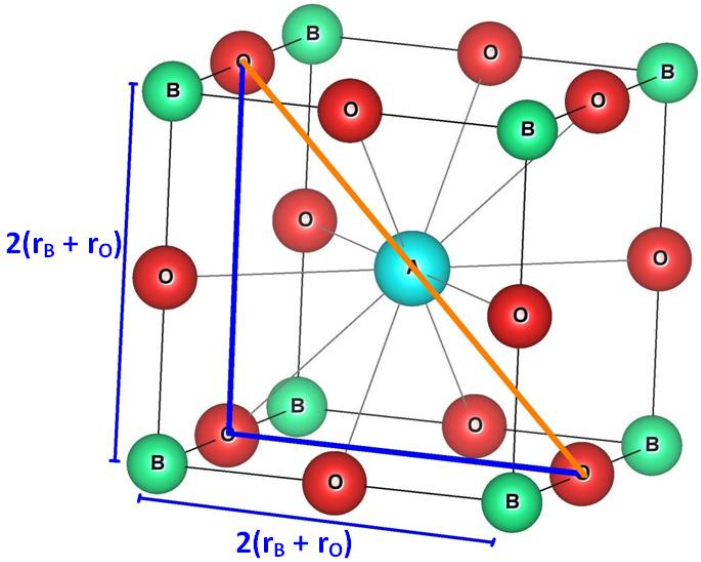

Figure I.4: Unit cell of the ABO_3 ideal double perovskite structure

For the right-angled triangle marked in the figure I.4 with thick lines, we can write:

$$2.[2.(r_B + r_O)]^2 = [2.(r_A + r_O)]^2 \quad \text{(I-1)}$$

$$\sqrt{2}.(r_B + r_O) = (r_A + r_O) \quad \text{(I-2)}$$

Where r_A, r_B and r_O are respectively the ionic radii of the atoms A (in coordination 12), B (in coordination 6) and O, given by Shanon and Prewitt [11] - [13].

In the cubic structure, the ratio $\frac{(r_A + r_O)}{\sqrt{2}.(r_B + r_O)}$ is worth 1.

On the basis of this geometric analysis, Goldschmit defined the tolerance factor t (Goldschmit factor), as [14]:

$$t = \frac{(r_A + r_O)}{\sqrt{2}.(r_B + r_O)} \quad \text{(I-3)}$$

The deviation of t from its ideal value (t = 1) signifies a distortion of the cubic structure, this is true for simple perovskites as for double perovskites. In the latter case, considering a double perovskite of general formula $AA'BB'O_6$, r_A and r_B are replaced in the preceding formula by the average value of the cationic radii (A and A') and (B and B') successively. The equation of the tolerance factor becomes as follows:

$$t = \frac{\frac{(r_A + r_{A'})}{2} + r_O}{\sqrt{2}.(\frac{r_B + r_{B'}}{2} + r_O)} \quad \text{(I-4)}$$

Moreover, in the case of double perovskites with substitution in the A and/or B site, for example: $A_{\alpha-x}A'_xBB'O_6$ ($0 \leq x \leq \alpha$), the percentage of the A and A' cations in the structure must be taken into consideration. Indeed, the tolerance factor can be written as:

$$t = \frac{\frac{[(\alpha - x).r_A + x.r_{A'}]}{2} + r_O}{\sqrt{2}.(\frac{r_B + r_{B'}}{2} + r_O)} \quad \text{(I-5)}$$

Given that this factor, however, is only an indicator and does not definitively know whether a perovskite lattice will form or not. It is therefore necessary to go through the experience, as other space filling restrictions should also be considered [15,16] such as the stability of the $B/B'O_6$ octahedra.

It should be noted, moreover, that the definition of tolerance factor given above is theoretical, the experimental approach of this definition, called: observed tolerance factor «t_{obs}», is defined by replacing the appropriate ionic radii of A/A', B/B', and O ions tabulated by Shannon in the theoretical tolerance factor formula, by $d_{(A/A'-O)}$ and $d_{(B/B'-O)}$, the average

atomic distances obtained experimentally (via the structure refinement software) between the A/A' and B/B' atoms respectively and the nearest oxygen neighbors that belong to the $A/A'O_{12}$ and $B/B'O_6$.

As we already pointed out above, the deviation of t from its ideal value (t = 1) signifies a distortion of the cubic structure. Indeed, according to the value of the tolerance factor, we can distinguish several situations, shown in the following table:

Table I.1: Evolution of crystalline structures as function the tolerance factor value [17].

t<0.75 Ilmenite	**0.75<t<1.06** Perovskite			**t>1.06** Hexagonal
	0.75<t<0.95 Orthorhombic distortion	0.96<t<0.99 Rhombohedric distortion	0.99<t<1.06 Cubic	

4- Distorted Perovskite classification

The decrease in the symmetry in the perovskite structure (i.e. when the value of t exceeds the interval of stability of cubic symmetry, Table I.1), is related to the ratio of the volume between the A and B cations and the cuboctahedral and octahedral sites successively. Two cases are to envisage:

- If t > 1.06, the cuboctahedral site is totally occupied by the cation A, while the octahedral site is partially occupied due to the smaller size of cation B. Therefore, the latter moves in its site with a view to reduce the length of some B-O bonds and decrease its coordination, thus causing a distortion in the perovskite framework [18].
- If t < 0,99, by contrast to the previous situation, the octahedral site is totally occupied by the cation B, while the cuboctahedral site is partially occupied due to the smaller size of cation A. Consequently, in order to minimize the length of some A-O bonds and thus reduce the coordination of A, two phenomena can be observed: the tilting of BO_6 octahedra around the pseudo-cubic axes and/or the displacement of the cations A in their sites AO_{12} so that it is no longer necessary for the lengths of the A-O bonds to be equal. In general the octahedral tilting is the most common [9].

It must also be pointed out that what has been said above concerning the A and B cations, always remains the same for the A' and B' cations successively in a double perovskite.

Either way, outside the stability range, the perovskite structure show distortions (of which the tilting of the BO_6 octahedra are the most common) compared to cubic structure. Several detailed structural studies on a large number of perovskite compounds have been carried out in order to characterize and classify the different types of possible distortions. In this context, numerous systems of notations, taking into account the number of axes of rotation of the octahedra, have been developed. The most used are those developed by A.M. Glazer [19], K. S. Aleksandrov [20], and P.M. Woodward [21, 22]. Thus, Glazer counted 23 octahedron rotation systems around the 3 possible axes of the ideal perovskite (see Figure I.5). The rotation around each axis is described by 2 symbols. The first is a letter a, b and c characterizing the amplitude of rotation about this axis relative to the amplitude of rotation around the other axes. In the case where the amplitude of the rotation is the same along several axes, the letter is repeated. The second, a positive or a negative superscript indicating tilt of octahedra in successive layers in a specific direction. A positive superscript "+" indicates tilt of octahedra in successive layers in the same direction (in-phase tilt), whereas a negative superscript "-" indicates rotation of consecutive octahedra along a specific rotation axis in the opposite sense (anti-phase tilt). A zero superscript "0" is assigned to the letter when there is no rotation about a specific axis. For example, a notation $a^+b^-c^0$ corresponds to the inclination of octahedra in-phase about the a-axis, in opposition of phase (in anti-phase) about the b-axis and the absence of inclination about c-axis (see Figure I.6 for other examples).

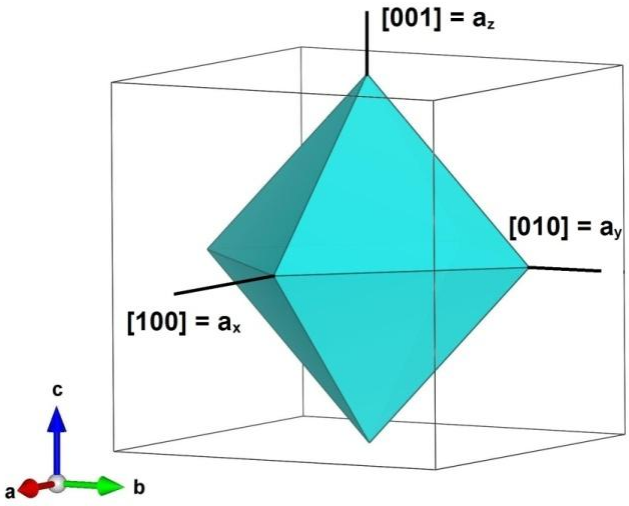

Figure I.5: Directions of rotation of the B/B'O_6 octahedron relative to the pseudocubic cell axes. Glazer (1972) tilt axes are shown as a_x, a_y and a_z.

In light of the 23 rotation systems obtained by Glazer and on the basis of group theory, Howard and Stokes (1998) [23] confirmed Glazer's (1972) analysis, but reduced the number of tilt systems to 15, as some of Glazer's tilt systems were combinations of one or more of the basic fifteen. Thus, they established group relations to existing subgroups as illustrated in Figure I.7.

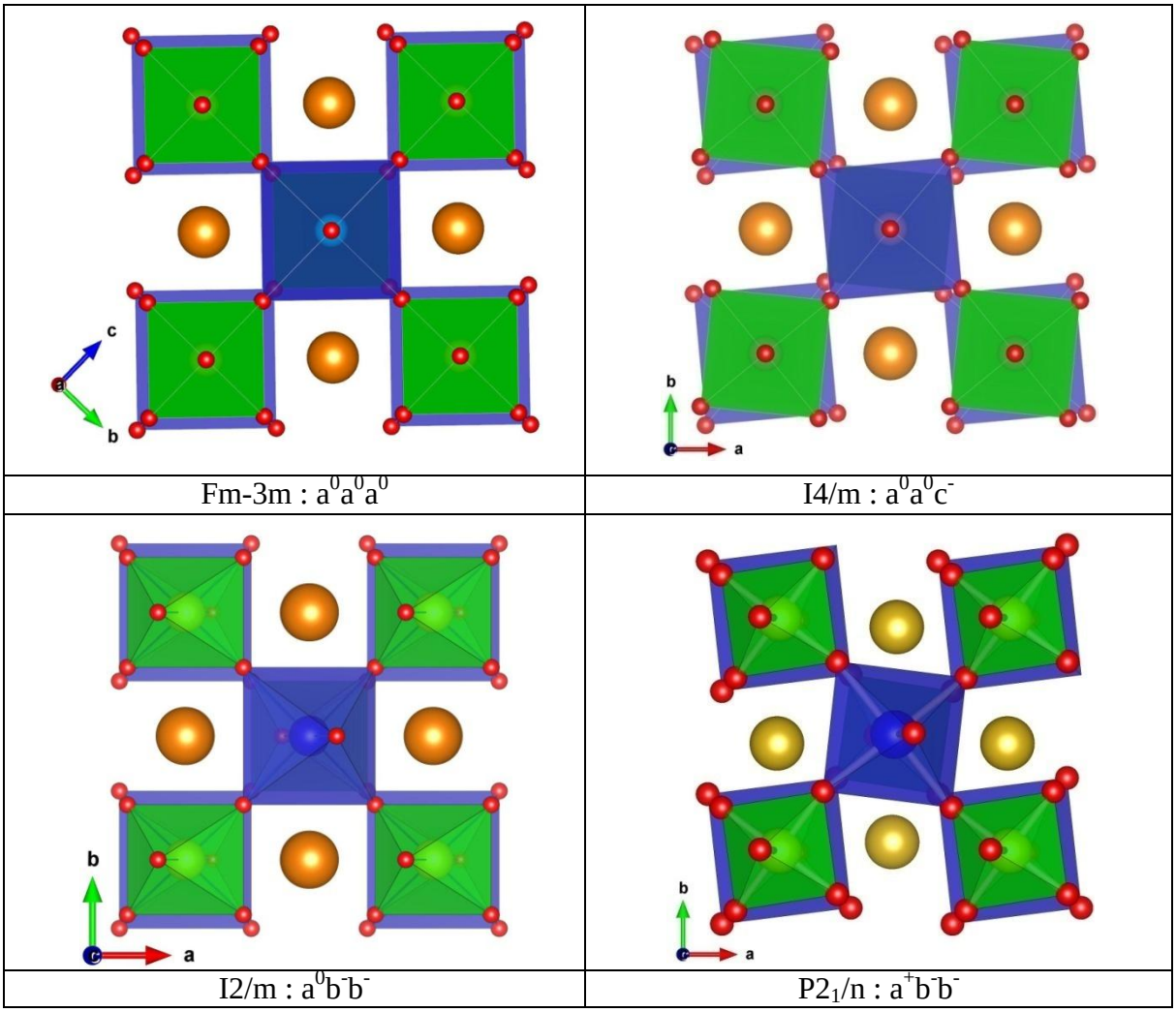

Fm-3m : $a^0a^0a^0$	I4/m : $a^0a^0c^-$
I2/m : $a^0b^-b^-$	$P2_1/n$: $a^+b^-b^-$

Figure I.6: Representation of the different types of octahedral tilts, no tilts, one tilt, two tilts and tree tilts.

In the other hand, Woodward (1997) summarized Glazers' work for ordered double perovskite structures ($A'A''B'B''O_6$) [21] in seeking to the different space groups corresponding to each 23 Glazer tilts, that allow B and B" cation ordering while maintaining the rigid octahedra. Thus, 14 possible space groups were searched for 1:1 ordered double perovskites.

Subsequently, exhaustive studies by Woodward show that 12 of the 15 tilt systems reported by Howard and Stokes naturally exist [24] (Table I.2 and Figure I.8). None of the eight Glazer tilt systems omitted by Howard and Stokes have been experimentally observed [22].

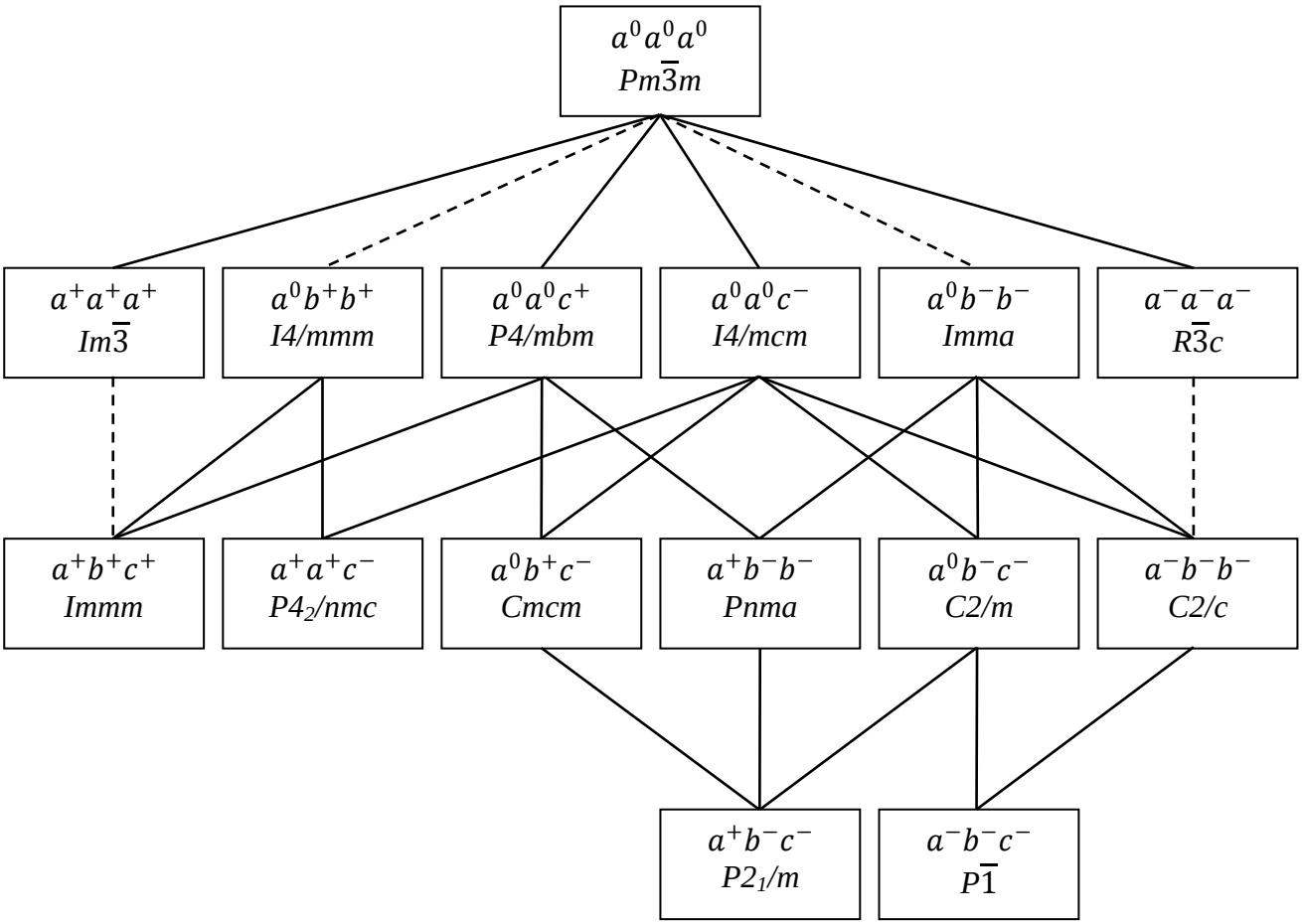

Figure I.7: Diagram of the 15 space groups that describing the possible symmetries caused by octahedral rotation/tilting in perovskites. The presence of a line between spaces groups indicate where a group-subgroup relationship exists. A solid line signifies a transition that is allowed to be continuous and a dashed line indicates a transition that is required to be 1st order [23].

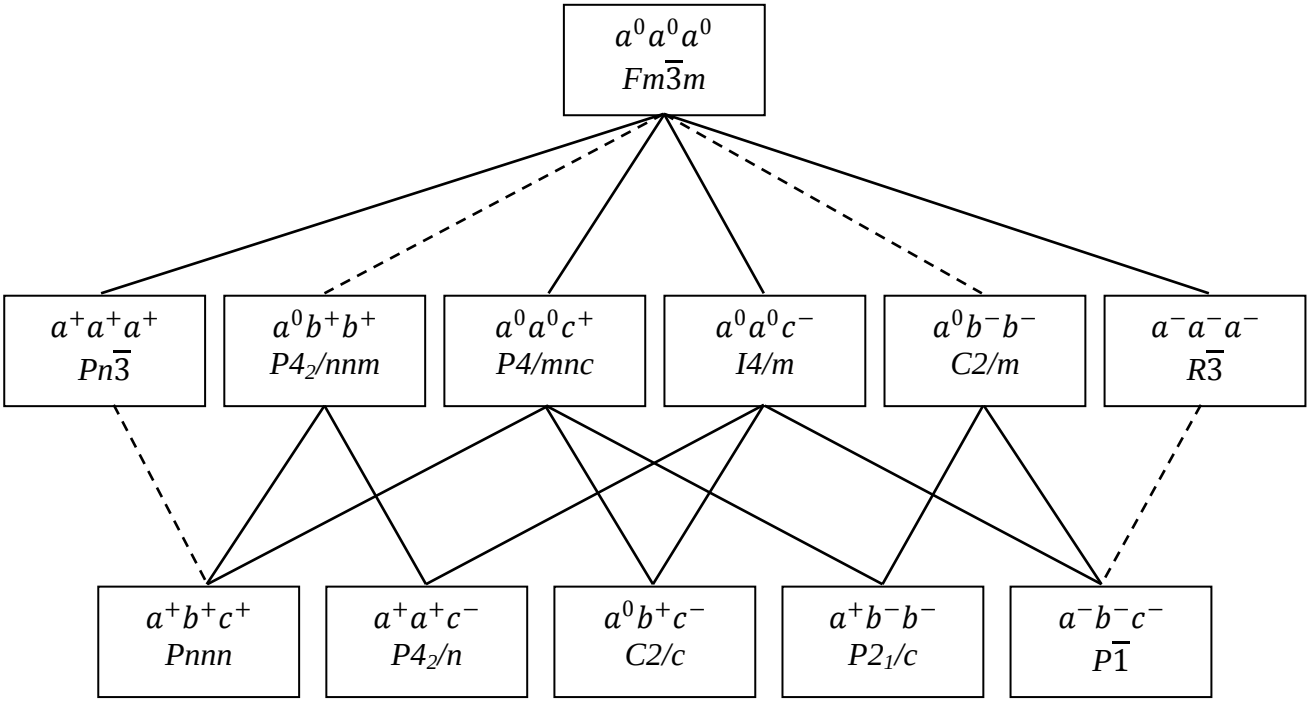

Figure I.8: Diagram of the 12 space groups that describing the possible symmetries caused by octahedral rotation/tilting in double perovskites. The lines have the same meaning as in the Figure I.7 [26].

Table I.2: The Glazer-tilts and space groups for simple and double perovskites. Numbers after the tilt system correspond to the original numbering scheme proposed by Glazer. Numbers after the space group are those listed in the International Tables for Crystallography [25]. "*" indicates the space groups corresponding to the tilt systems reported by Howard and Stokes that do not naturally exist.

Type	N°	Tilt Systems	Space group for Ternary Perovskite	Space group for Double Perovskite
No tilt	1	$a^0a^0a^0$ (#23)	*Pm$\bar{3}$m* (#221) Z=1	*Fm$\bar{3}$m* (#225)
One tilt	2	$a^0a^0c^+$ (#21)	*P4/mbm* (#127) Z = 2	*P4/mnc* (#128)
	3	$a^0a^0c^-$ (#22)	*I4/mcm* (#140) Z = 4	*I4/m* (#87)
Tow tilts	4	$a^0b^+b^+$ (#16)	*I4/mmm* (#139) Z = 8	*$P4_2/nnm$* (#134)
	5	$a^0b^+c^-$ (#17)	*Cmcm* (#63) Z = 8	*C2/c* (#15)
	6	$a^0b^-c^-$ (#19)	*C2/m* (#12) Z = 4	N/A *
	7	$a^0b^-b^-$ (#20)	*Imma* (#74) Z = 4	*I2/m* (#12)
	8	$a^+b^+c^+$ (#1)	*Immm* (#71) Z = 8	*Pnnn* (#48)
Three tilts	9	$a^+a^+a^+$ (#3)	*Im$\bar{3}$* (#204) Z = 8	*Pn$\bar{3}$* (#201)
	10	$a^+a^+c^-$ (#5)	*$P4_2/nmc$* (#137) Z = 8	*$P4_2/n$* (#86)
	11	$a^+b^-c^-$ (#8)	*$P2_1/m$* (#11) Z = 4	N/A *
	12	$a^+b^-b^-$ (#10)	*Pnma* (#62) Z = 4	*$P2_1/n$* (#14)
	13	$a^-b^-c^-$ (#12)	P$\bar{1}$ (#2) Z = 2	*P$\bar{1}$* (#2)
	14	$a^-b^-b^-$ (#13)	*C2/c* (#15) Z = 4	N/A *
	15	$a^-a^-a^-$ (#14)	*R$\bar{3}$c* (#167) Z = 4	R$\bar{3}$ (#148)

References:

[1] G. Rose (1839) scripsit. Ann. Phys., Berlin Bd48.S.558

[2] M.T. Anderson, K.B. Greenwood, G.A. Taylor, K.R. Poeppelmeier, Prog. Solid State Chem. 22 (1993) 197-233.

[3] M.T. Anderson, K.R. Poeppelmeier, Chem. Mater. 3 (1991) 476-482.

[4] Meghan C. Knapp, Patrick M. Woodward. J. Solid State Chem. 179 (2006) 1076–1085

[5] P.K. Davies, Curr. Opin. Solid State Mater. Sci. 4 (1999) 467–471.

[6] A. J. Jacobson, B.M. Collins, B. E. F. Fender, Acta. Cryst. B 32 (1976) 1083.

[7] F. Galasso, W. Darby, J. Phys. Chem. 66 (1962) 131.

[8] L. H. Brinxner, J. Phys. Chem. (1960) 165.

[9] R.H. Mitchell, Almaz Press, Ontario, 2002.

[10] H.D. Megaw, C.N.W. Darlington, Acta Cryst. A 32 (1975) 161-173.

[11] R. D. Shannon et C. T. Prewitt, Acta Cryst. B, vol. 25, n° 5, p. 925-946, mai 1969.

[12] R. D. Shannon et C. T. Prewitt, Acta Cryst. B, vol. 26, n° 7, p. 1046-1048, juill. 1970.

[13] R. D. Shannon, Acta Cryst. Sect. A, vol. 32, n° 5, p. 751-767, sept. 1976.

[14] V.M. Goldschmidt, Die Gesetze der Krystallochemie, Naturwissenschaften. 14 (1926) 477–485.

[15] L. Liang, L. Wencong, C. Nianyi, J. Phys. Chem. Solids. 65 (2004) 855–860.

[16] C. Li, X. Lu, W. Ding, L. Feng, Y. Gao, Z. Guo, Acta Cryst. Sect. B Struct. Sci. 64 (2008) 702–707.

[17] J. B. Philipp, P. Majewski, L. Alff, A. Erb, R. Gross, T. Graf, M. S. Brandt, J. Simon, T. Walther, W. Mader, D. Topwal and D. D. Sarma (2003) Phys. Rev. B 68 144431-13

[18] J.D. Donaldson, J. Silver, S. Hadjiminolis, S.D. Ross, J. Chem. Soc. Dalt. Trans. 0 (1975) 1500-1506.

[19] A.M. Glazer, Acta. Cryst. B 28 (1972) 3384-3392.

[20] K. S. Aleksandrov, Kristallografiya 21 (1976) 249-255.

[21] P.M. Woodward. Acta. Cryst. B, 53 :32-43, 1997.

[22] P.M. Woodward. Acta. Cryst. B, 53 :44-66, 1997.

[23] C. J. Howard and H. T. Stokes (1998) Acta Cryst. B 54 782-789

[24] M. A. Islam, J. M. Rondinelli and J. E. Spanier, J. Phys. Condens. Matter. 25 (2013) 175902

[25] International Tables for Crystallography (1995). Vol. A, Space Group Symmetry, 3rd ed., edited by T. Hahn. Dordrecht: Kluwer Academic Publishers.

[26] C.J. Howard, B.J. Kennedy, P.M. Woodward, Acta Cryst. B 59 (2003) 463-471.

Chapter II

Preparation method and experimental techniques

In this chapter, we will present the synthesis method and the main techniques used to characterize the different materials synthesized during this study: X-ray diffraction and Raman spectroscopy.

1. Preparation method

A diverse array of methods to synthesize solid compounds and materials are described in the literature, such as:

Solid state synthesis in a silica ampoule sealed under vacuum: The procedure consists in heating the pellets of reagent mixtures in evacuated silica capsules at 900-1035 °C. The product is removed after a short period of heating, ground in an agate mortar, repelleted, and heated again in vacuo for 24 hr. With some preparations this procedure is repeated several times [1, 2]. However, this process leads, in addition to the formation of the double perovskite, to the formation of impurities (such as $SrMoO_4$ and $BaMoO_4$ for example). In another study [3], it was demonstrated that by increasing the sintering temperature above 1100 °C, this process leads to samples without impurities.

Another process using rapid heating of the stoichiometric mixture of reagents in an atmosphere of oxygen pressure of 10^{-10} atm, controlled by mixing of H_2 and CO_2 at 1200 °C, was reported by Itoh, Wang et al [4, 5]. The powders obtained are made into pellets and followed by secondary heat treatment at 1200 °C.

Another method by the sol-gel process, has been used by [6], the precursors were mixed stoichiometrically with nitric acid until a gel formed. The gel was dried, then preheated at 700 °C for 6 h. Finally, the powders were finely pulverized and made into pellets followed by sintering at different temperatures (900, 950, and 1000 °C) in a stream of 5% H_2/Ar for 3h.

Although a variety of processes are used in preparation of polycrystalline solids, including the examples above-mentioned, the conventional solid state synthesis method is the most widely used. This one is essentially based on from the direct heating of solid state starting materials. The Solid state reaction is performed in the absence of solvent, which is one of the main advantages of this process in addition to its simplicity and the possibility it provides to synthesize large amount of powder. However, this reaction cannot take place at room temperature over normal time scales and it is necessary to heat the stoichiometric mixture of starting materials to high temperatures, often from 500 to 2000 °C in order for the reaction to occur at an appreciable rate.

In this work, we have used the solid state synthesis whose the protocol was as follows (Figure II.1):

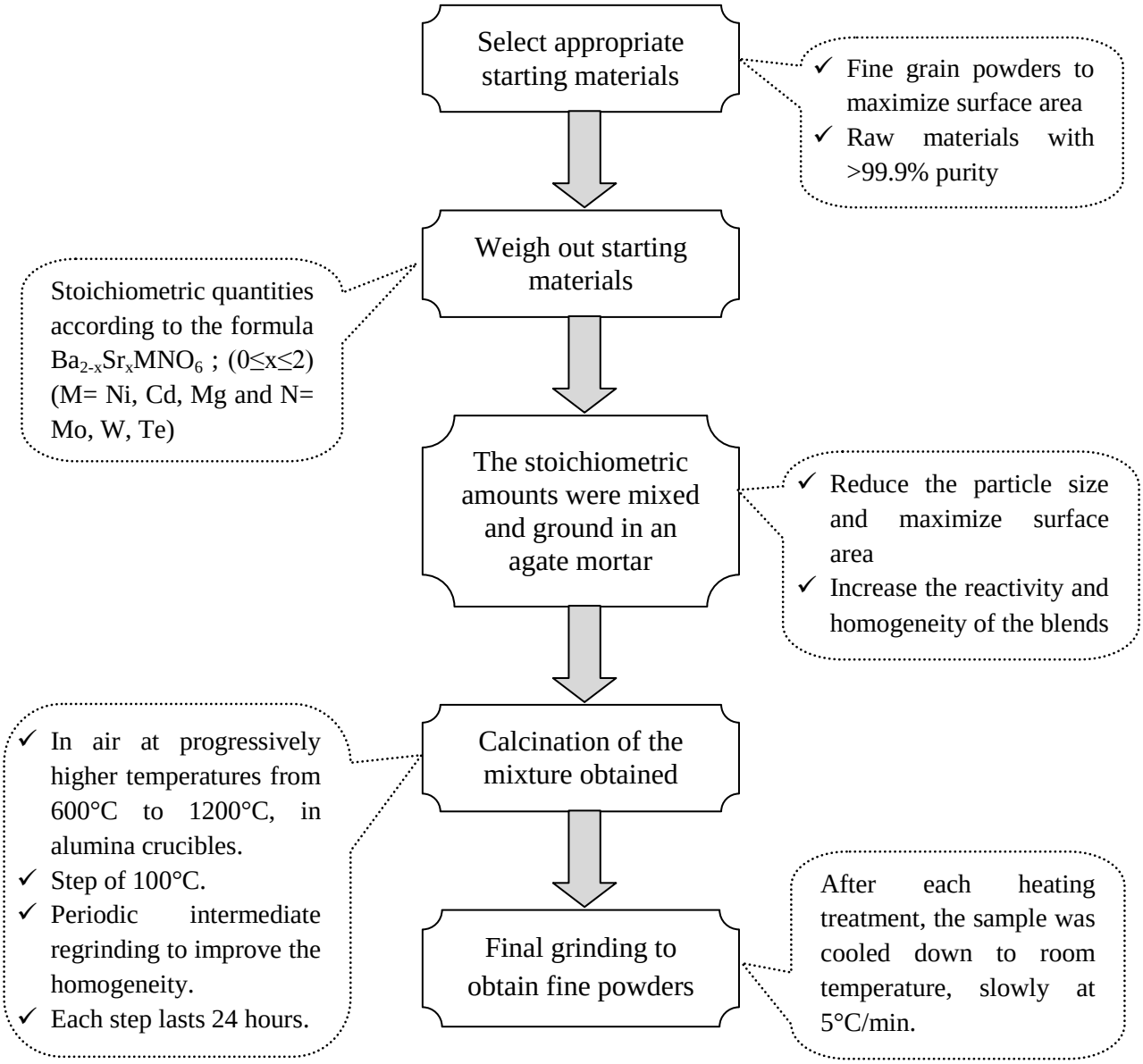

Figure II.1 Schematic illustration of double perovskite oxide synthesis by conventional solid state reaction route in this thesis.

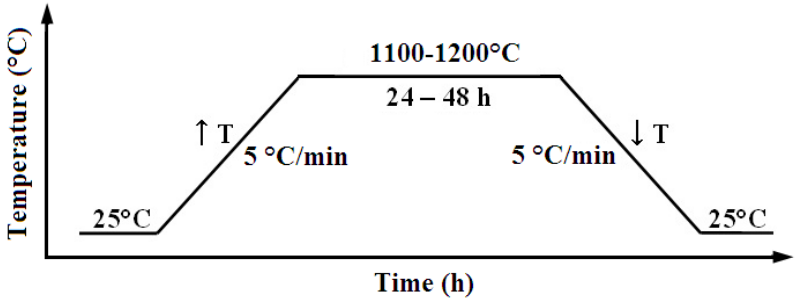

Figure II.2: Temperature program for the calcination stage.

Note that the granulometry of the particles plays a particularly important role in the kinetics of the reaction and in the homogeneity of the compounds obtained, because the diffusion process is relatively slow in the solid state. In order to compensate for this, we have carried out several successive sintering at 1100-1200°C for 48 hours with intermediate grindings.

2. Samples synthesis

The polycrystalline samples $Ba_{2-x}Sr_xMeMO_6$ (Me = Ni, Cd, Mg, M = Mo, W, Te and $0 \leq x \leq 2$) were synthesized by solid state chemical reaction at high temperature using high purity precursors (99.9%), described in Table II-1. For this, stoichiometric quantities of raw materials, dictated by the finished product formula, were weighed, mixed according to the chemical reactions shown below:

$$(2\text{-}x)\ BaCO_3 + (x)\ SrCO_3 + NiO + MoO_3 \rightarrow \mathbf{Ba_{2-x}Sr_xNiMoO_6} + 2CO_2$$

$$(2\text{-}x)BaCO_3 + xSrCO_3 + MgO + MoO_3 \rightarrow \mathbf{Ba_{2-x}Sr_xMgMoO_6} + 2CO_2$$

$$(2\text{-}x)BaCO_3 + (x)SrCO_3 + Cd(NO_3)_2;4H_2O + WO_3 \rightarrow \mathbf{Ba_{2-x}Sr_xCdWO_6} + 2CO_2 + 2NO_2 + ½\ O_2 + 4H_2O$$

Table II.1: Precursors used in the synthesis of the samples and upper limit of calcination temperature for each series of sample.

Product formula ($0 \leq x \leq 2$)	$Ba_{2-x}Sr_x$**NiMo**O_6	$Ba_{2-x}Sr_x$**MgMo**O_6	$Ba_{2-x}Sr_x$**CdW**O_6
Precursors (99.9% purity)	- $BaCO_3$ - $SrCO_3$ - NiO - MoO_3	- $BaCO_3$ - $SrCO_3$ - MgO - MoO_3	- $BaCO_3$ - $SrCO_3$ - WO_3 - $Cd(NO_3)_2;4H_2O$
Upper limit of calcination temperature (°C)	1200	1200	1100

This mixture is then finely ground in an agate mortar, and heated in air in alumina crucibles according to the following heat treatment procedure: The samples were heated to progressively higher temperatures from 100°C to 1100-1200°C with a step of 100°C and periodic intermediate regrinding to improve the homogeneity. Each step lasts 24 hours except

the last treatment at 1100-1200°C which lasts 48 hours. After each heating treatment, the sample was cooled down to room temperature, slowly at 5°C/min (Figure II.2). In order to control the quality of the obtained materials, X-ray diffraction analysis was performed after each heating from 700°C.

3. X-ray Powder Diffraction (XRD):

3.1 Principle of the method

Following the discovery of X-rays by Röntgen in 1895, the X-ray diffractometry technique had developed. This technique has its roots in the earlier half of the 20th century; however, it was not until the 1960s that the technique became widely accepted [7]. Since then, the X-ray diffraction has become the most powerful method and the most flexible analytical technique for investigation, identification and quantitative determination of crystalline phases of solids and of powder samples [8], to such an extent that is the most used technique for a first contact with a solid phase. It has the advantage of being more efficient technique. It has the advantage of being more efficient technique, easy-to-use and non-destructive. In comparison to the reference diagrams of a large number of compounds (X-ray diffraction databases), it can quickly identify the crystallized phases present in the studied sample [9]. It also allows it possible to follow the evolution of the crystalline phases over time, i.e. to observe their presence as well as to evaluate their proportion in the sample [10, 11] as a function of the experimental conditions such as temperature, pressure.... Using this technique, we can obtain structural information (crystal symmetry, lattice parameters, distribution of atoms within the unit cell), textural (crystallite dimensions, internal stresses of the network) and composition (qualitative and quantitative, by comparing the position and intensity of the diffraction lines obtained).

The X-ray diffraction technique is based on the fact that interatomic distances, of the order of an angstrom, are of the order of wavelength associated with X-rays. Of an electromagnetic nature, the waves interact with the electrons of atoms. Sir William Henry Bragg, after several researches on crystal structure with her son W.L.Bragg, derived a simple equation relating the diffraction angle with the diffracted wavelength and the interplanar spacing [7], this relation is known as Bragg's Law. In Bragg's representation, diffraction is described as the reflection of an X-ray beam by crystallographic planes defined by indices hkl. Incident waves reflected by equivalent planes with characteristic separation d_{hkl} are in phase if the difference in their

travel (2Θ in Fig. II.3) is equal to an integral number of wavelengths n [7]. In other words, Bragg's law means that the diffraction can occur only when the equation below (equation II-1) is satisfied. Therefore, a diffraction pattern should be a succession of Dirac peaks located at 2θ angles. These detected peaks are then processed, and counted.

$$2.d.\sin\theta = n.\lambda \qquad \text{(II-1)}$$

Where:

- n: is a positive integer,
- λ: is the wavelength of the X-ray,
- d: is the distance between the lattice plane,
- θ: is the incident glancing angle (supplement of the incident angle).

This relation demonstrates that it is sufficient to measure the Bragg angles (θ) to determine the dimensions and the form of the elemental unit cell of the crystal. The amplitudes of the reflected waves make it possible to determine the atomic structure of the pattern. Typically, this is achieved by conversion of the diffraction peaks to d-spacings, because each compound has a set of unique d-spacings. Thereafter, these results are to be compared with standard reference patterns.

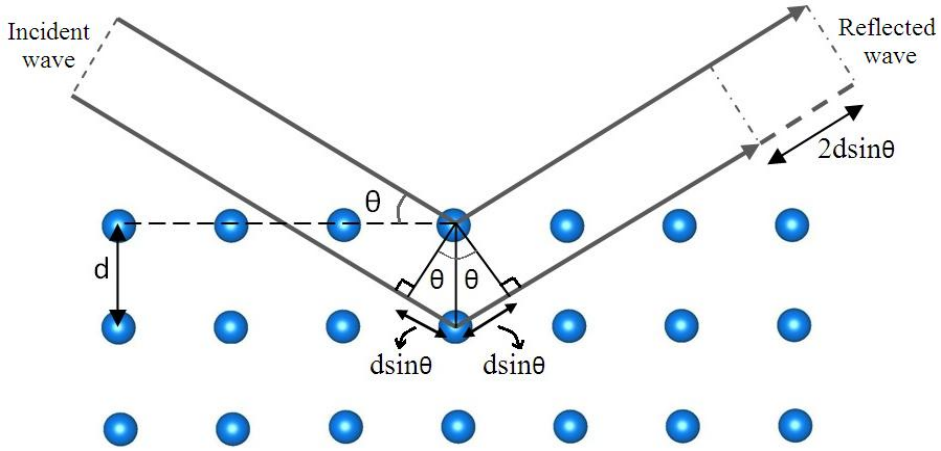

Figure II.3: X-ray diffraction with a crystal. Two incident waves reflect off two planes of a crystal. The difference in path lengths is indicated by the dashed line.

Note that in Bragg's law, the angle θ for the incident and reflected waves are measured with respect to the surface itself, unlike the general practice in geometric optics, where θ is measured with respect to the normal.

From an instrumental point of view, X-ray diffractometers consist of three basic elements: an X-ray tube, a sample holder, and an X-ray detector [12]. X-rays used for X-ray diffraction (XRD) can be generated in many ways. The two most commonly used methods, the X-ray tube method and synchrotron X-ray [13]. The X-ray tube method is actually Röntgen's method and is mostly used in laboratory X-ray diffractometers. In this method, X-rays are generated in a cathode ray tube by heating a filament to produce electrons, accelerating the electrons in vacuum toward a metal target (anode) by applying a voltage in the range 20-60 kV. Thereafter, the target material is bombarded by electrons. When electrons have sufficient energy to dislodge inner shell electrons of the target material, characteristic X-ray spectra are produced.

The specific wavelengths are characteristic of the target material (Cu, Fe, Mo, Cr). In the current study, the copper Cu is the metal used whose characteristic X-rays have wavelengths $K_{\alpha 1}$ = 1.5406Å, $K_{\alpha 2}$ = 1.5444Å, $K_{\beta 1,3}$ = 1.3922 and $K_{\beta 3}$ = 1.3926Å in an approximate intensity ratio of 100:50:30:15 [14].

As the sample and detector are rotated, the intensity of the reflected X-rays is recorded. When the geometry of the incident X-rays impinging the sample satisfies Bragg's law, constructive interference occurs and a peak in intensity appears.

3.2 Instrument

Since the 1940s, the instrumentation that is used for powder diffraction measurements has not changed much. The major difference found in modern instrumentation is the use of the computer for control, data acquisition, and data processing [15]. Figure II.4 illustrates the geometry of the system, showing the layout of a typical diffractometer. This geometric arrangement is known as the Bragg-Brentano parafocusing system and is typified by a diverging beam from a line source, falling onto the specimen, being diffracted and passing through a receiving slit to the detector. The advantage of this system is that the recording is made using a mobile goniometer provided with a sensor instead of a photosensitive film.

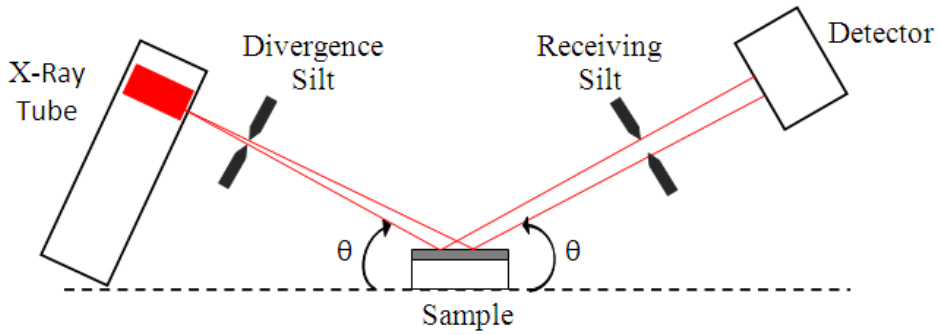

Figure II.4: Typical scheme of a Bragg-Brentano type diffractometer

In the current study, powder X-ray diffraction patterns were collected at room temperature on a D2 PHASER diffractometer (Figure II.5), with the Bragg–Brentano geometry, using CuKα radiation (λ=1.5418 Å) with 30KV and 10 mA. The patterns were scanned through steps of 0.01 (2θ) in the 2θ range 15–105°. The full pattern refinements were carried out by means of the Rietveld method using the Fullprof program [16] integrated in Winplotr software [17]. The Rietveld refinement of the observed powder XRD data is initiated with scale and background parameters and successively other profile parameters are included. The background is fitted with a fifth order polynomial. The peak shape is fitted with a pseudo-Voigt profile function. After an appreciable profile matching the position parameters and isotropic atomic displacement parameters of individual atoms were also refined.

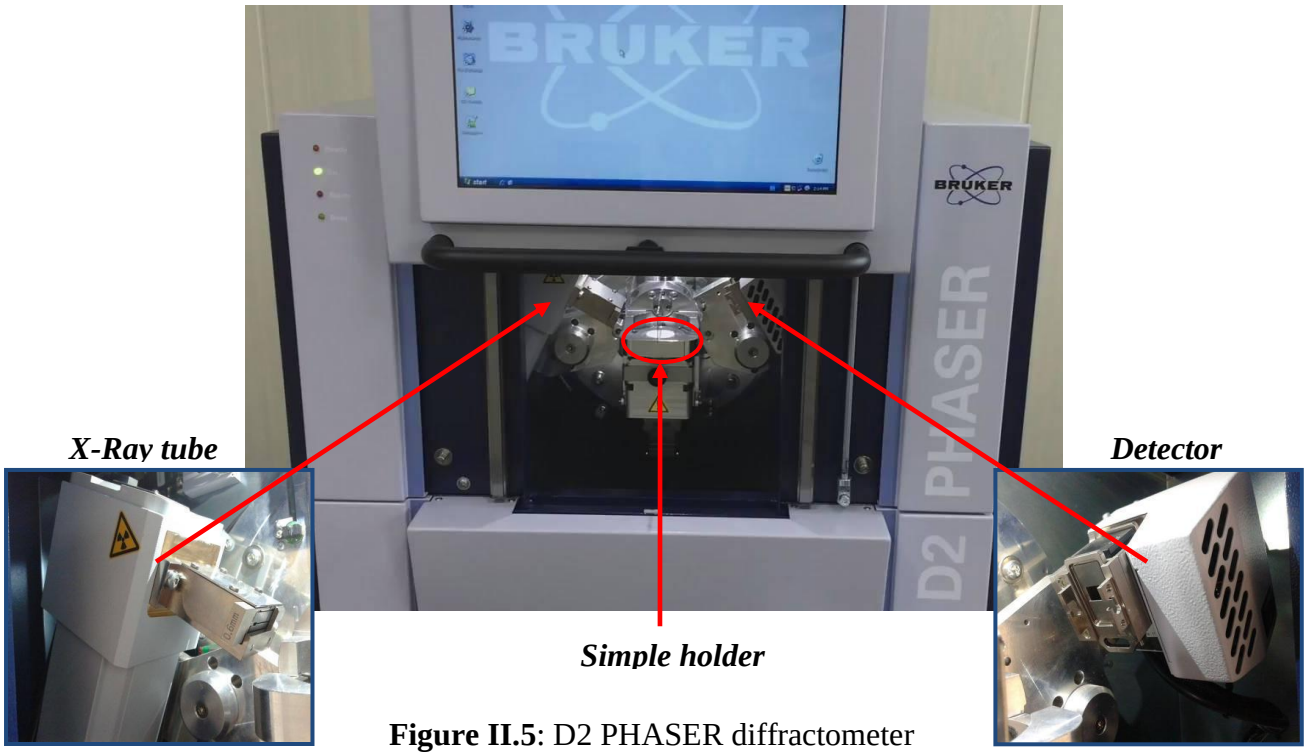

Figure II.5: D2 PHASER diffractometer

3.3 Sample preparation

To obtain good quality X-ray diffraction patterns, on powder or on polycrystalline material, it is important to have a good sample. Thus, a sample is considered to be of good quality, if the size of its particles is reduced as possible and that its surface is plane and smooth. Hence, it is desired to reduce the particle size, of about 0.002 mm to 0.005 mm section, to orient the crystals randomly, rather than in a preferred orientation to have a complete representation of the sample and enhance the statistical significance of the analysis (related to the randomness of the sample). The necessary conform quantity of the powder to this technique varies between 0.5 and 1g. It is preferable to work with the maximum of powder to have at least one millimeter of analyzable thickness; the measurement will then be less sensitive to the orientations of the material. The ideal sample is homogeneous and the crystallites are randomly distributed. The sample is pressed into a sample holder so that we have a smooth flat surface. This set of measures taken for sample preparation should lead to a distribution of all possible (h, k, l) plans. Only crystallites with reflective planes (h, k, l) parallel to the surface of the sample contribute to the reflected intensities. For a truly random sample, each possible reflection from a given set of (h, k, l) planes will have an equal number of crystallites contributing to it. We only have to rock the sample through the glancing angle THETA in order to produce all possible reflections.

Following all this preliminary considerations, we get, as raw data, a powder X-ray diffraction pattern (Figure II.6).

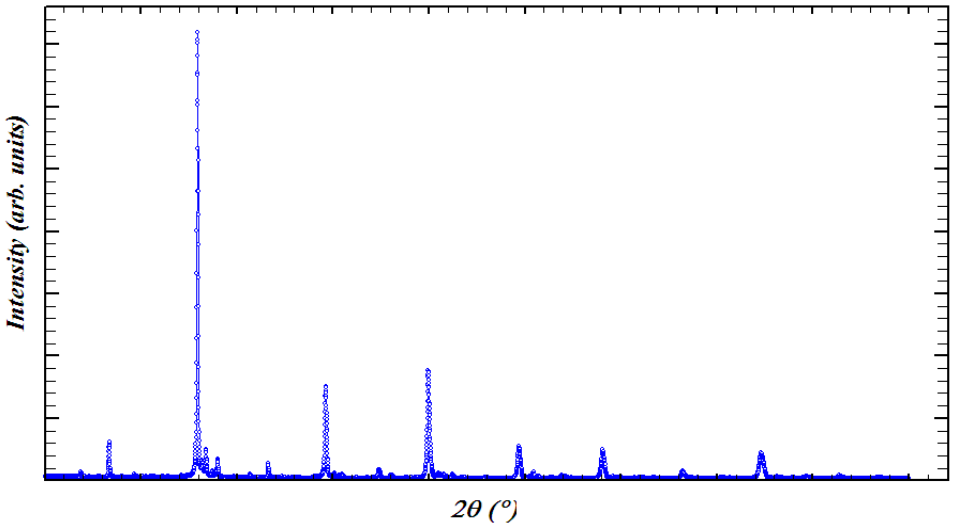

Figure II.6: X-ray diffraction pattern I=f(2θ)

This one is the sum of four different contributions:

- The position of the diffraction lines, related to the unit cell of the crystal.
- The intensity of these diffraction lines, which is significant of the structure inside the crystalline cell.
- The profile of the lines, which depends on the experimental resolution of the diffractometer and the characteristics of the powder to be studied.
- The continuous background, which can give information on the presence of a component due to the presence of an amorphous material.

4. Diffraction Data Analysis : Rietveld method

4.1 Rietveld method

The analysis of X-ray diffractograms was carried out by the Rietveld method [18, 19]. The intensity observed at each point of the diagram is considered as the sum of the contributions of all the diffraction lines.

The Rietveld method corresponds to the adjustment of a structural model to the diffractogram obtained experimentally. The main information obtained is: the elementary cell parameters, positions of the atoms in the elementary cell, distance and binding angle, the occupancy rates of different atoms, mass fractions and the thermal factors. The optimization of the model takes into account simultaneously all the factors affecting the measurement of the diagram, such as:

- ✓ The instrumental characteristics: the diffractometer resolution curve and the instrumental line profile.
- ✓ The structural parameters: cell parameters and atomic positions.
- ✓ The microstructural parameters: sizes and microdeformations of crystallites

The first applications of the Rietveld method to the analysis of X-ray diffraction data were only reported in the late 1970s by Malmros & Thomas and Khattack & Cox [20, 21]. Since then, many programs have emerged, most of which can process data from both X-rays and neutrons. The most widely used program is Fullprof by J. Rodriguez Carvajal [22], it allows, on the one hand, to analyze the data obtained by X-rays or by neutrons and on the other hand, to treat several phases simultaneously.

The refinement program minimizes, by the least squares method, the difference M (formula II-2), called residue, between the experimental values I_{obs} and the calculated values I_{calc}.

$$M = \sum_{i=1}^{i=N} w_i[(I_{obs})_i - (I_{calc})_i]^2 \quad \text{(II-2)}$$

with : $$(I_{obs})_i = I_{(backgound\ )i} + \sum_i I_{(Bragg)i} \quad \text{(II-3)}$$

where:

- w_i : is the statistical weight assigned to each point: $w_i = \frac{1}{\sigma^2}$; (σ^2 the variance of $(I_{obs})_i$)
- $(I_{obs})_i$: the observed intensity of each equally spaced steps i over the entire pattern including the background intensity and the sum of the contribution of reflections close to the i powder pattern step (formula II-3)
- $(I_{calc})_i$: calculated intensity for each 2θi and can be calculated as:

$$(I_{calc})_i = I_{(backgound\ )i} + \sum_{\phi=1}^{N} S_\phi \sum_{k=k1}^{K2} j_{\phi k}.Lp_{\phi k}.O_{\phi k}.A.\left|F_{\phi k}\right|^2.\Omega_{i\phi k} \quad \text{(II-4)}$$

where:

- $I_{(backgound\ )i}$: the background intensity at the step i of the diffraction pattern
- S_ϕ : scale factor, proportional to the volume fraction of each refined phase
- $j_{\phi k}$: multiplicity factor of the k^{th} reflection
- $Lp_{\phi k}$: contains the Lorentz polarization and multiplicity factors
- $O_{\phi k}$: correction factor describing the preferred orientation
- A : an empirical function of the correction of micro absorption
- $|F_k|$: the structure factor which includes nuclear and magnetic structure factors if applicable
- $\Omega_{i\phi k}$: is the peak shape function which describes the effects of the instrument and the sample on the reflection profiles

The first summation concerns all the crystalline phases present in the sample and the second on all the neighboring reflections.

During the refinement cycles, each of these terms and its parameters may be varied to improve the match between observed and calculated diffraction patterns, i.e. to minimize the difference M.

4.2 Goodness-Of-Fit : Reliability factors

Then, to evaluate the refinement, several factors (mathematical criteria characteristic of the quality of fit) were introduced allowing to know the agreement between the calculated model and the observed model [23], and thus to estimate the quality of the process of minimization of the function M. The factors the most used are the «Goodness-Of-Fit» Gof, the «R-profile» R_p, the «R-weighted profile» R_{wp} and the « R-expected pattern » R_{exp}. The corresponding equations are given below:

$$R_p(\%) = 100 \times \frac{\sum_{i=1}^{n} |(I_{obs})_i - (I_{calc})_i|}{\sum_{i=1}^{n} (I_{obs})_i} \quad \text{(II-5)}$$

Profile factor for the entire diffraction pattern ($R_{pattern}$)

$$R_{wp}(\%) = 100 \times \sqrt{\frac{M}{\sum_{i=1}^{n} w_i \, [(I_{obs})_i]^2}} \quad \text{(II-6)}$$

Weighted profile factor for the entire diffraction pattern ($R_{weighted\ pattern}$)

M : the function to minimize

$$R_{exp}(\%) = 100 \times \sqrt{\frac{N - P + C}{\sum_{i=1}^{n} w_i \, [(I_{obs})_i]^2}} \quad \text{(II-7)}$$

The statistically expected R value in the absence of systematic errors ($R_{expected}$)

N: number of independent observations

P: number of refined parameters

C: number of constrains applied

$$\chi^2 = \left(\frac{R_{wp}}{R_{exp}}\right)^2 = \frac{M}{N - P + C} \quad \text{(II-8)}$$

Goodness-Of-Fit

The R_{wp} weighted factor and the Goodness-Of-Fit (Gof) factor those that best reflect the refinement progress, because their numerator contains the residue M to be minimized [24].

The values generally desired, at the end of refinement process, for these parameters are between 1 and 2 for the Gof, and for the R_p and R_{wp}, they are "the lowest possible". The minimum theoretical value of R_{wp} is given by the expected factor (R_{exp}) in the absence of systematic errors. However, this corresponds to the case of a pure phase, but the presence of secondary phase (s) substantially increases these values.

It should be noted that the R_p and R_{wp} conventional factors take account of the background intensity, and in order to make them more realistic we have calculated in this thesis report, in addition to the previous factors, the factors cR_p and cR_{wp}, whose calculated and observed intensities are corrected of background intensity. This implies that in these factors, the denominators become weaker while the numerators do not vary. Therefore, their values will be larger than those of R_p and R_{wp}, but more realistic [25]. Moreover, the standard deviations σ_i calculated by the program FULLPROF are corrected by the factor of Berar [26].

$$cR_p(\%) = 100 \times \frac{\sum_{i=1}^{n} |(I_{obs})_i - (I_{calc})_i|}{\sum_{i=1}^{n} ((I_{obs})_i - (I_{BF})_i)} \quad \text{(II-9)}$$

$$cR_{wp}(\%) = 100 \times \sqrt{\frac{M}{\sum_{i=1}^{n} w_i ((I_{obs})_i - (I_{BF})_i)^2}} \quad \text{(II-10)}$$

It is worth remembering that one of the best tools for judging the quality of a refinement remains the human eye, through the curve difference between the curve of calculated values and that of observed values.

5. Raman spectroscopy

5.1 Theoretical aspects

Spectroscopy was originally the study of the interaction between radiation and matter as a function of wavelength (λ). However, spectroscopy is the use of the absorption, emission, or scattering of electromagnetic radiation by matter to qualitatively or quantitatively study the matter or to study physical processes. With regard to Raman spectroscopy, it is a technique used to observe the vibrational and rotational states of a molecule. It makes it possible to characterize the molecular composition of a sample by identifying the chemical groups that

constitute it. The basic idea of the Raman spectroscopy method is the registration of inelastically scattered light from the sample with subsequent decoding of the spectrum obtained by comparing the frequencies of the oscillations with the characteristic oscillations that is unique to each material. This phenomenon of inelastic light scattering was first documented by Raman and Krishnan in 1928[27]. Raman scattering (also known as Raman effect) is named after Indian physicist Dr. C. V. Raman.

When monochromatic light is directed at a molecule, some of the photons forming the radiation are either reflected or absorbed, and few are scattered. Most of these photons are of the same frequency ν_0 as the incident radiation. This is a scattering phenomenon without frequency change, called Rayleigh scattering or elastic scattering. However, a small fraction of the light (~ 1 in 10^8 photons) is diffused inelastically with a change of frequency. The difference in energy between the incident light and the scattered light is proportional to the vibrational energy of the scattering molecules. This process of energy exchange between scattering molecules and the incident light constitutes the Raman effect.

A standard Raman spectrum comprises the spectral range of 0 – 3500 cm^{-1}. The position and intensity of a vibrational bands are characteristic of the underlying molecular motion and consequently of the atoms participating in the chemical bond, their conformation, and their immediate environment.

5.2 Basic principle:

The principle of Raman spectroscopy consists of sending a monochromatic light on the sample to be studied and analyzing the scattered light. The process involved is as follows: due to the interaction of the incident photons with the sample, some energy is transmitted to elementary particles of which material are constituted (electrons, molecules etc.). This causes their transition from ground energy levels to 'virtual' excited states. These excited states are highly unstable and particles decay instantaneously to the ground state by one of the following three different processes, Rayleigh scattering, Stokes scattering and anti-Stokes scattering:

- Rayleigh scattering: the energy released in the photon must be the same as the energy from the initial photon. Therefore the scattered light has the same wavelength. Rayleigh scattering, therefore, bears no information regarding the vibrational energy levels of the sample (elastic scattering).

- Raman scattering is different in that it is inelastic. The light photons lose or gain energy during the scattering process, and therefore increase or decrease in wavelength respectively. This difference in energy leads to a shift in the emitted photon's frequency away from the excitation frequency. Thus, there are two different cases according to the frequency of the Raman photon, which translates into the relationship below (II-11) [28] :

$$\nu_d = \nu_0 \pm \nu_{vib} \qquad \text{(II-11)}$$

where:

- ✓ $\boldsymbol{\nu_0}$: frequency of the incident photon
- ✓ $\boldsymbol{\nu_d}$: frequency of Raman photon
- ✓ $\boldsymbol{\nu_{vib}}$: frequency of the phonon created in the crystal

If the molecule is promoted from a ground to a virtual state and then drops back down to a (higher energy) vibrational state then the scattered photon has less energy than the incident photon, and therefore a longer wavelength. This is called Stokes scattering.

If the molecule is in a vibrational state to begin with and after scattering is in its ground state then the scattered photon has more energy, and therefore a shorter wavelength. This is called anti-Stokes scattering

Given that the energy differences of the Stokes and anti-Stokes Raman photons with respect to the excitation energy give information about molecular vibrational levels and consequently about the crystalline phases present in the analyzed sample [28, 29, 30]. Namely, the identification of a material (via the position of the peaks), its concentration in the sample studied (via the intensity of the peaks), the structural and dynamic disorder of an element (via the width at half height of the peaks) and the identification of the effect of a determined constraint on the system, for example, the substitution of a chemical element, temperature, etc. (via the shift of the peaks). This is the reason why we are more often interested in three parameters characterizing a Raman peak (the position of the peak, its intensity and its width at mid-height) during the analysis of a Raman spectrum.

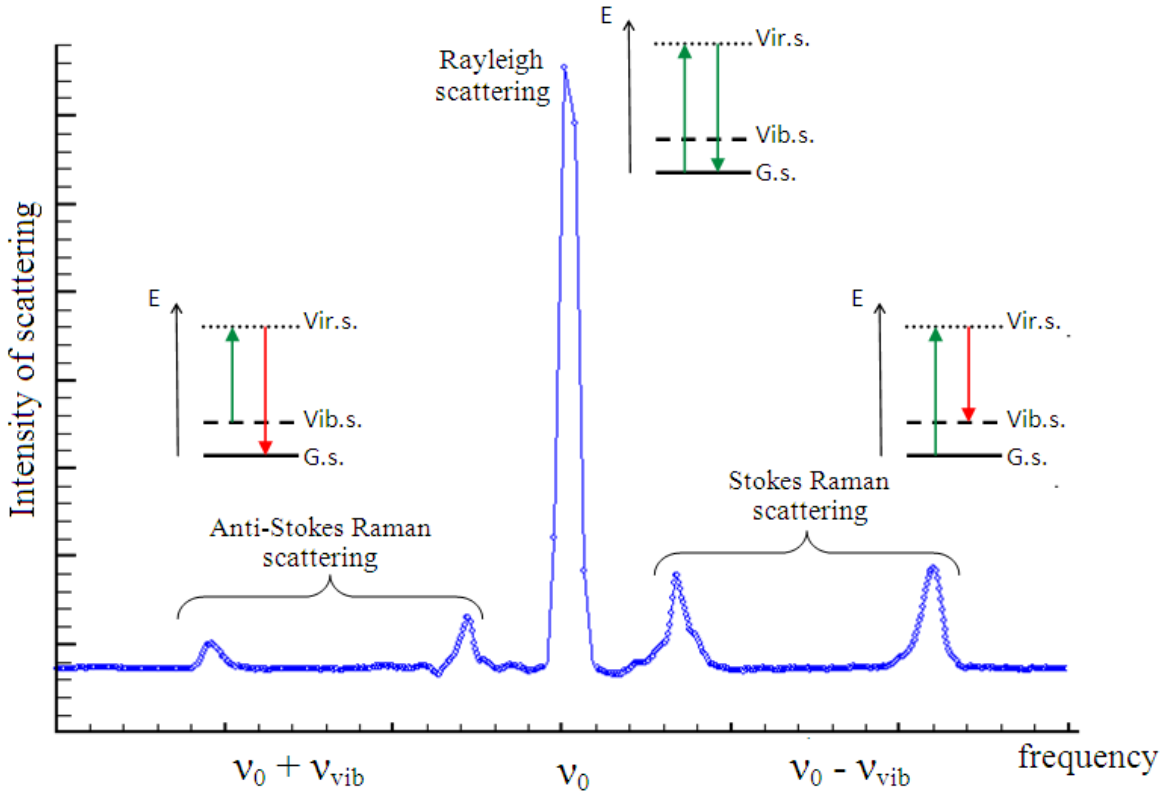

Figure II.7 Illustration of a complete Raman spectra and the three possible modes of scattering during excitation by a monochromatic light source (E = energy level, G.s. = Ground state, Vib.s. = Vibrational state, Vir.s. = Virtual state).

5.3 Intensity diffused by Raman process

The intensity of the peaks obtained by the Raman spectroscopy technique, as in any other type of spectroscopy, is influenced by several factors, those who depend on the instrumentation, on the experimental conditions of the analysis or those who depend on the sample itself (for example, the number of molecules included in the process of interaction with incident light, etc.). All these factors are included in the following equation (II-12) which expresses the light intensity recorded during the Raman scattering process [29, 30]:

$$I = N.K.\mathcal{V}_0^4.I_0.[\beta]^2.(n+1) \qquad \text{(II-12)}$$

where:

N: Number of molecules included in the interaction process between the medium and the incident light (laser).

K: Instrumental factor dependent upon the spectrometer and experimental conditions (wavelength, measurement time, etc.).

$\boldsymbol{\nu_0}$: Frequency of incident light.

$\mathbf{I_0}$: Intensity of incident light.

$[\boldsymbol{\beta}]^{\mathbf{2}} = \left[\frac{\partial \boldsymbol{\alpha}}{\partial \boldsymbol{q}}\right]^{\mathbf{2}}$: where α is the molecular polarizability and q stands for the normal coordinate describing the motion of the atoms during a normal vibration. This parameter is directly related to induced electric dipole moment in the molecule by the electric field of incident radiation. In other words, it measures the variation of polarizability during the vibration and therefore it provides information about the Raman activity [31]. Thus, the modes of vibration active in Raman are those for which this parameter is other than zero ($[\beta]^2 \neq 0$). On the contrary, if $[\beta]^2 = 0$, the vibration (or rotation) does not alter the polarizability of the molecule and the dipole oscillates only at the frequency of the incident radiation.

n: Bose-Einstein factor that is expressed according the following equation : [32, 33]:

$$n = \frac{1}{e^{\left(\frac{h.\nu_{vib}}{k_B.T}\right)}-1} \qquad \text{(II-13)}$$

$h = 6{,}63.10^{-34}\ J.s$: Planck's constant
$k_B = 1{,}38.10^{-23}\ J.K^{-1}$: Boltzmann constant.
T: the temperature expressed in Kelvin.
$h.\nu_{vib}$: the phonon energy.
$k_B.T$: the thermal energy.

This factor defines the population of the levels involved in the different processes at thermal equilibrium. Thus, the Stokes scattering is defined by the population factor (n + 1), and the anti-Stokes scattering by the factor (n) [34]. This implies that the corresponding intensities will be different, the ratio of Stokes and anti-Stokes intensities then expressed by the Boltzmann factor [30, 35]:

$$\frac{I_{Stokes}}{I_{anti\ -Stokes}} \simeq \frac{n+1}{n} = e^{\frac{h.\upsilon_{vib}}{k_B.T}} \qquad \text{(II-14)}$$

Therefore, the intensity of the Anti-Stokes peaks will be lower than that of Stokes peaks because the anti-Stokes diffusion concerns only the molecules existing in an excited state, while the probability of presence of molecules in excited states is lower. The Anti-Stokes part

is less intense and not providing additional spectral information because symmetrical with respect to ν_0, it is the Stokes part which is generally considered in a Raman spectrum.

5.4 Instrument

A set of Raman spectrometry is composed of several elements. The installation first requires a monochromatic light source of the laser type, a sample holder, an optical of collection of scattered light and of coupling with the spectral analysis device (spectrometer), a spectrometer, a very light-sensitive detector, and an electronics for the acquisition and processing of spectral data. However, these elements differ from one type of installation to another, on the one hand, depending on whether this installation is intended to analyze relatively large sizes sample or on the contrary a microscopic quantity of matter and, on the other, in order to adapt to the requirements of each experience (for example, the focusing optics of the laser beam and of scattered light collection).

The Raman spectra were recorded with an Imaging Spectrometer (HoloSpec f/1.8i, Kaiser Optical Systems) designed and built at the Department of Earth Sciences, Uppsala University [36, 37] (Figure II.8). This spectrometer is equipped with a holographic transmission grating and thermoelectrically cooled two-dimensional multichannel CCD detector (Newton, Andor Technology, 1600×400 pixels, thermoelectrically cooled down to -60 °C). The light radiation used for the excitation is an argon laser with a wavelength λ=514.5 nm and a power of 20mW. The spectrometer is also equipped with an optical imaging system (magnification 20×, spatial resolution ~1 μm) and two holographic notch filters (Semrock, Inc.) that blocks the Rayleigh line.

The spectrometer (Figure II.9) was calibrated by fluorescence lines of the neon lamp. Nonpolarized Raman spectra of powdered samples were collected in the back-scattering geometry, in the range 100 – 2300 cm^{-1}, at a resolution of about three cm^{-1}. Accuracy and precision of spectral measurements, as estimated from the wavelength calibration procedure and peak fitting results, were 1.5 cm^{-1} and 0.1–0.4 cm^{-1}, respectively. The acquisition time varied from 10 s to 20 s.

Heating was accomplished by using a mica insulated band heater (DuraBand, 200 W, Tempco Electric Heater Corporation) mounted around the sample and connected to a variable transformer (Figure II.8). Temperature changes during the heating/cooling cycles were induced and controlled by adjusting the transformer's voltage (0–240 V) and monitored with

an accuracy of ±1 °C by the K-type thermocouple adjacent to the sample. During the spectral acquisitions, temperatures were stabilized to within 1 and 3 °C, for the low and high temperature measurements, respectively.

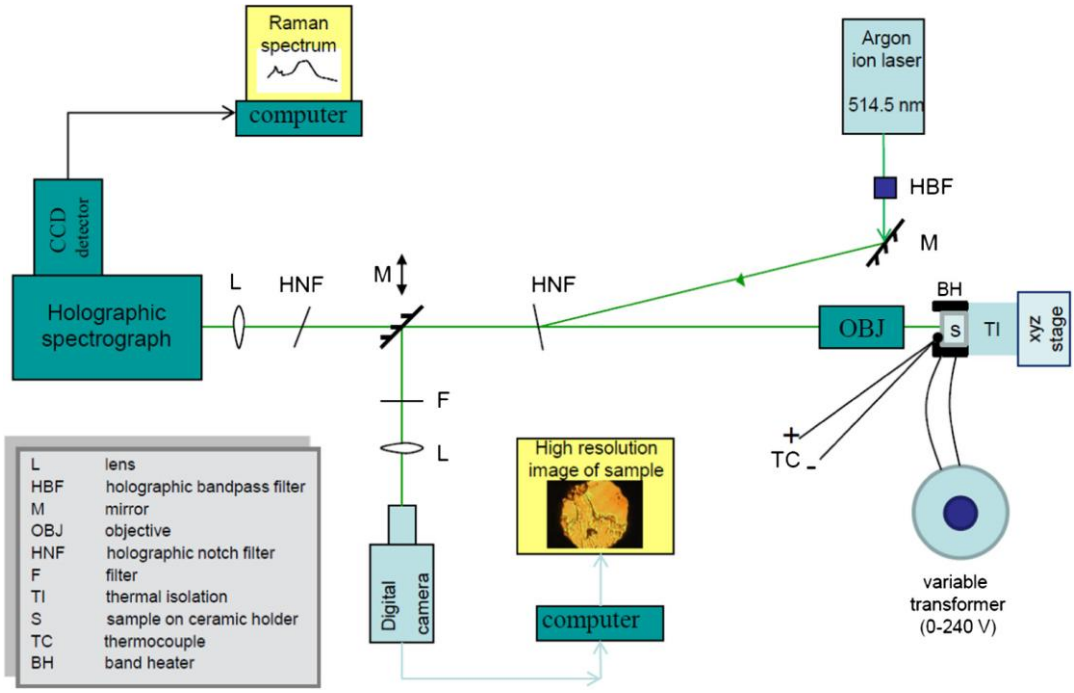

Figure II.8: A schematic diagram of the experimental spectrometer installation [38]

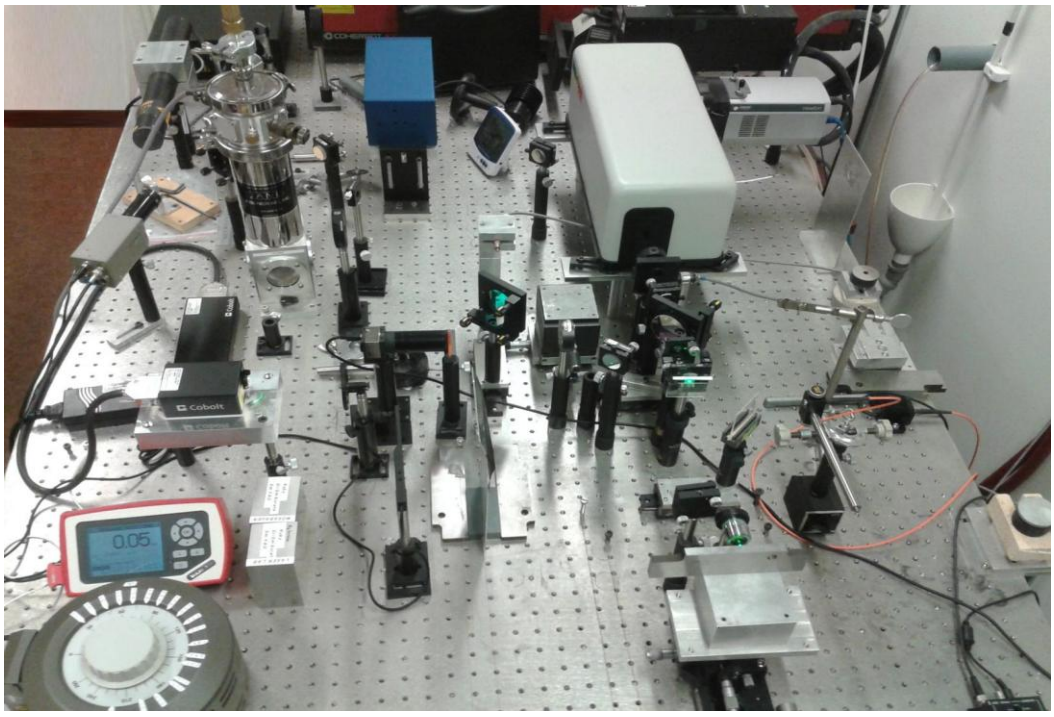

Figure II.9: Real installation of the Raman spectroscopic system [39]

References:

[1] F. K. Patterson, C. W. Moeler et R. Ward, Inorg. Chem., 2, 196 (1963)

[2] F. S. Galasso, F. C. Douglas et R. J. Kasper, J. Chem. Phys., 44, 1672 (1966)

[3] T. Nakagawa, J. Phys. Soc. Jpn., 24, 806 (1968)

[4] M. Itoh, I. Ohta et Y. Inaguma, Mater. Sci. Engineer. B, 41, 55 (1996)

[5] R. Wang et M. Itoh, Solid State Ionics, 108, 269 (1998)

[6] C. L. Yuan, S. G. Wang, W. H. Song, T. Yu, J. M. Dai, S. L. Ye et Y. P. Sun, Appl. Phys. Lett., 75, 3853 (1999)

[7] Ron Jenkins, J. Chem. Educ, 78 (2001) 601.

[8] Martijn Fransen, Faster X-ray powder diffraction measurements, (2002) p:42-49.

[9] The Rietveld Method. Ed. by R. A.Young. Oxford University Press,(1993).

[10] R. Kahn, R. Fourme, A.Gadet, J. Janin, C. Dumas, & D. André, J. Appl. Cryst. 15,330-337.(1982).

[11] F. W. Jones, Proc. Roy. Soc., 166A, 16 (1938)

[12] B. Lavina, P. Dera, R. T. Downs, Rev. Mineral. Geochem., 78, 1 (2014)

[13] Mel Schwartz, Encyclopedia of Materials, Parts and Finishes, 2nd ed., ISBN : 1-56676-661-3, CRC Press (2002)

[14] D. R. Lide, Crc Handbook of Chemistry and Physics 2004-2005: A Ready-Reference Book of Chemical and Physical Data, CRC press, 2004.

[15] Andrei A. Bunaciu, Elena gabriela Udriştioiu & Hassan Y. Aboul-Enein (2015), Critical Reviews in Analytical Chemistry, 45:4, 289-299

[16] J. Rodriguez-Carvajal, Collected Abstracts of Powder Diffraction Meeting, (Toulouse, France), 127 (1990)

[17] T. Roisnel, J. Rodriguez-Carvajal, Mater. Sci. Forum 378, 118 (2001)

[18] H. M. Rietveld, Acta. Crystallogr., 22, 151 (1967)

[19] H. M. Rietveld, J. Appl. Crystallogr., 2, 65 (1969)

[20] G. Malmros, J. O. Thomas, J. Appl. Cryst. , 10, 7-11 (1977)

[21] P. Khattak, D. E. Cox, J. Appl. Cryst. , 10, 405-411 (1977)

[22] Rodriguez C. J. Abstracts of the Satellite Meeting on Powder Diffraction of the XV Congress of IUCr, Toulouse, France, p. 127 (1990)

[23] R. J. Hill; H. D. Flack, J. Appl. Cryst., 20, 356-361. (1987)

[24] R. A. Young, The Rietveld Method, IUCr-Oxford University Press, (R. A. Young ed.) (1996)

[25] E. Jansen, W. Schäfer and G. Will, J. Appl. Cryst. 27 (1994) 492-496

[26] J. F. Bérar and P. Lelann, J. Appl. Crystallogr., 24, 1, (1991).

[27] C. V. Raman, K. S. Krishnan, Nature, 121, 3048 (1928) 501-502

[28] R. Poilblanc, F. Crasnier, Infrared and Raman Spectroscopies, In : Grenoble Sciences Collection, ISBN : 2-86883-744-1, EDP Sciences (2006)

[29] P. COLOMBAN, Raman Imaging of materials and Heterogeneous Devices, In : Techniques de l'Ingénieur, vol. 04, pp. RE 5 1–13, 2002.

[30] BARBILLAT J., BOUGEARD D., BUNTINX G., DELAYE M., DHAMELINCOURT P., FILLAUX F., Raman Spectroscopies, In : Techniques de l'Ingénieur, RE. P4, 1999, p. 2865-2866.

[31] Schrader B., Raman Spectroscopy, Methods and Applications. Edited by B. Schrader; VCH, Weinheim pp. 7-61 (1995).

[32] T.H. Kauffmann, N. Kokanyan, M. Fontana, J. Raman Spectrosc., Wiley, 50, 3 (2019) 418-424.

[33] G. Goudec and P. Colomban, Prog. Cryst. Growth Charact. Mater. 53, 1 (2007)

[34] I. Jankowska-Sumara, G.E. Kugel, K. Roleder and J. Dec, J. Phys. Condens. Matter 7, 3957 (1995)

[35] Goldstein, T. et al., Sci. Rep., 6, 28024 (2016).

[36] M. Azdouz, B. Manoun, M. Azrour, L. Bih, L. El Ammari, S. Benmokhtar, P. Lazor, J. Mol. Struct. 963 (2010) 258.

[37] H. Bih, L. Bih, B. Manoun, M. Azdouz, S. Benmokhtar, P. Lazor, J. Mol. Struct. 936 (2009) 147–155.

[38] B. Manouna, A. Ezzahi, S. Benmokhtar, A. Ider, P. Lazor, L. Bihd, J.M. Igartua, J. Alloys Compd. 533 (2012) 43–52

[38] F. Tutti, P. Lazor, J. Phys. Chem of Solides 69 (2008) 2535

Chapter III

Synthesis, structural refinement and spectroscopic study by Raman scattering of new solid solutions $Ba_{2-x}Sr_xMeMoO_6$; $0 \leq x \leq 2$ (Me= Ni, Mg) of double perovskite type

In this chapter we will present the results obtained in this study concerning the solid solutions $Ba_{2-x}Sr_xMeMoO_6$; $0 \leq x \leq 2$ (Me= Ni, Mg).

First, we will talk about the synthesis process of new solid solutions $Ba_{2-x}Sr_xMeMoO_6$; $0 \leq x \leq 2$ (Me= Ni, Mg) of double perovskite type.

In a second step, we will present the results of analyzes carried out as well as the characterisation of different solid solutions synthesized by X-ray diffraction technique.

We will also present a description of the crystallographic behavior of the phases as a function of the strontium composition.

Thirdly, we will present the results concerning the Raman spectroscopy analysis at ambient and at high temperature of the different solid solutions, as well as the effect of the strontium composition on the crystallographic behavior of these solutions.

Finally, we will conclude this chapter with an analysis and a discussion of the results obtained.

1. Introduction :

Perovskite is one of the most frequently encountered structures in solid-state physics. During the last few years, many experimental and theoretical investigations were devoted to the study of perovskite solids, namely the barium and strontium perovskites ($Ba_2BB'O_6$ and $Sr_2BB'O_6$), because of their interesting properties, of their more important applications, of their capacity to accommodate most of the metal ions in the periodic table with a significant number of different anions and in the objective of studying phase transitions in materials based on metal oxides having a double-perovskite structure ($A_2BB'O_6$). Furthermore, for the latter reason, several researchers have tried to substitute A/B cations by other cations of the same family and whose radii are more or less large in order to study the cation size effect on the possible appearance of phase transitions, while others have tried to study this phase transitions as a function of temperature.

Thus, Nomura and Nakagawa [1] have shown that Sr_2NiMoO_6 has a structure tetragonal at room temperature and a phase transition to cubic occurred at about 230°C. Also, Manoun et al [2] studied $Ba_{2-x}Sr_xMWO_6$ (M= Ni, Co and $0 \leq x \leq 2$) compound by Raman spectroscopy at elevated temperatures, up to 350°C, as a result, a phase transition induced by the temperature of tetragonal (I4/m) to cubic (Fm-3m), this study also showed that progressively increasing the effective size of the A-type cation by chemical substitution of the alkaline earth cation resulted in the same previous phase transition (I4/m → Fm-3m). A similar study was realized by Tamraoui et al [3] about the solid solutions $Ba_{2-x}Sr_xMgTeO_6$, where the conclusions showed the presence of phase transition sequence I2/m→I4/m→Fm-3m, as a function of temperature, the monoclinic to tetragonal transition occurs at around 102 °C and the tetragonal to cubic transition at around 303 °C, while depending on the composition, at room temperature, the study showed that two phase transitions occurred as a function of increased strontium content, from cubic to tetragonal structure at x ~ 1.5 and from the tetragonal to monoclinic structure at x ~1.9. In a recent comprehensive structural study of the double perovskites A_2NiWO_6 (A= Ba, Sr, Ca) conducted by Qingdi Zhou et al [4], progressively increasing the effective size of the A-type cation by chemical substitution of the alkaline earth cation resulted in the sequence of structural phase transitions: $P2_1/n$ → I4/m → Fm-3m. While other research [5, 6, 7], in order to demonstrate if the structural phases transition for these double perovskites, directly from I4/m to $P2_1/n$ as seen in the series $A_{2-x}Sr_xNiWO_6$ [4] or in the compounds Sr_2MeWO_6 (Me=Ca, Zn, Co), or goes via an I2/m intermediate [7], they confirmed the results obtained by Qingdi Zhou.

In connection with the foregoing, the objectives of this chapter are:

- Description of the crystal structure of new solid solutions $Ba_{2-x}Sr_xMeMoO_6$ (Me = Ni, Mg and $0 \leq x \leq 2$).
- Contribute to the search for structural phase transitions in materials based on metal oxides having a double-perovskite structure.
- Investigation of the A-cation-size effect on the possible appearance of phase transitions in $Ba_{2-x}Sr_xMeMoO_6$ (Me=Ni, Mg and $0 \leq x \leq 2$) double perovskite oxides.
- Study of the effect of substitution of barium by strontium in the A-site on the temperature induced phase transitions in these oxides.

2. Previous work on A_2NiMoO_6 and A_2MgMoO_6 (A=Ba, Sr) double perovskites

On the other hand, the investigations on the limit structures of the two solid solutions $Ba_{2-x}Sr_xMMoO_6$ (M = Ni, Mg and $0 \leq x \leq 2$) have been the subject of several studies. The double perovskites Sr_2NiMoO_6 and Ba_2NiMoO_6 were studied in the sixties and then forgotten for more than 30 years [8]. Cubic structure was observed for Ba_2NiMoO_6 [9, 10, 11] with Fm-3m (no. 225) space group and has the lattice parameter of a = 8.04 Å. The compound Sr_2NiMoO_6 has been studied in the early 1960's [12, 13], its crystal structure was initially said to have I4/mmm symmetry, with cell parameters a = 3.932 Å, and c = 3.943 Å [14] and the phase was reported to undergo a structural phase transition at 230 °C to a cubic structure [13]. However, other studies have shown the Sr_2NiMoO_6 structure crystallizes in the tetragonal system with I4/m space group and has the cell parameters a = 5.54 Å and c = 7.89 Å [8, 15, 16, 17, 18] and whose structural phase transition I4/m → Fm-3m occurs at around 277 °C [15, 19].

Similarly, the double perovskites A_2MgMoO_6 (A = Ba, Sr) have been studied by X-ray and neutron powder diffraction. Only one cubic phase (Fm-3m) of Ba_2MgMoO_6 was found with lattice parameter a= 8.110 Å [20], while tetragonal space group I4/m was found for Sr_2MgMoO_6 by Yasutake Teraoka and al [21], with lattice parameters a=5.598Å and c=7.875Å.

3. Description of the structure

The X-ray powder diffraction patterns of $Ba_{2-x}Sr_xNiMoO_6$ ($0 \leq x \leq 2$) and $Ba_{2-x}Sr_xMgMoO_6$ ($0 \leq x \leq 2$) in the 15–100° 2Θ range are showed in Figure III.1 and III.2, these diffraction patterns were assigned to :

- A cubic symmetry with the space group Fm-3m for the composition range ($0 \leq x \leq 1.3$) and ($0 \leq x \leq 0.9$) for Me=Ni and Me=Mg successively.
- A tetragonal symmetry with the space group I4/m for the composition range ($1.5 \leq x \leq 1.8$) and ($1 \leq x \leq 1.5$) for Me=Ni and Me=Mg successively.
- A monoclinic symmetry with the space group I2/m for the compositions Sr_2NiMoO_6 and for the composition range ($1.75 \leq x \leq 2$) for $Ba_{2-x}Sr_xMgMoO_6$.

We can already notice that the peaks positions shift to higher 2θ degree when increasing the value of x, which means the cell volume decreases with increasing x, this is due to the substitution of Ba^{2+} by Sr^{2+} whose ionic rays are 1.61Å and 1.44Å successively. This decrease in the cell volume is accompanied by a decrease in crystal symmetry caused by inclination of the octahedrons following the substitution of Ba^{2+} by Sr^{2+} with smaller radius compared to Ba^{2+}.

Given that, according to the X-ray diffraction analysis, a few samples from the series $Ba_{2-x}Sr_xNiMoO_6$ ($0 \leq x \leq 2$) and the samples of the series $Ba_{2-x}Sr_xMgMoO_6$ ($0 \leq x \leq 2$) contain small proportions of impurities in the form of $Ba/SrMoO_4$ and Ba_2/Sr_2MoO_5 as shown in Figure III.1 and III.2. The intensity of these impurities is particularly important in the case of the samples $Ba_{2-x}Sr_xMgMoO_6$ ($0 \leq x \leq 2$) than in the case of the samples $Ba_{2-x}Sr_xNiMoO_6$ ($0 \leq x \leq 2$).

The lattice parameters that were refined with the program FullProf as well as the unit cells volume are given in Tables III-1 and III-2. While Tables III-3 and III-4 summarize all the details of Rietveld refinement conditions of the series $Ba_{2-x}Sr_xMeMoO_6$ (Me=Ni, Mg and $0 \leq x \leq 2$). The variation of the unit cell parameters of the cubic, tetragonal and monoclinic phases in the studied composition range is illustrated in Figure III-3.

Three types of starting model are used for the refinement of the powder XRD pattern for $Ba_{2-x}Sr_xMeMoO_6$ (Me=Ni, Mg and $0 \leq x \leq 2$). Firstly, the starting model taken from Ref. [22] for the cubic lattices with space group Fm-3m. In this model Ba^{2+}/Sr^{2+}, Ni^{2+} and Mo^{6+} are

placed at 8c(1/4, 1/4, 1/4), 4b(1/2, 1/2, 1/2) and 4a(0, 0, 0) sites, respectively; the oxygen atoms occupy 24e(0, 0, z) sites.

Secondly, the starting model taken from Ref. [22] for the tetragonal lattices with space group I4/m. In this model Ba^{2+}/Sr^{2+}, Ni^{2+} and Mo^{6+} are placed at 4d(0, 1/2, 1/4), 2a(0, 0,0) and 2b(0, 0, 1/2) sites, respectively. There are two crystallographically distinct oxygen atoms, O1 (0, 0, z) and O2 (x, y, 0), present in the unit cell.

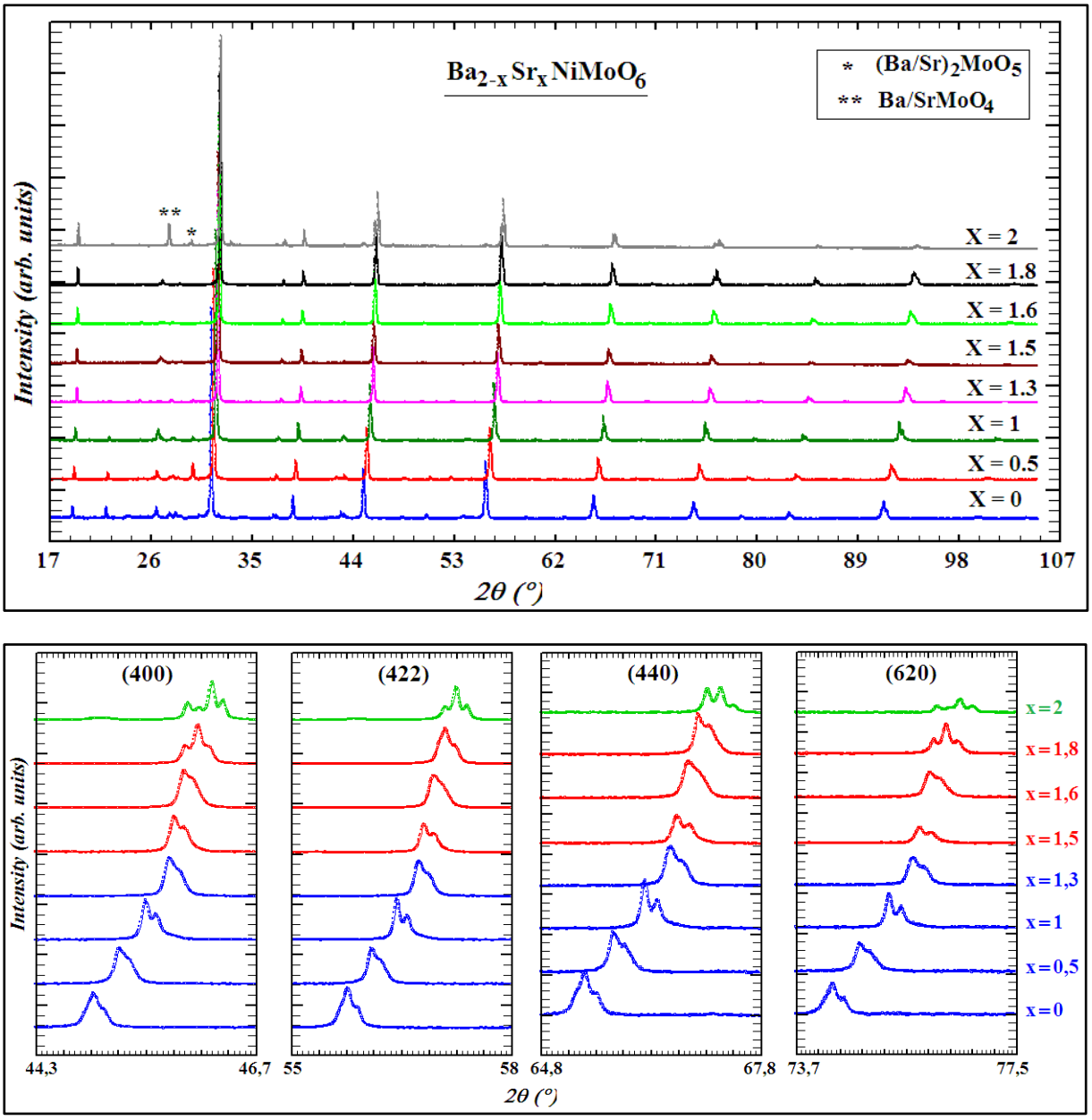

Figure III.1: X-ray powder diffraction patterns for $Ba_{2-x}Sr_xNiMoO_6$ ($0 \leq x \leq 2$). The star corresponds to the most intense reflection of the minor impurity. The Enlarged sections show the evolution of the basic (400), (422), (440) and (620) reflections.

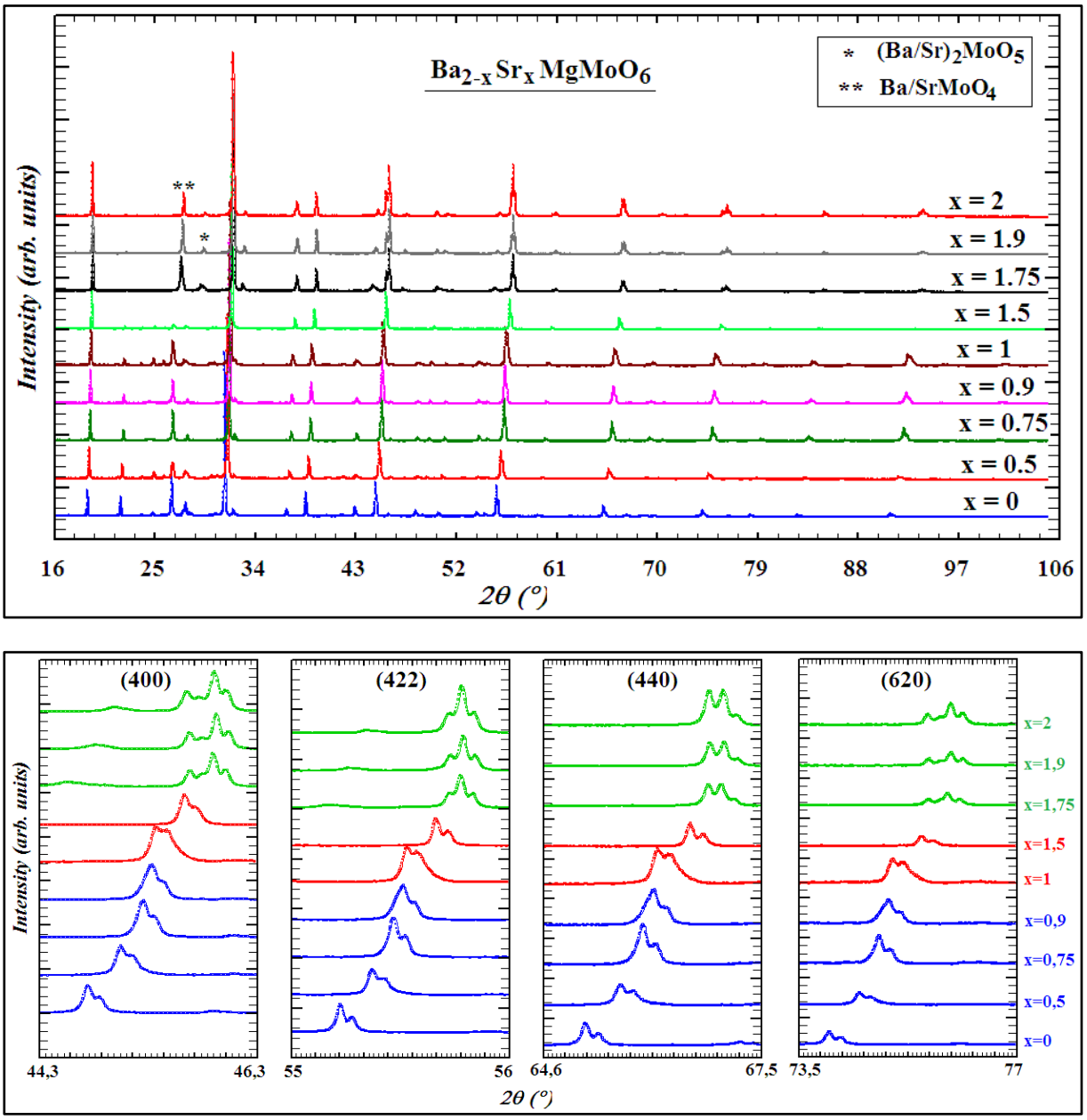

Figure III.2: X-ray powder diffraction patterns for $Ba_{2-x}Sr_xMgMoO_6$ ($0 \leq x \leq 2$). The star corresponds to the most intense reflection of the minor impurity. The Enlarged sections show the evolution of the basic (400), (422), (440) and (620) reflections.

At last, the starting model taken from Ref. [23] for the monoclinic lattices with space group I2/m. In this model, Ba^{2+}/Sr^{2+}, Ni^{2+}, and Mo^{6+} are placed at 4i (x, 1/2, z), 2c (1/2, 0, 0) and 2b (0, 1/2, 0) sites, respectively; the oxygen atoms occupy 4i(x, 0, z) and 8j(x, y, z) positions.

For all the compounds studied here, the refinements of the occupancies of all the atoms show no significant deviation from their stoichiometric values. Significantly good residuals of

the refinements are obtained. We show, in Figure III.4-(a, b, c, d and e), the typical Rietveld refinement patterns along with the difference plot at ambient temperature for compounds of the series $Ba_{2-x}Sr_xNiMoO_6$ and $Ba_{2-x}Sr_xMgMoO_6$. As can be seen in Figure III.4, for all phases, a good agreement was obtained between the experimental and the calculated diffraction profiles.

Note that, in order to reduce the impact of the intensities associated with the impurities obtained in the X-ray diffractograms of the various compositions of the series $Ba_{2-x}Sr_xMgMoO_6$ on the values of the reliability factors, we took into account the crystalline structure of the Ba/$SrMoO_4$ impurity throughout the refinement of the powder XRD pattern of this series. Ba/$SrWO_4$ crystallizes in a tetragonal lattice, with space group $I4_1/a$ at room temperature [21] and the unit cell parameters are: a = b = 5.5568 Å and c = 12.504869 Å.

Table III.1: Unit cell parameters of $Ba_{2-x}Sr_xNiMoO_6$ ($0 \leq x \leq 2$)

x	a(Å)	b(Å)	c(Å)	β(°)	V(Å^3)	Symmetry
0	8.0619(3)				523.969(4)	Cubic
0.5	8.0125(2)				514.40(3)	
1	7.9663(2)				505.55(2)	
1.3	7.9317(1)				498.99(1)	
1.5	5.6007(2)		7.9127(4)		248.20(2)	Tetragonal
1.6	5.58537(1)		7.9066(2)		246.66(1)	
1.8	5.56807(8)		7.8969(13)		244.83(1)	
2	5.5517(4)	5.5535(4)	7.8934(3)	89.963(6)	243.36(3)	Monoclinic

Table III.2: Unit cell parameters of $Ba_{2-x}Sr_xMgMoO_6$ ($0 \leq x \leq 2$)

x	a(Å)	b(Å)	c(Å)	β(°)	V(Å^3)	Symmetry
0	8.0870(1)				528.895(2)	Cubic
0.5	8.0366(3)				519.068(3)	
0.75	8.0094(1)				513.805(2)	
0.9	7.9937(1)				510.799(2)	
1	5.6411(3)		7.9745(8)		253.759(3)	Tetragonal
1.5	5.6091(1)		7.9329(1)		249.586(1)	
1.75	5.5790(3)	5.5794(3)	7.9265(2)	89.989(5)	246.736(2)	Monoclinic
1.9	5.5764(5)	5.5751(5)	7.9267(3)	89.999(9)	246.432(3)	
2	5.5735(2)	5.5729(2)	7.9240(1)	89.999(4)	246.127(1)	

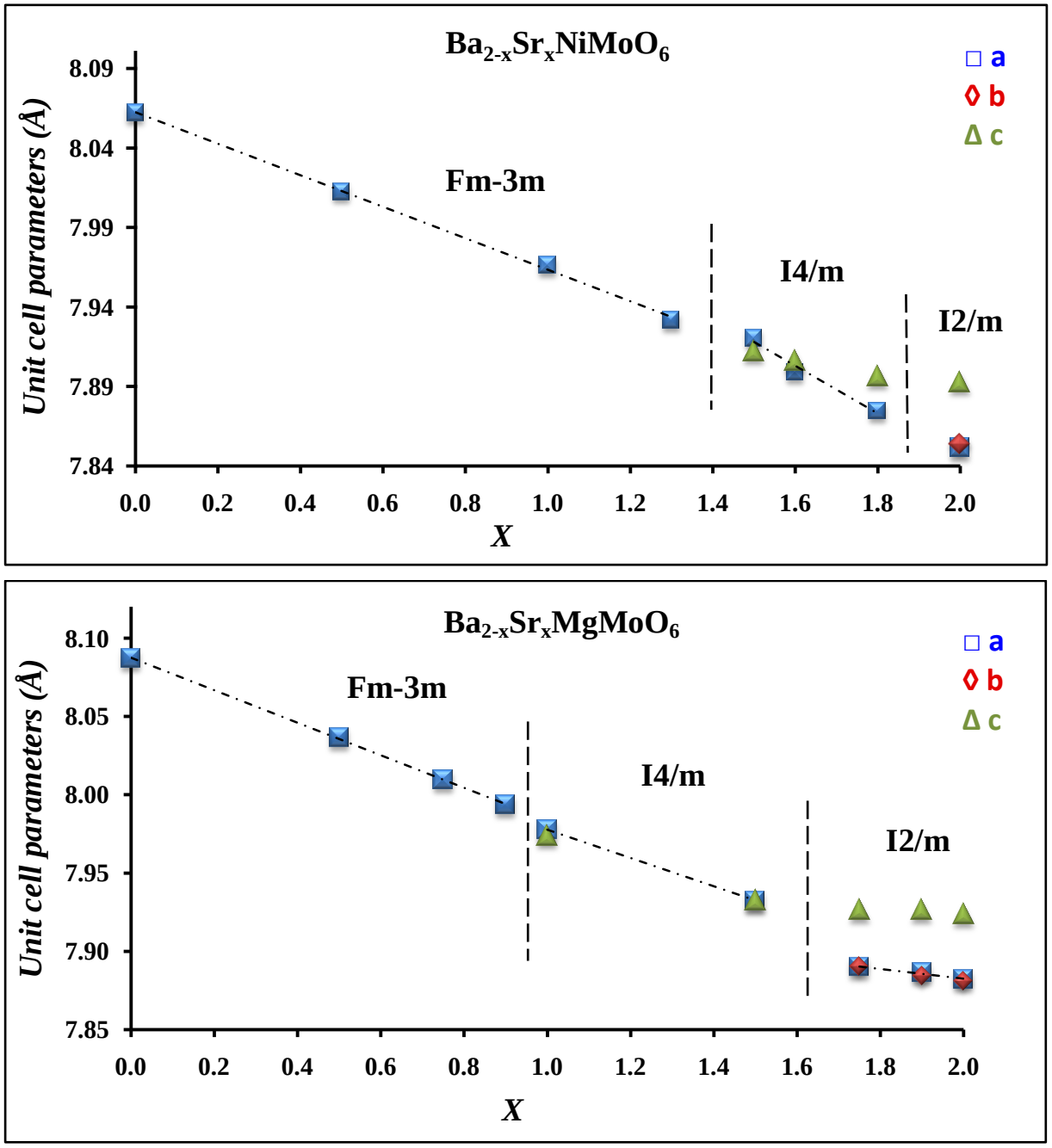

Figure III.3: Variation of the lattice parameters as a function of composition for the series $Ba_{2-x}Sr_xNiMoO_6$ (up) and $Ba_{2-x}Sr_xMgMoO_6$ (down). The *a* and *b* values in the tetragonal and monoclinic cells have been multiplied by $2^{1/2}$ for clarity. The cubic to tetragonal transition is observed between x = 1.3 and x = 1.5 for the series $Ba_{2-x}Sr_xNiMoO_6$ and between x = 0.9 and x = 1 for the series $Ba_{2-x}Sr_xMgMoO_6$, while the tetragonal to monoclinic transition is observed between x = 1.8 and x = 2 and between x = 1.5 and x = 1.75 for the series $Ba_{2-x}Sr_xNiMoO_6$ and $Ba_{2-x}Sr_xMgMoO_6$ successively.

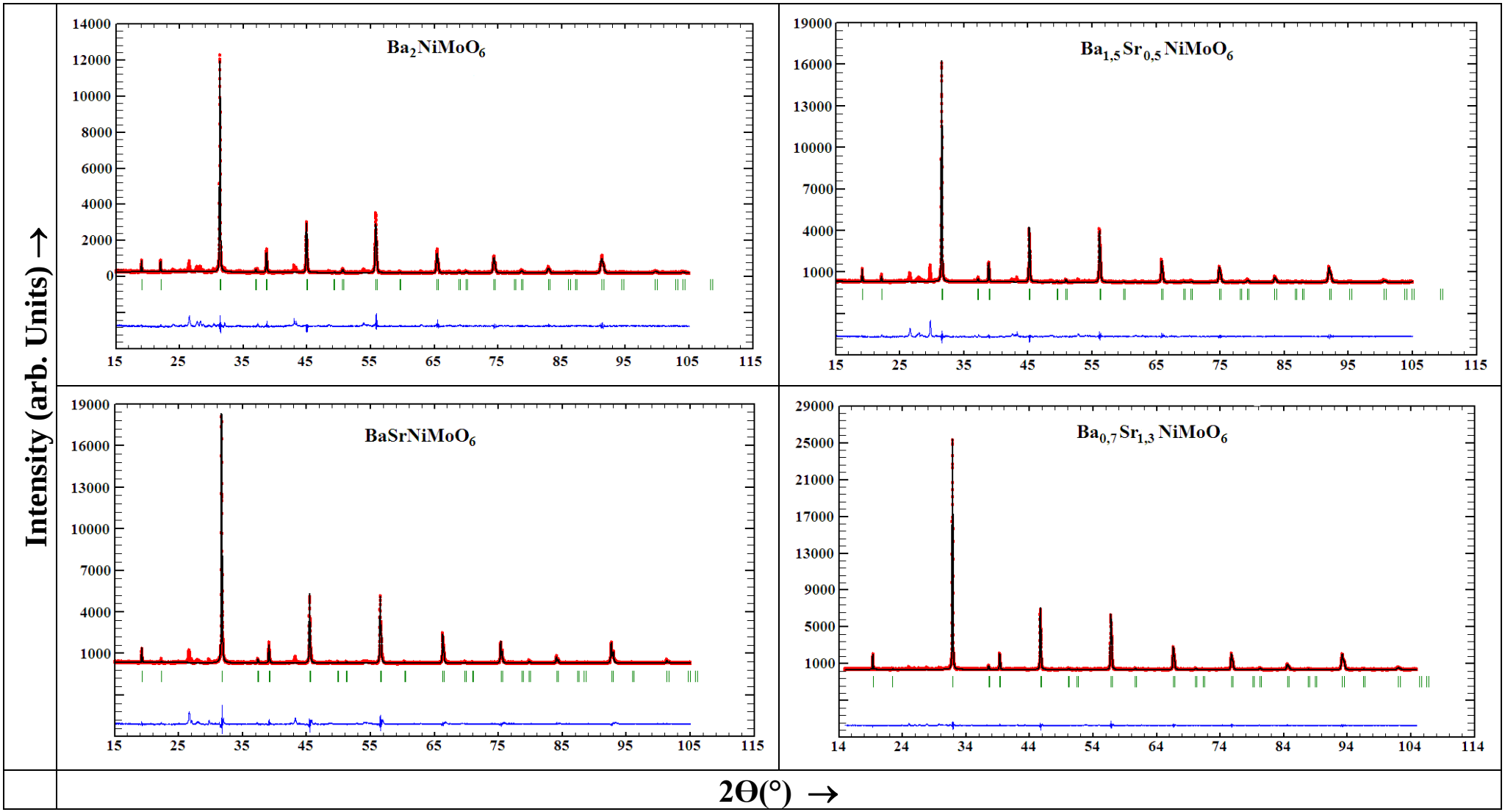

Figure III.4-a: Final Rietveld plots for compounds $Ba_{2-x}Sr_xNiMoO_6$; $0 \leq x \leq 1.3$ (Fm-3m). The upper symbols illustrate the observed data (circles) and the calculated pattern (solid line). The vertical markers show calculated positions of Bragg reflexions. The lower curve is the difference diagram. (1/5)

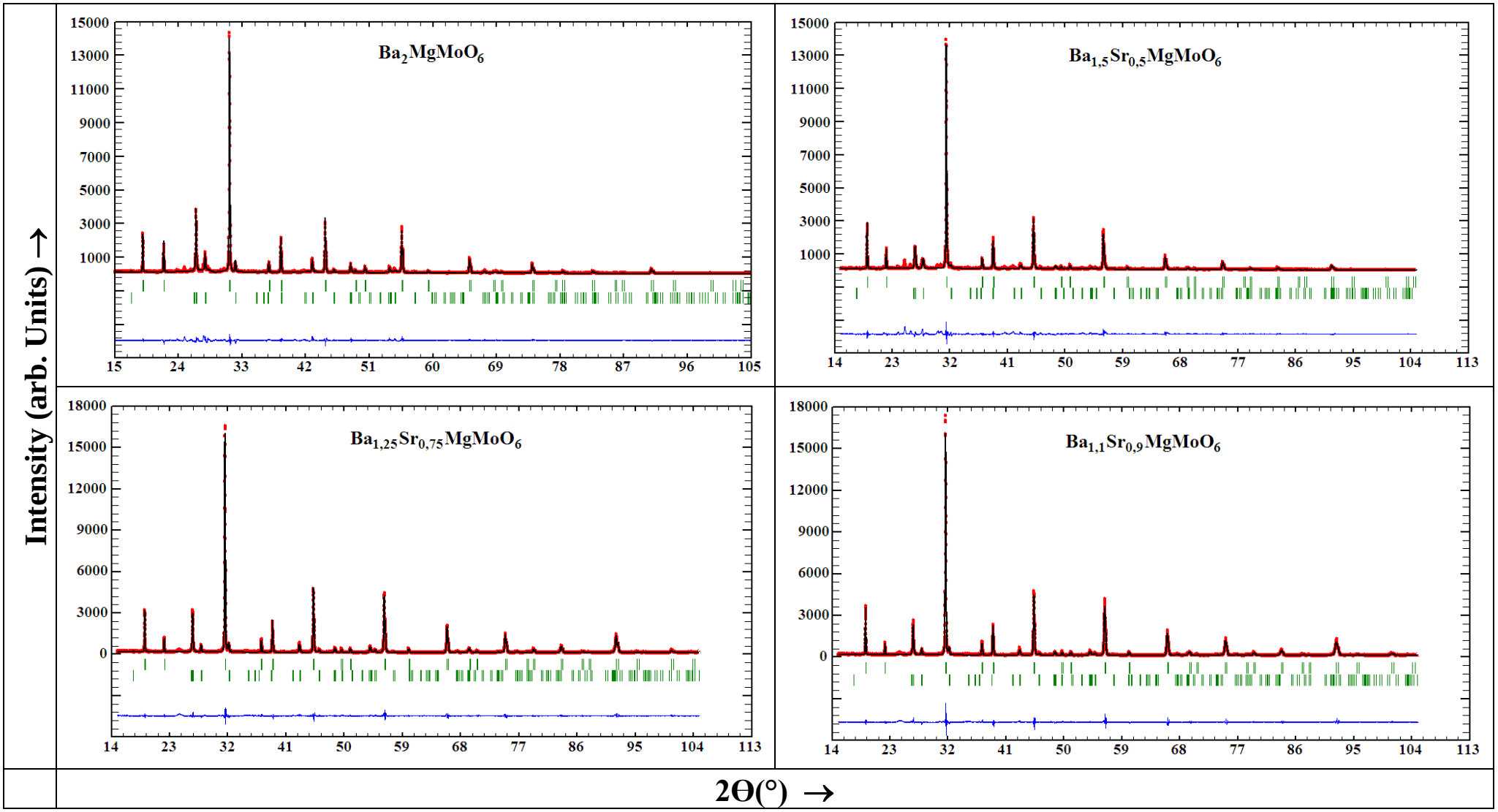

Figure III.4-b: Final Rietveld plots for compounds $Ba_{2-x}Sr_xMgMoO_6$; $0 \leq x \leq 0.9$ (Fm-3m). The upper symbols illustrate the observed data (circles) and the calculated pattern (solid line). The vertical markers show calculated positions of Bragg reflexions for $Ba_{2-x}Sr_xMgMoO_6$ (up) and for the minor impurity $BaMoO_4$ (down). The lower curve is the difference diagram. (2/5)

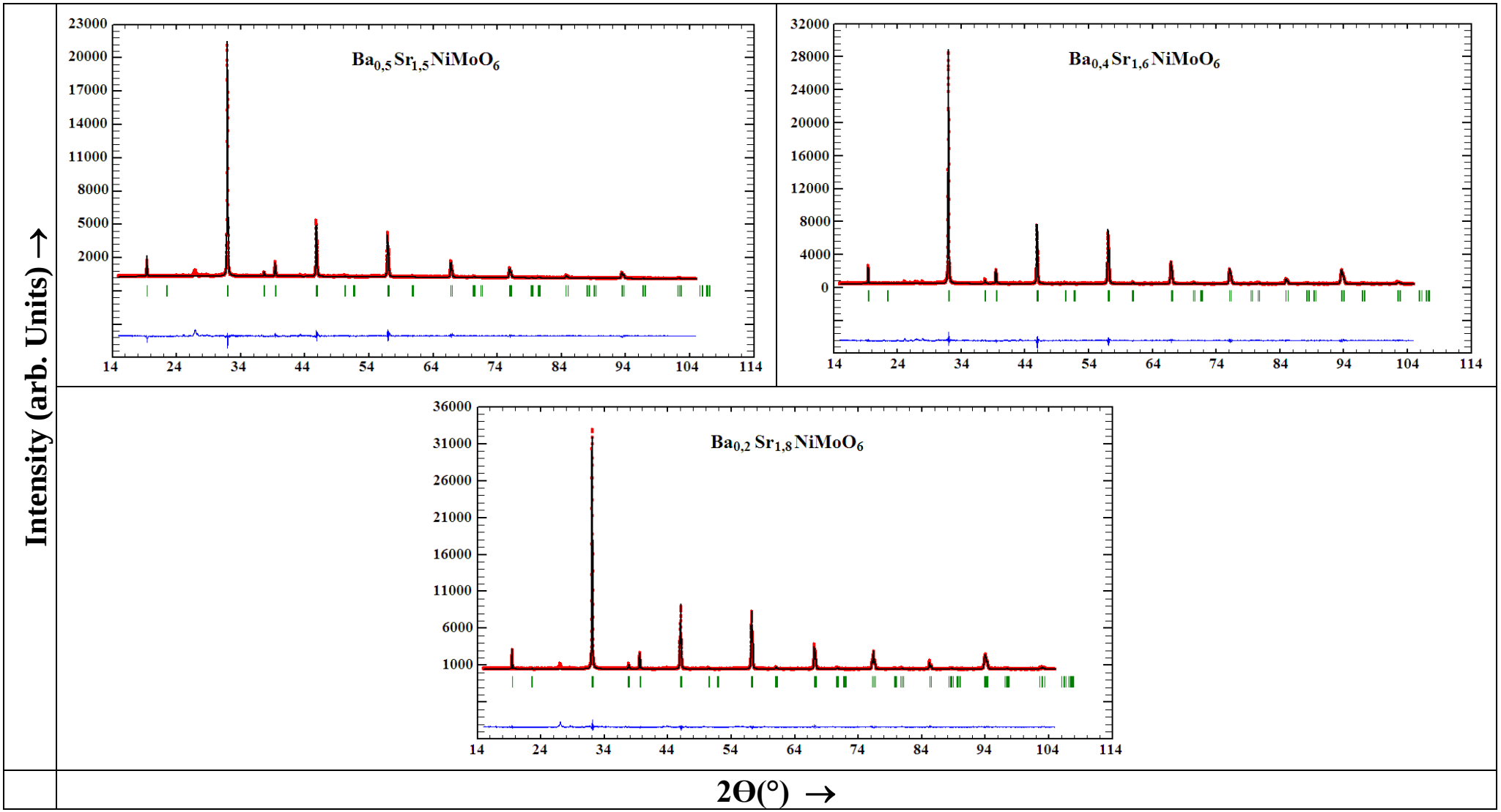

Figure III.4-c: Final Rietveld plots for compounds $Ba_{2-x}Sr_xNiMoO_6$; $1.5 \leq x \leq 1.8$ (I4/m). The upper symbols illustrate the observed data (circles) and the calculated pattern (solid line). The vertical markers show calculated positions of Bragg. The lower curve is the difference diagram. (3/5)

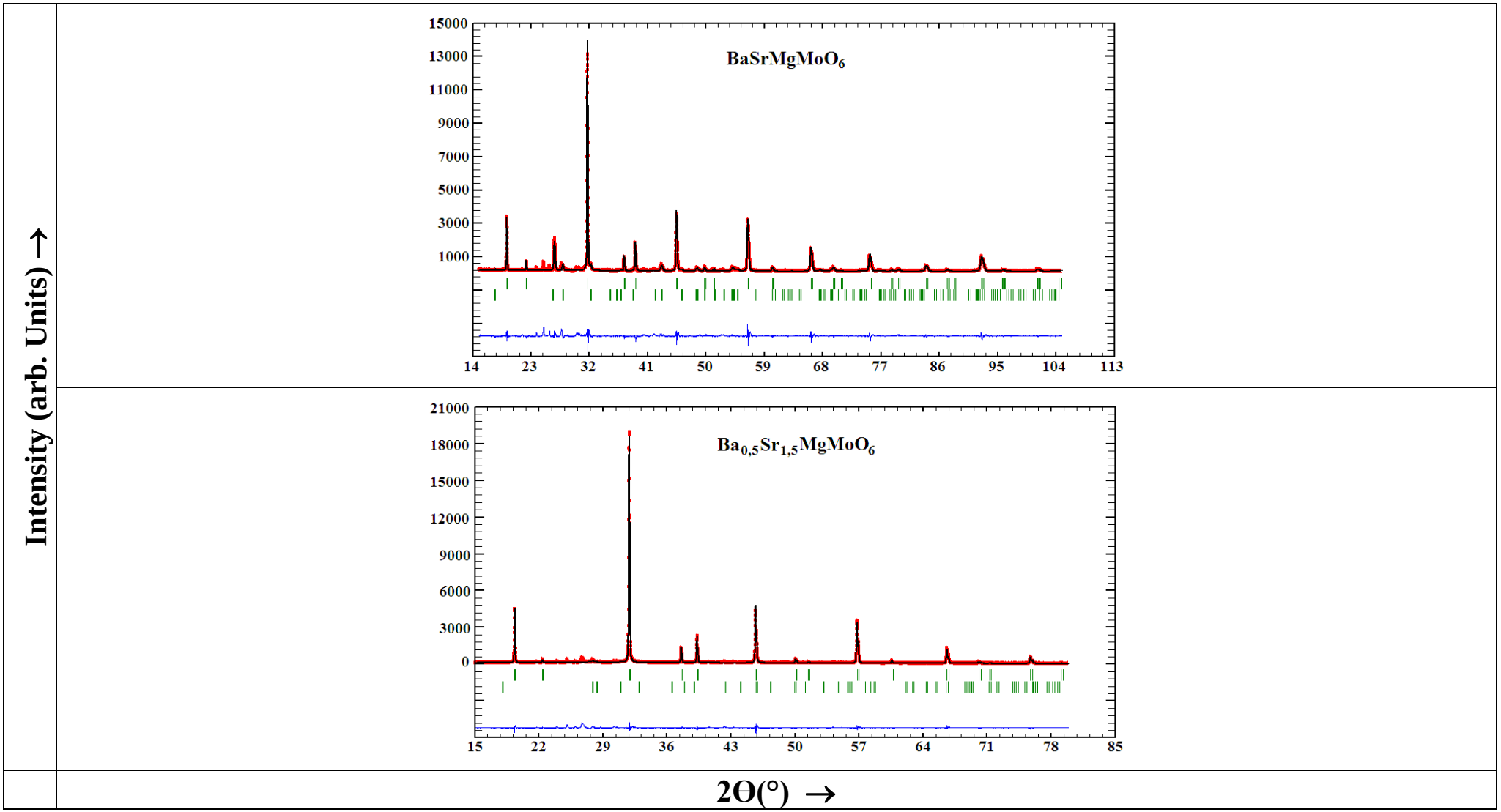

Figure III.4-d: Final Rietveld plots for compounds $Ba_{2-x}Sr_xMgMoO_6$; $1 \leq x \leq 1,5$ (I4/m). The upper symbols illustrate the observed data (circles) and the calculated pattern (solid line). The vertical markers show calculated positions of Bragg reflexions. The lower curve is the difference diagram. (4/5)

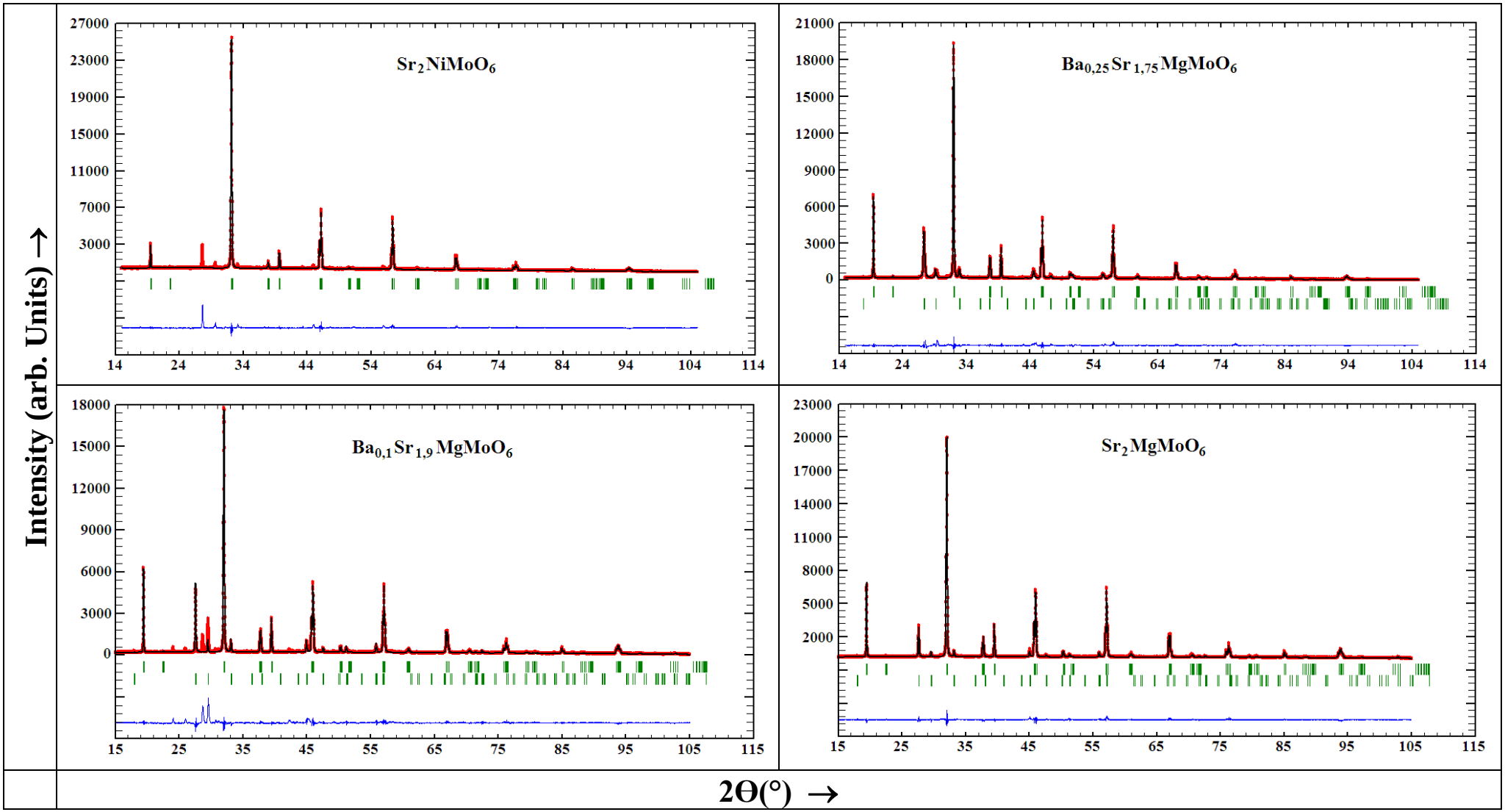

Figure III.4-e: Final Rietveld plots for compounds Sr_2NiMoO_6 (I2/m) (up- left) and $Ba_{2-x}Sr_xMgMoO_6$; $1{,}75 \leq x \leq 2$ (I2/m). The upper symbols illustrate the observed data (circles) and the calculated pattern (solid line). The vertical markers show calculated positions of Bragg reflexions. The lower curve is the difference diagram. (5/5)

Table III.3: Details of Rietveld refinement conditions of the cubic, tetragonal and monoclinic composition for $Ba_{2-x}Sr_xNiMoO_6$ ($0 \leq x \leq 2$).

Composition		***x=0.5***	***x=1***	***x=1.3***	***x=1.5***	***x=1.6***	***x=1.8***	***x=2***
Symmetry		Cubic	Cubic	Cubic	Tetragonal	Tetragonal	Tetragonal	Monoclinic
Wavelength (Å) $\lambda k\alpha_1$		1.5406	1.5406	1.5406	1.5406	1.5406	1.5406	1.5406
Step scan increment (°2θ)		0.010142	0.010142	0.010142	0.010142	0.010142	0.010142	0.010142
2θ range (°)		15-105	15-105	15-105	15-105	15-105	15-105	15-105
Program		FullProf	FullProf	FullProf	FullProf	FullProf	FullProf	FullProf
Zero point (°2θ)		-0.0073(19)	0.0016(13)	0.0504(9)	0.0241(16)	0.0312(1)	0.0080(9)	0.017(2)
Pseudo-Voigt function PV = ηL + (1-η)G		0.60(1)	0.91(1)	0.54(1)	0.66(1)	0.54(1)	0.63(1)	0.455(5)
Caglioti parameters	U	0.083(8)	0.023(4)	0.077(3)	0.060(5)	0.090(1)	0.026(2)	0.036(6)
	V	-0.005(7)	0.001(2)	-0.012(3)	-0.013(5)	-0.019(3)	0.004(2)	-0.019(5)
	W	0.005(2)	0.006(1)	0.007(1)	0.008(1)	0.008(2)	0.003(1)	0.008(1)
No. of reflections		31	29	29	86	86	86	162
No. of refined parameter		21	21	21	23	23	23	32
Space group		Fm-3m	Fm-3m	Fm-3m	I4/m	I4/m	I4/m	I2/m
a (Å)		8.0125(3)	7.9662(2)	7.9317(1)	5.6007(2)	5.58537(1)	5.56807(8)	5.5517(4)
b (Å)		_	_	_	_	_	_	5.5535(4)
c (Å)		_	_	_	7.9127(4)	7.9066(2)	7.89693(13)	7.8934(3)
β(°)		_	_	_	_	_	_	89.963(6)
V ($Å^3$)		514.40(3)	505.55(2)	498.99(1)	248.20(2)	246.66(1)	244.83(1)	243.36(3)
Atom number		4	5	5	6	6	6	5
R_F		5.89	10.1	4.64	6.66	3.81	3.99	9.14
R_B		5.34	5.94	3.11	6.04	3.14	2.95	5.47
Rp		7.50	7.65	4.64	7.14	4.62	4.29	7.25
Rwp		12.3	11.8	6.42	10.3	6.25	6.42	13.0
cRp		5.90	6.41	4.13	6.43	4.17	3.72	6.18
cRwp		8.22	8.62	5.45	8.44	5.35	4.86	9.17

Table III.4: Details of Rietveld refinement conditions of the cubic, tetragonal and monoclinic composition for $Ba_{2-x}Sr_xMgMoO_6$ ($0 \leq x \leq 2$).

Composition		***x=0.5***	***x=0.75***	***x=0.9***	***x=1***	***x=1.5***	***x=1.75***	***x=1.9***	***x=2***
Symmetry		Cubic	Cubic	Cubic	Tetragonal	Tetragonal	Tetragonal	Monoclinic	Monoclinic
Wavelength (Å) $\lambda k\alpha_1$		1.5406	1.5406	1.5406	1.5406	1.5406	1.5406	1.5406	1.5406
Step scan increment (°2θ)		0.010142	0.010142	0.010142	0.010142	0.010142	0.010142	0.010142	0.010142
2θ range (°)		15-105	15-105	15-105	15-105	15-105	15-105	15-105	15-105
Program		FullProf	FullProf	FullProf	FullProf	FullProf	FullProf	FullProf	FullProf
Zero point (°2θ)		0.0239(25)	0.0534(15)	0.0205(15)	0.0141(12)	-0.0005(5)	0.0132(11)	-0.0055(17)	-0.0302(7)
Pseudo-Voigt function PV = ηL + (1-η)G		0.382(32)	0.315(15)	0.437(16)	0.550(25)	0.525(24)	0.467(22)	0.366(35)	0.457(14)
Caglioti parameters	U	0.045(8)	0.038(2)	0.129(5)	0.149(1)	0.039(1)	0.036(3)	0.030(5)	0.035(2)
	V	0.006(5)	-0.0002(21)	-0.016(4)	-0.017(5)	-0.010(1)	-0.013(2)	-0.002(4)	-0.012(1)
	W	0.007(1)	0.0071(4)	0.007(1)	0.008(2)	0.006(2)	0.007(1)	0.006(1)	0.009(2)
No. of reflections		34	31	34	101	88	172	172	172
No. of refined parameter		33	35	29	29	18	40	40	40
Space group		Fm-3m	Fm-3m	Fm-3m	I4/m	I4/m	I2/m	I2/m	I2/m
a (Å)		8.0366(3)	8.0094(1)	7.9937(1)	5.6411(3)	5.6091(1)	5.5790(3)	5.5764(5)	5.5735(2)
b (Å)		_	_	_	_	_	5.5794(3)	5.5751(5)	5.5729(2)
c (Å)		_	_	_	7.9745(8)	7.9328(1)	7.9265(2)	7.9267(3)	7.9240(1)
β(°)		_	_	_	_	_	89.989(5)	89.9992(94)	89.999(4)
V ($Å^3$)		519.07(3)	513.81(2)	510.79(2)	253.76(3)	249.58(1)	246.74(2)	246.43(3)	246.12(1)
Atom number		4	5	5	6	6	6	6	5
R_F		3.69	2.05	1.92	3.59	2.10	4.29	5.24	3.78
R_B		4.50	2.70	2.96	3.86	2.79	3.09	4.01	2.97
Rp		12.0	6.93	7.69	9.99	8.96	7.80	10.3	6.24
Rwp		17.7	9.38	10.1	14.1	14.2	11.7	17.6	8.50
cRp		12.0	6.93	7.69	9.99	8.96	7.81	10.1	6.22
cRwp		17.7	9.38	10.1	14.1	14.2	11.7	17.4	8.49

The refined positions coordinates for $Ba_{2-x}Sr_xNiMoO_6$ ($0 \leq x \leq 2$) and $Ba_{2-x}Sr_xMgMoO_6$ ($0 \leq x \leq 2$) in the cubic, tetragonal and monoclinic compositions along with other crystallographic data are given in Tables III-5 and III-6.

Note that for the compositions $Ba_{0.5}Sr_{1.5}NiMoO_6$ and $BaSrMgMoO_6$, The refinements of powder X-ray diffraction patterns were carried out successfully with cubic symmetry (Fm-3m) and tetragonal symmetry (I4/m). While, the reliability factors were much better for these two compositions in a tetragonal symmetry. Similarly, for the compositions Sr_2NiMoO_6, the reliability factors favored a monoclinic symmetry (I2/m), although the refinement of powder X-ray diffraction pattern has been successfully carried out with tetragonal symmetry (I4/m).

The analysis of refined crystallographic parameters in $Ba_{2-x}Sr_xNiMoO_6$ ($0 \leq x \leq 1.3$) and $Ba_{2-x}Sr_xMgMoO_6$ ($0 \leq x \leq 0.9$) indicates that the Ni^{2+}, Mg^{2+} and Mo^{6+} are octahedrally coordinated with the oxygen atoms. The NiO_6 and MoO_6 octahedra on the one hand, and the MgO_6 and MoO_6 octahedra, on the other hand, are alternatively connected and extended in three dimensions. The O(1) atoms connect the NiO_6 and MoO_6 octahedra and the MgO_6 and MoO_6 octahedra along the three directions. The typical Ni–O–Mo and Mg–O–Mo angle for all compounds of $Ba_{2-x}Sr_xNiMoO_6$ ($0 \leq x \leq 1.3$) and of $Ba_{2-x}Sr_xMgMoO_6$ ($0 \leq x \leq 0.9$) successively, is constrained to 180° by the space group Fm-3m. The O(1) positional coordinates are restricted to (0,0,z), indicating no tilt with respect to a, b and c-axes, and corresponds to the $a^0a^0a^0$ in Glazer's notation [24]. A (1 0 0) projection of the $BaSrNiMoO_6$ unit cell indicating the typical polyhedral arrangement for these cubic compositions is shown in Figure III-5.

The analysis of various inter-atomic distances (Table III-7) shows that Ba/Sr atoms form Ba/SrO_{12} polyhedra with the Ba/Sr–O bond lengths around 2.83Å for $Ba_{2-x}Sr_xNiMoO_6$ and around 2.84Å for $Ba_{2-x}Sr_xMgMoO_6$.

For $Ba_{2-x}Sr_xNiMoO_6$, the Ni^{2+} and Mo^{6+} have octahedral coordination with the Ni–O bond lengths around 2.05Å and the Mo–O bonds around 1.94Å. Whereas for $Ba_{2-x}Sr_xMgMoO_6$ The Mg^{2+} and Mo^{6+} have octahedral coordination with the Mg–O bond lengths around 2.12Å and the Mo–O bonds around 1.90Å

The analysis of refined crystallographic parameters for the tetragonal compositions in $Ba_{2-x}Sr_xNiMoO_6$ ($1.5 \leq x \leq 1.8$) and $Ba_{2-x}Sr_xMgMoO_6$ ($1 \leq x \leq 1.5$) indicates that the Ni^{2+}, Mg^{2+} and Mo^{6+} are octahedrally coordinated with the oxygen atoms. The NiO_6 and MoO_6 octahedra on the one hand, and the MgO_6 and MoO_6 octahedra, on the other hand, are alternatively connected and extended in three dimensions. The O(2) atoms connect the NiO_6/MgO_6 and

MoO_6 octahedra along the c-axis. In ab-plane NiO_6/MgO_6 and MoO_6 octahedra are connected through the O(1) atoms.

Table III.5: Refined structural parameters for $Ba_{2-x}Sr_xNiMoO_6$ ($0 \leq x \leq 2$).

x	*Atom*	*x*	*y*	*z*	*B(Å²)*	*Occ.*
0	Mo	0	0	0	-0.189	1
	Ni	0,5	0,5	0,5	0.277	1
	Ba	0,25	0,25	0,25	0.171	2
	O1	0	0	0,2418(10)	1.010	6
0.5	Mo	0	0	0	0.199	1
	Ni	0,5	0,5	0,5	0.630	1
	Ba/Sr	0,25	0,25	0,25	0.345	1,5/0,5
	O1	0	0	0,2436(9)	1.120	6
1	Mo	0	0	0	0.491	1
	Ni	0,5	0,5	0,5	0.407	1
	Ba/Sr	0,25	0,25	0,25	0.671	1/1
	O1	0	0	0,2421(9)	1.620	6
1.3	Mo	0	0	0	0.568	1
	Ni	0,5	0,5	0,5	0.267	1
	Ba/Sr	0,25	0,25	0,25	0.568	0,7/1,3
	O1	0	0	0,2440(4)	0.964	6
1.5	Mo	0	0	0,5	2.718	1
	Ni	0	0	0	2.723	1
	Ba/Sr	0	0, 5	0,25	3.280	0,5/1,5
	O1	0	0	0.2579(47)	3.648	2
	O2	0.2421(49)	0.2823(62)	0	3.648	4
1.6	Mo	0	0	0,5	0.474	1
	Ni	0	0	0	0.241	1
	Ba/Sr	0	0,5	0,25	0.846	0,4/1,6
	O1	0	0	0.2704(32)	0.913	2
	O2	0.2397(15)	0.2876(21)	0	0.913	4
1.8	Mo	0	0	0,5	0.485	1
	Ni	0	0	0	0.650	1
	Ba/Sr	0	0,5	0,25	0.896	0,2/1,8
	O1	0	0	0.2657(18)	1.415	2
	O2	0.2877(25)	0.2416(19)	0	1.415	4
2	Mo	0	0,5	0	0.670	1
	Ni	0,5	0	0	0.300	1
	Sr	0.4944(31)	0,5	0.2482(19)	0.915	2
	O1	0.5509(77)	0	0.2612(34)	1.004	2
	O2	0.2641(48)	0.2835(38)	0.0160(37)	1.004	4

Table III.6: Refined structural parameters for $Ba_{2-x}Sr_xMgMoO_6$ ($0 \leq x \leq 2$).

x	*Atom*	*x*	*y*	*z*	*B(Å2)*	*Occ.*
0	Mo	0	0	0	0.016	1
	Mg	0,5	0,5	0,5	-0.159	1
	Ba	0,25	0,25	0,25	0.726	2
	O1	0	0	0.2354(23)	0.398	6
1,5	Mo	0	0	0	0.393	1
	Mg	0,5	0,5	0,5	0.237	1
	Ba/Sr	0,25	0,25	0,25	0.345	1,5/0,5
	O1	0	0	0.2392(7)	0.952	6
0,75	Mo	0	0	0	0.491	1
	Mg	0,5	0,5	0,5	0.407	1
	Ba/Sr	0,25	0,25	0,25	0.671	1,25/0,75
	O1	0	0	0.2359(4)	1.620	6
0,9	Mo	0	0	0	0.568	1
	Mg	0,5	0,5	0,5	0.267	1
	Ba/Sr	0,25	0,25	0,25	0.568	1,1/0,9
	O1	0	0	0.2358(4)	0.964	6
1	Mo	0	0	0,5	0.131	1
	Mg	0	0	0	-1.053	1
	Ba/Sr	0	0, 5	0,25	1.452	1/1
	O1	0	0	0.2322(16)	-1.197	2
	O2	0.7385(35)	0.3082(42)	0	-1.197	4
1.5	Mo	0	0	0,5	0.474	1
	Mg	0	0	0	0.241	1
	Ba/Sr	0	0,5	0,25	0.846	0,5/1,5
	O1	0	0	0.2684(13)	0.913	2
	O2	0.2163(19)	0.2813(22)	0	0.913	4
1,75	Mo	0	0,5	0	1.140	1
	Mg	0,5	0	0	-1.328	1
	Ba/Sr	0.5048(22)	0,5	0.2536(15)	3.149	0,25/1,75
	O1	0,4547(65)	0	0.2605(12)	-0.616	2
	O2	0.2131(20)	0.2269(21)	0.9739(16)	-0.275	4
1,9	Mo	0	0,5	0	0.739	1
	Mg	0,5	0	0	-2.033	1
	Ba/Sr	0.5053(25)	0,5	0.2521(19)	1.866	0,1/1,9
	O1	0.4289(51)	0	0.2575(18)	-2.976	2
	O2	0.2177(42)	0.2364(44)	0.9824(35)	0.031	4
2	Mo	0	0,5	0	0.472	1
	Mg	0,5	0	0	-1.036	1
	Sr	0.5035(12)	0,5	0.2527(6)	0.312	2
	O1	0.4383(27)	0	0.2561(7)	-2.113	2
	O2	0.2166(16)	0.2312(17)	0.9846(17)	0.058	4

The typical Ni–O(1)–Mo and Mg–O(1)–Mo bonds angle in $Ba_{2-x}Sr_xNiMoO_6$ ($1.5 \leq x \leq 1.8$) and $Ba_{2-x}Sr_xMgMoO_6$ ($1 \leq x \leq 1.5$) successively, is constrained to 180° by space group I4/m and O(1) position coordinates (0, 0, z), indicating no tilt with respect to c-axis. The appreciable tilt of the octahedra is observed from the Ni–O(2)–Mo (169°) and Mg–O(2)–Mo (167°) bond angles. The tilt pattern of the octahedral units satisfies the ($a°a°c^-$) tilt system in Glazer's notation [24,25]. A (001) projection of the $Ba_{0.4}Sr_{1.6}NiMoO_6$ unit cell indicating the typical polyhedral arrangement and the tilt pattern is shown in Figure III-5. In the same figure we illustrate the Ba/Sr environment in the tetragonal structure (I4/m).

For $Ba_{2-x}Sr_xNiMoO_6$ ($1.5 \leq x \leq 1.8$), the analysis of various inter-atomic distances (Table III-8) shows that Ba/Sr atoms form Ba/SrO_{12} polyhedra with the Ba/Sr–O bond lengths ranging between 2.66 and 2.93Å, and the average d value is approximately 2.80Å. The Ni^{2+} and Mo^{6+} have octahedral coordination with the Ni–O bond lengths ranging between 2.04 and 2.14Å and the Mo–O bonds lengths ranging between 1.82 and 1.91 Å.

Whereas for $Ba_{2-x}Sr_xMgMoO_6$ ($1 \leq x \leq 1.5$), the analysis of various inter-atomic distances (Table III-8) shows that Ba/Sr atoms form Ba/SrO_{12} polyhedra with the Ba/Sr–O bond lengths ranging between 2.63 and 2.99Å, and the average d value is approximately 2.82Å. The Mg^{2+} and Mo^{6+} have octahedral coordination with the Mg–O bond lengths ranging between 1.85Å and 2.28Å and the Mo–O bonds lengths ranging between 1.73 and 2.14 Å.

Table III.7: Selected inter-atomic distances (Å) and O-Mo-O angles for $Ba_{2-x}Sr_xNiMoO_6$ ($0 \leq x \leq 1.3$) and $Ba_{2-x}Sr_xMgMoO_6$ ($0 \leq x \leq 0.9$)

Cubic	**$Ba_{2-x}Sr_xNiMoO_6$**				**$Ba_{2-x}Sr_xMgMoO_6$**			
	x=0	***x=0.5***	***x=1***	***x=1.3***	***x=0***	***x=0.5***	***x=0.75***	***x=0.9***
6× Mo-O	1.949(2)	1.952(2)	1.929(2)	1.935(1)	1.904(1)	1.922(1)	1.889(1)	1.885(1)
6× Ni-O	2.082(2)	2.054(2)	2.055(2)	2.031(1)	—	—	—	—
6× Mg-O	—	—	—	—	2.139(1)	2.096(1)	2.116(1)	2.112(1)
12× Ba/Sr-O	2.851(2)	2.833(1)	2.817(1)	2.805(1)	2.862(1)	2.843(9)	2.834(1)	2.828(1)
3× O-Mo-O	180	180	180	180	180	180	180	180
12× O-Mo-O	90	90	90	90	90	90	90	90

Table III.8: Selected inter-atomic distances (Å) and O-Mo-O angles for $Ba_{2-x}Sr_xNiMoO_6$ ($1.5 \leq x \leq 1.8$) and $Ba_{2-x}Sr_xMgMoO_6$ ($1 \leq x \leq 1.5$)

Tetragonal	$Ba_{2-x}Sr_xNiMoO_6$			$Ba_{2-x}Sr_xMgMoO_6$	
	x=1.5	***x=1.6***	***x=1.8***	***x=1***	***x=1.5***
2× Mo-O1	1.915(40)	1.8152(1)	1.850(14)	2.136(13)	1.838(1)
4× Mo-O2	1.892(31)	1.8764(1)	1.861(10)	1.725(19)	2.009(1)
<Mo-O>	1.899(39)	1.8560(1)	1.8575(9)	1.862(7)	1.952(1)
2× Ni-O1	2.042(40)	2.1381(2)	2.098(14)	—	—
4× Ni-O2	2.081(31)	2.0912(3)	2.093(11)	—	—
<Ni-O>	2.068(39)	2.107(1)	2.0948(10)	—	—
2× Mg-O1	—	—	—	1.852(13)	2.129(1)
4× Mg-O2	—	—	—	2.281(20)	1.990(1)
<Mg-O>	—	—	—	2.138(7)	2.037(1)
4 × Ba/Sr-O1	2.8011(9)	2.7973(1)	2.7868(6)	2.824(1)	2.808(1)
4 × Ba/Sr-O2	2.915(23)	2.9326(6)	2.922(8)	2.708(13)	2.993(1)
4 × Ba/Sr-O2	2.691(21)	2.6661(4)	2.665(7)	2.966(14)	2.629(1)
<Ba/Sr-O>	2.802(52)	2.799(21)	2.7912(6)	2.833(3)	2.810(1)
1× O1-Mo-O1	180	180	180	180	180
8× O1-Mo-O2	90	90	90	90	90
4× O2-Mo-O2	90	90	90	90	90
2× O2-Mo-O2	180	180	180	180	180

Note that the distances of Mo–O are considerably shorter than expected (1.99 Å) from the Shannon ionic radii of Mo^{6+} (0.59Å) and O^{2-} (1.4 Å). The Ni–O and Mg–O values are very close to what is expected: 2.09Å and 2.12 successively (Table III.8). It seems that Mo–O contracts when the Ba^{2+} substitution by Sr^{2+} becomes very important. What is more important is that when the strontium amount increases in the cubic, tetragonal and monoclinic compositions, the Mo-O changes considerably on passing from one symmetry to another, which is a great sign of, on the one hand, the cubic to tetragonal transition and on the other hand, of the tetragonal to monoclinic transition. This contraction is not due to the cations

Ni^{2+}/Mg^{2+} since these one entirely occupy the site of B while Mo^{6+} occupies the site of B' in $AA'BB'O_6$.

Table III.9: Selected inter-atomic distances (Å) and O-Mo-O angles for Sr_2NiMoO_6 and $Ba_{2-x}Sr_xMgMoO_6$ ($1.75 \leq x \leq 2$)

Monoclinic	$Ba_{2-x}Sr_xNiMoO_6$	$Ba_{2-x}Sr_xMgMoO_6$		
	x=2	***x=1.75***	***x=1.9***	***x=2***
2× Mo-O1	1.907(24)	1.915(10)	1.963(15)	1.964(6)
4× Mo-O2	1.898(26)	1.942(11)	1.914(22)	1.928(9)
<Mo-O>	1.901(3)	1.933(4)	1.930(8)	1.940(3)
2× Ni-O1	2.080(24)	—	—	—
4× Ni-O2	2.054(25)	—	—	—
<Ni-O>	2.063(1)	—	—	—
2× Mg-O1	—	2.080(10)	2.079(15)	2.058(6)
4× Mg-O2	—	2.052(11)	2.055(22)	2.042(9)
<Mg-O>	—	2.061(4)	2.063(8)	2.047(3)
2 × Ba/Sr -O1	2.797(6)	2.804(4)	2.820(5)	2.810(2)
1 × Ba/Sr -O1	3.027(47)	2.569(35)	2.421(30)	2.462(18)
1 × Ba/Sr -O1	2.527(47)	3.015(35)	3.157(30)	3.114(18)
2 × Ba/Sr -O2	2.536(32)	3.145(16)	3.052(30)	3.052(13)
2 × Ba/Sr -O2	2.755(32)	2.837(15)	2.828(29)	2.865(12)
2 × Ba/Sr -O2	2.828(31)	2.449(16)	2.542(30)	2.539(13)
2 × Ba/Sr -O2	3.034(31)	2.784(16)	2.778(31)	2.738(13)
< Ba/Sr -O>	2.788(93)	2.802(6)	2.802(8)	2.799(37)
1 × O1-Mo-O1	180	180	180	180
4 × O1-Mo-O2	87.2(20)	88.6(10)	86.8(15)	87.3(6)
4 × O1-Mo-O2	93(2)	91.4(9)	93.2(16)	92.7(7)
2 × O2-Mo-O2	180	180	180	180
2 × O2-Mo-O2	102(2)	103.2(9)	100.5(17)	102.0(7)
2 × O2-Mo-O2	78.4(16)	76.8(7)	79.5(15)	78.0(6)

The analysis of refined crystallographic parameters for the monoclinic compositions in Sr_2NiMoO_6 and $Ba_{2-x}Sr_xMgMoO_6$ ($1.75 \leq x \leq 2$) indicates that the Ni^{2+} and Mo^{6+} are octahedrally coordinated with the oxygen atoms. The NiO_6 and MoO_6 octahedra on the one hand, and the MgO_6 and MoO_6 octahedra, on the other hand, are alternatively connected and extended in three dimensions. The O(1) atoms connect the NiO_6/MgO_6 and MoO_6 octahedra along the c-axis. In ab-plane NiO_6/MgO_6 and MoO_6 octahedra are connected through the O(2) atoms. The typical bond angles Ni–O(1)–Mo and Ni–O(2)–Mo for Sr_2NiMoO_6 are constrained to 163,6° and to 166,8° successively by space group I2/m. While, in the same space group, the typical bond angles Mg–O(1)–Mo and Mg–O(2)–Mo for $Ba_{2-x}Sr_xMgMoO_6$ ($1.75 \leq x \leq 2$) are constrained to 161,3° and to 164,86° successively. While O(1) position coordinates (x, 0, z) and (x, y, z) for O(2), indicating the presence of appreciable tilt. The tilt pattern of the octahedral units satisfies the ($a^ob^-b^-$) tilt system in Glazer's notation [24,25]. A (110) projection of the Sr_2NiMoO_6 unit cell indicating the typical polyhedral arrangement and the tilt pattern is shown in Figure III-5. In the same figure we illustrate the Ba/Sr environment in the monoclinic structure (I2/m).

For Sr_2NiMoO_6, the analysis of various inter-atomic distances (Table III.9) shows that Sr atoms form SrO_{12} polyhedra with the Sr–O bond lengths ranging between 2.53 and 3.03Å, and the average d value is approximately 2.79Å. The Ni^{2+} and Mo^{6+} have octahedral coordination with the Ni–O bond lengths ranging between 2.05 and 2.08Å and the Mo–O bond lengths ranging between 1.88 and 1.91 Å.

Whereas for $Ba_{2-x}Sr_xMgMoO_6$ ($1.75 \leq x \leq 2$), the analysis of various inter-atomic distances (Table III.9) shows that Ba and Sr atoms form Ba/SrO_{12} polyhedra with the Ba/Sr–O bond lengths ranging between 2.42 and 3.16Å, and the average d value is approximately 2.80Å. The Mg^{2+} and Mo^{6+} have octahedral coordination with the Mg–O bond lengths ranging between 2.04 and 2.08Å and the Mo–O bond lengths ranging between 1.91 and 1.96Å.

As explained earlier in the first chapter, it possible to quantify the deformation of the perovskite structure, with respect to the ideal structure, leading to the formation of phases with lower symmetry, and thus to illustrate the structural phase transitions. Indeed, The changes of the slope of the tolerance factor (obtained from the observed distances) as a function of the composition, represents a useful way to illustrate this transitions [22].

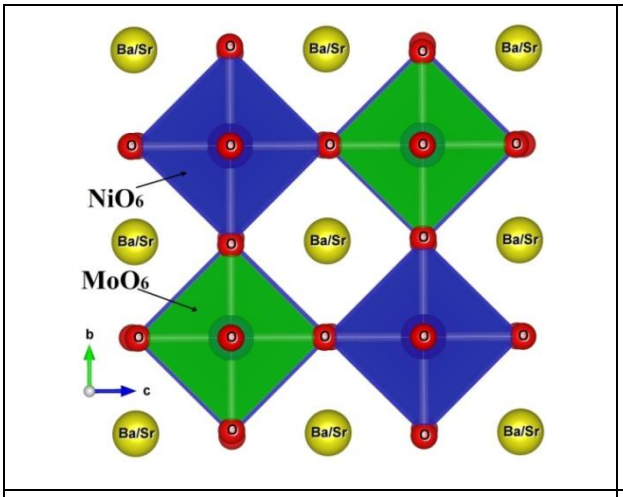

(100) projection of $BaSrNiMoO_6$ (Fm-3m)

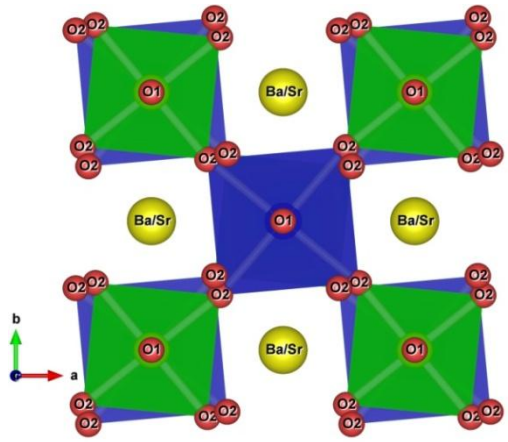

(001) projection of $Ba_{0.4}Sr_{1.6}NiMoO_6$ (I4/m)

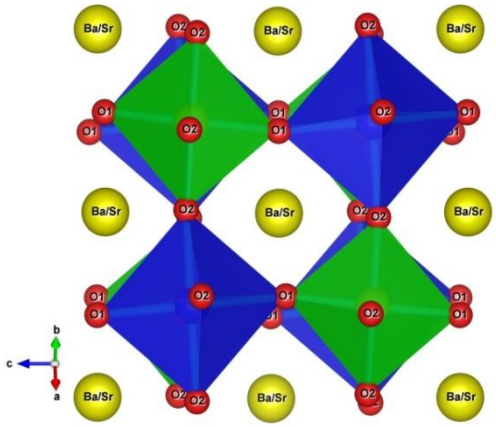

(110) projection of Sr_2NiMoO_6 (I2/m)

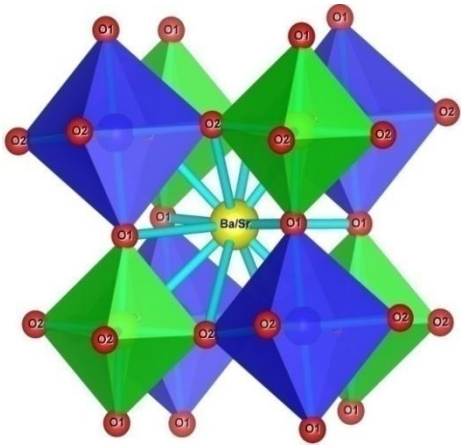

The Ba/Sr environment in the monoclinic structure (I2/m)

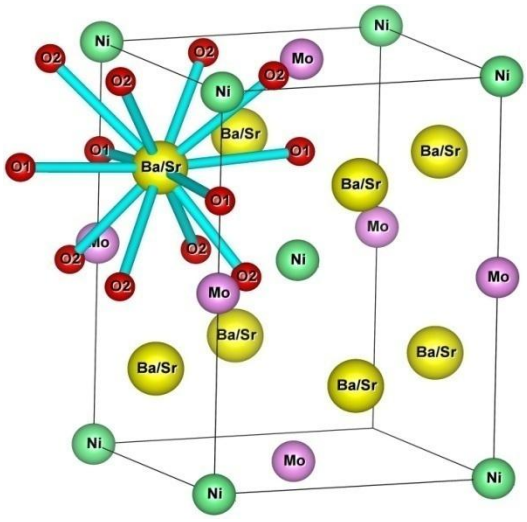

The Ba/Sr environment in the tetragonal structure (I4/m)

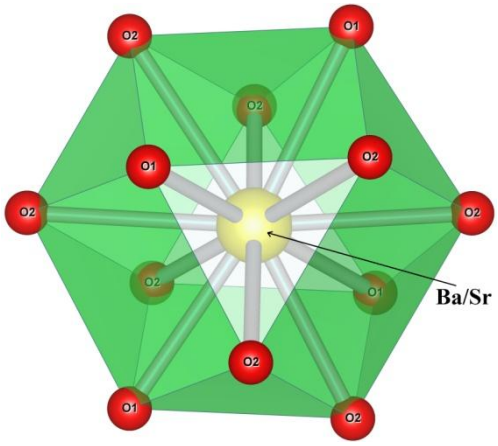

The Ba/Sr cation in cuboctahedral site in the monoclinic structure (I2/m)

Figure III.5: The typical polyhedral arrangement, the Ba/Sr environment and illustrations of the effect of tilting of the MoO_6, NiO_6 and MgO_6 octahedra in the different space group structure in $Ba_{2-x}Sr_xMeMoO_6$ (Me=Ni, Mg and $0 \leq x \leq 2$).

Figure III-6 shows the observed tolerance factor (calculated from the distances obtained from the Rietveld refinements) as a function of the strontium amount in $Ba_{2-x}Sr_xNiMoO_6$ and $Ba_{2-x}Sr_xMgMoO_6$. The first phase transition from cubic to tetragonal is well illustrated in the figure between the compositions $1.3 \leq x \leq 1.5$ and between the compositions $0.9 \leq x \leq 1$ for $Ba_{2-x}Sr_xNiMoO_6$ and $Ba_{2-x}Sr_xMgMoO_6$ successively, but the second phase transition from tetragonal to monoclinic is illustrated in the same figure between the compositions $1.8 \leq x \leq 2$ and between the compositions $1.5 \leq x \leq 1.75$ for $Ba_{2-x}Sr_xNiMoO_6$ and $Ba_{2-x}Sr_xMgMoO_6$ successively.

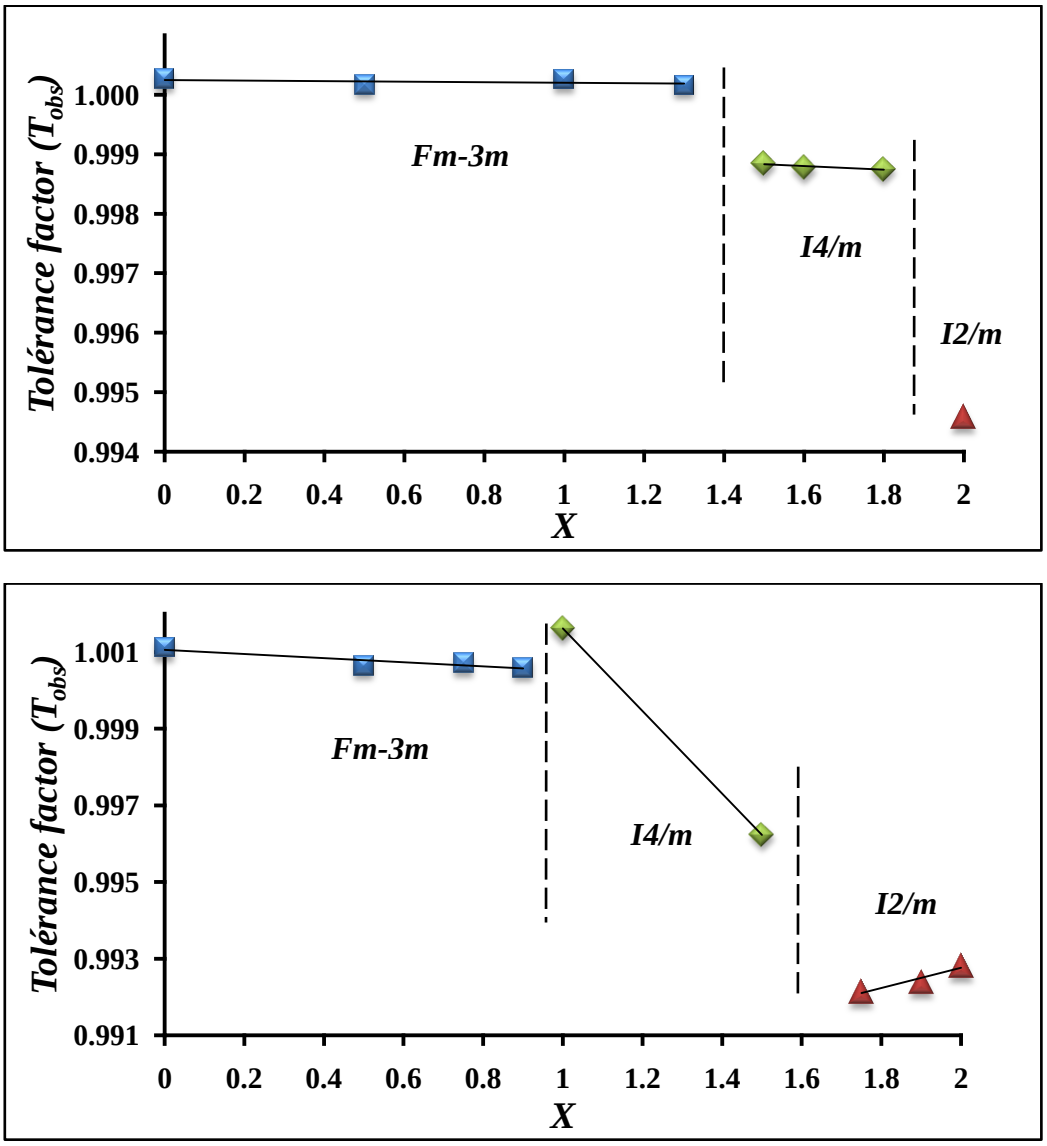

Figure III.6: Observed tolerance factor (obtained from the distances obtained from the Rietveld refinements) as a function of the strontium amount in $Ba_{2-x}Sr_xNiMoO_6$ ($0 \leq x \leq 2$) (up) and $Ba_{2-x}Sr_xMgMoO_6$ ($0 \leq x \leq 2$) (down).

4. Group theory analysis of structural Raman-active modes

4.1 Raman-active modes in $Ba_{2-x}Sr_xMeMoO_6$ $0 \leq x \leq 2$ (Me= Ni, Mg) solid solutions

The irreducible representation obtained for the face-centered cubic Ba_2NiMoO_6 and Ba_2MgMoO_6 perovskite structures (with Fm-3m space group) by analysis of the symmetry group of the site is:

$$\Gamma = A_{1g}\,(R) + E_g\,(R) + 2F_{2g}\,(R) + F_{1g}\,(s) + 4F_{1u}\,(IR) + F_{2u}\,(s) + F_{1u}\,(ac)$$

where the "R", "IR", "ac" and "s" notation stands for :

- R: Raman-active modes,
- IR: infrared active modes,
- ac: acoustic modes,
- s: silent modes.

Among all of these modes predicted by the theory, only A_{1g}, E_g and F_{2g} are Raman-active modes. According to the factor group [26] analysis, nine Raman-active modes, represented as M = 3Ag + 3B*g* + 3E*g*, should be observed for the tetragonal compositions with I*4/m* space group. Only four Raman-active modes should be observed for the cubic compositions. Most of the bands are weak; there are four strong bands for $Ba_{2-x}Sr_xNiMoO_6$ and three strong bands for $Ba_{2-x}Sr_xMgMoO_6$ and they are observed around the wavelengths indicated in the Table III.10.

In Figure III-8 we show the compatibility relations for the space groups present in the known temperature-induced phase-transition sequence: I2/m→I4/m→Fm-3m.

Table III.10: The wavenumber (cm^{-1}) of the strong Raman-active modes for Ba_2/Sr_2NiMoO_6 and Ba_2/Sr_2MgMoO_6.

	$Ba_{2-x}Sr_xNiMoO_6$ ($0 \leq x \leq 2$)		$Ba_{2-x}Sr_xMgMoO_6$ ($0 \leq x \leq 2$)	
Mode number	Ba_2NiMoO_6	Sr_2NiMoO_6	Ba_2MgMoO_6	Sr_2MgMoO_6
1	138	149	125	135
2	442	451	436	446
3	520	580	776	825
4	779	828		

The Raman spectra of $Ba_{2-x}Sr_xNiMoO_6$ ($0 \leq x \leq 2$) and of $Ba_{2-x}Sr_xMgMoO_6$ ($0 \leq x \leq 2$) recorded at ambient conditions are illustrated in Figure III.7.

For all the composition ranges (cubic, tetragonal and monoclinic), the observed Raman modes can be classified into three general families of lattice vibrations:

- Ba^{2+}/Sr^{2+} translations, as well as translational and rotational modes of the MoO_6-octahedra, at frequencies below 200 cm^{-1};
- O–Mo–O bending vibrations, in the 200-500 cm^{-1} region
- Mo–O stretching modes, at frequencies over 500 cm^{-1}.

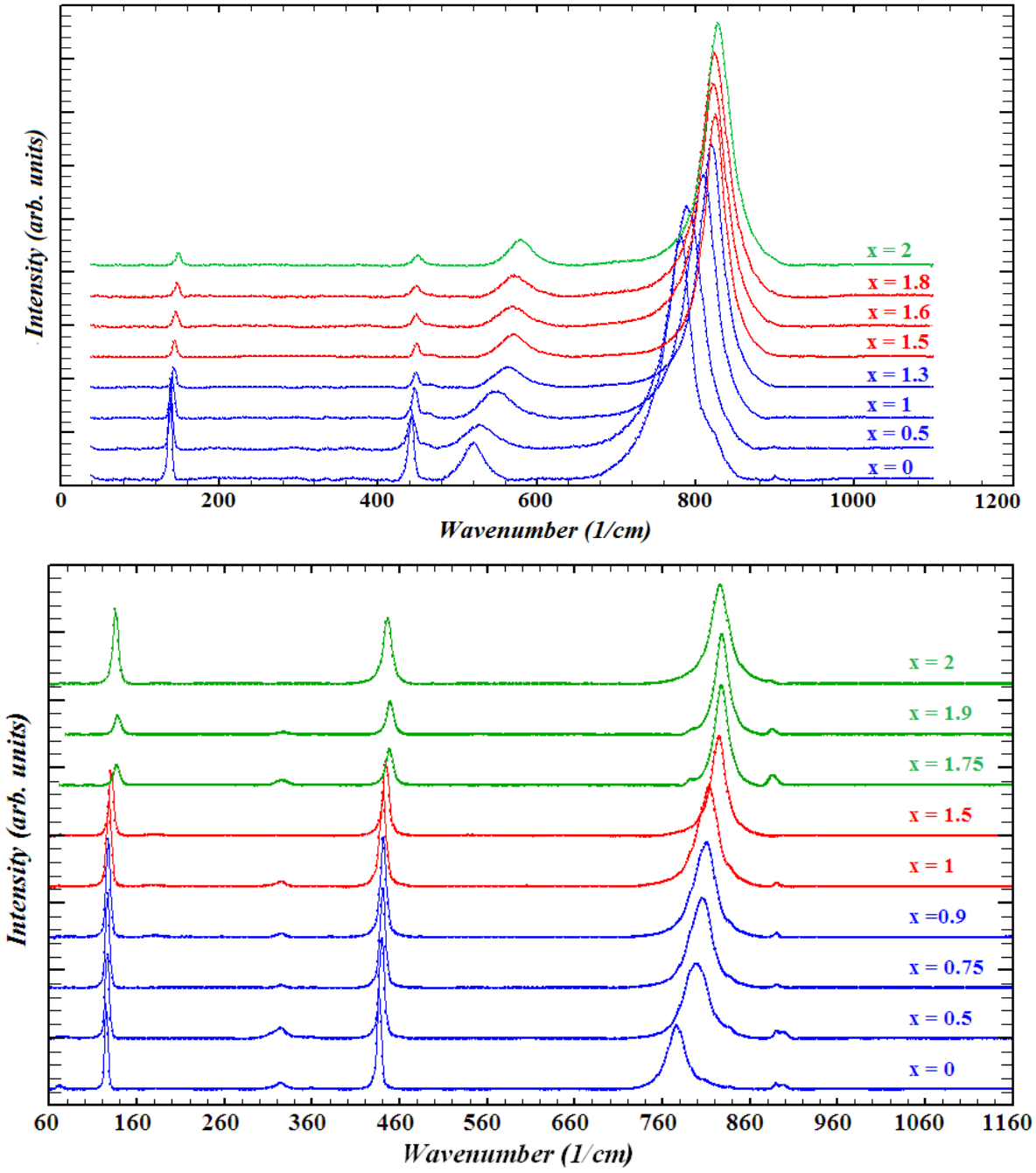

Figure III.7: Raman spectra of $Ba_{2-x}Sr_xNiMoO_6$; $0 \leq x \leq 2$ (up) and $Ba_{2-x}Sr_xMgMoO_6$; $0 \leq x \leq 2$ (down) recorded at ambient conditions.

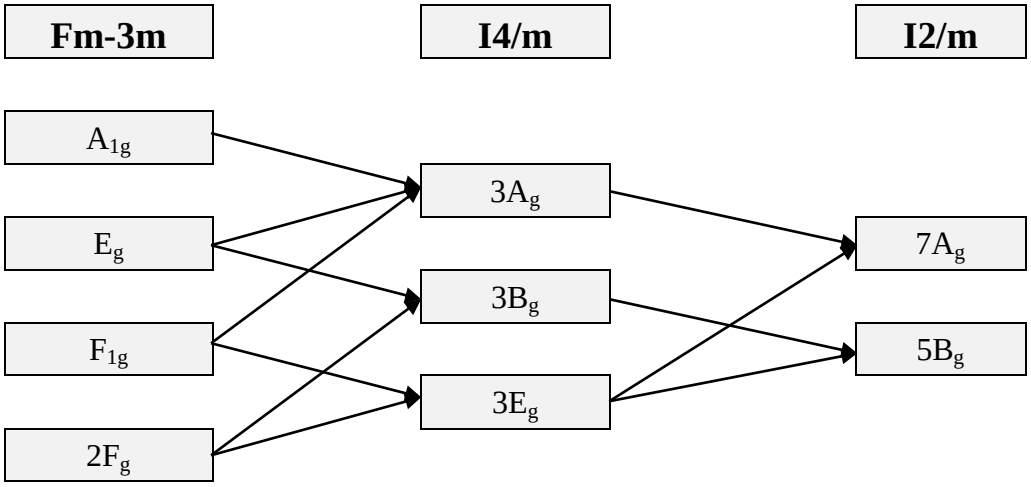

Figure III.8: Correlations diagrams for the Raman-active vibrations in the monoclinic (I2/m), the tetragonal (I4/m) and the cubic (Fm-3m) phases of $Ba_{2-x}Sr_xMeMoO_6$; $0 \leq x \leq 2$ (Me=Ni,Mg).

4.2 Raman spectroscopy analysis at room temperature of $Ba_{2-x}Sr_xMeMoO_6$; $0 \leq x \leq 2$ (Me= Ni, Mg)

The analysis of Raman spectra recorded at room condition of double perovskite compound $Ba_{2-x}Sr_xNiMoO_6$ ($0 \leq x \leq 2$) and $Ba_{2-x}Sr_xMgMoO_6$; ($0 \leq x \leq 2$) shows two phase transitions in this series, from cubic (Fm-3m) to tetragonal (I4/m) and from tetragonal (I4/m) to monoclinic (I2/m). In Figure III.9 and III.10 we plot the Raman modes as a function of the strontium amount in the compositions. While, in Figure III.11 we plot the evolution of the intensity for 800 cm^{-1} mode of $Ba_{2-x}Sr_xNiMoO_6$ as a function of composition and the FWHM for 800 cm^{-1} mode of $Ba_{2-x}Sr_xMgMoO_6$, as a function of the strontium amount in the compositions.

Thus, as shown in these figures, clear changes were observed in the curves showing the cubic to tetragonal phase transition between x = 1.3 and x = 1.5 for the series $Ba_{2-x}Sr_xNiMoO_6$ and between x = 0.9 and x = 1 for the series $Ba_{2-x}Sr_xMgMoO_6$, while the tetragonal to monoclinic phase transition is observed between x = 1.8 and x = 2 and between x = 1.5 and x = 1.75 for the series $Ba_{2-x}Sr_xNiMoO_6$ and $Ba_{2-x}Sr_xMgMoO_6$ successively and thus confirming the Rietveld refinements studies.

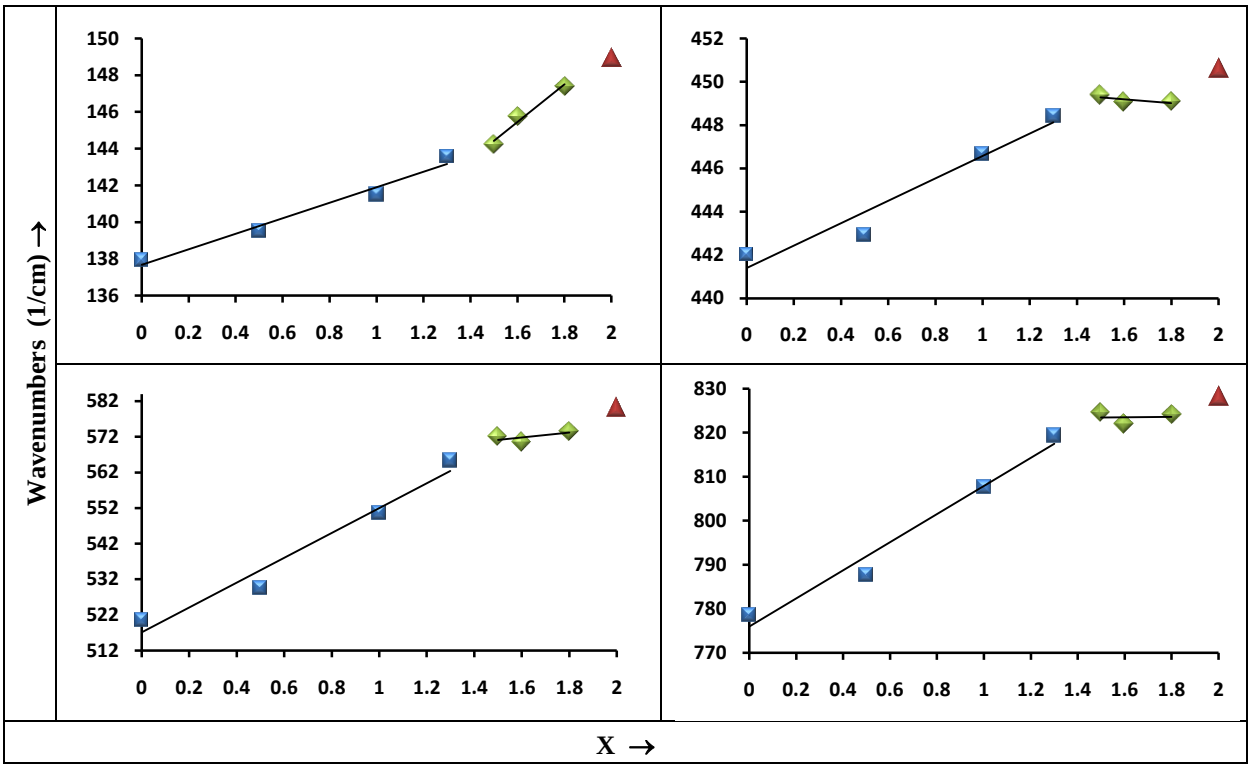

Figure III.9: Evolution of the 140 cm^{-1}, 445 cm^{-1}, 550 cm^{-1} and 800 cm^{-1} Raman mode as a function of the strontium amount in $Ba_{2-x}Sr_xNiMoO_6$ ($0 \leq x \leq 2$) materials.

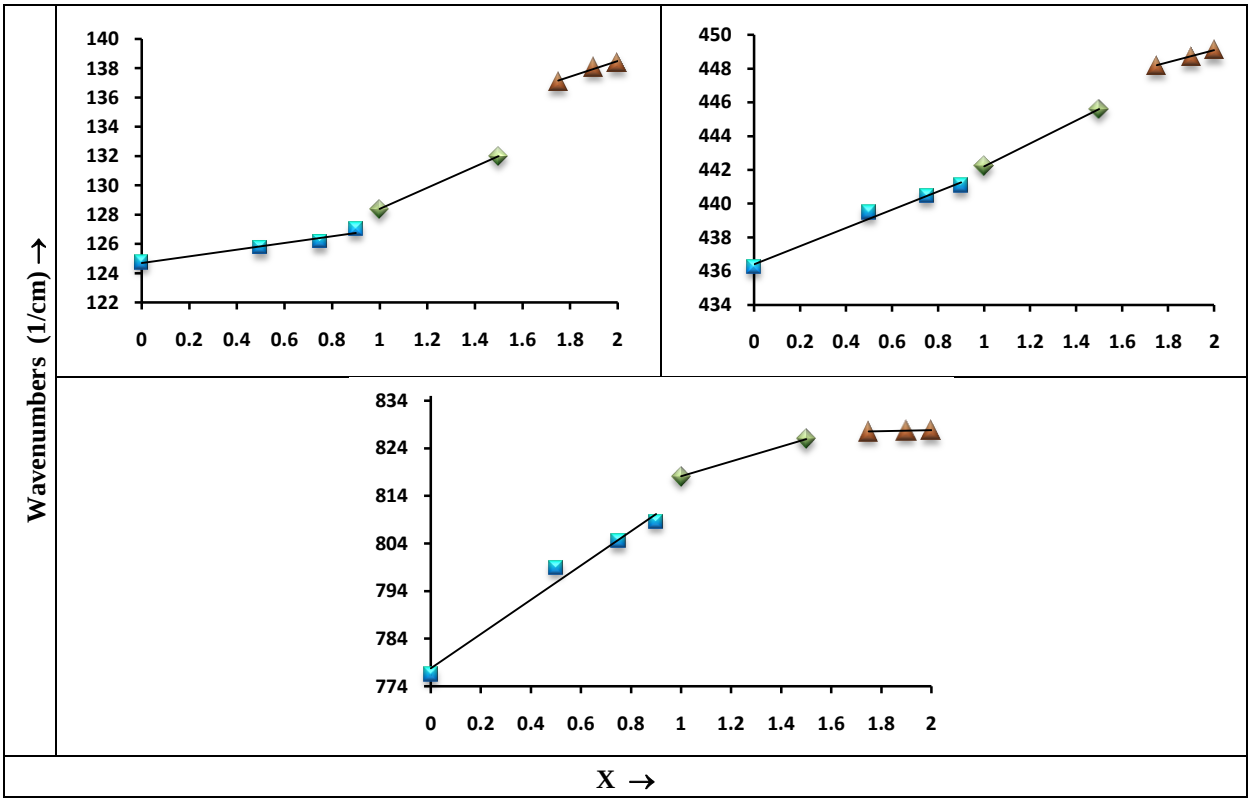

Figure III.10: Evolution of the 130 cm^{-1}, 440 cm^{-1} and 800 cm^{-1} Raman mode as a function of the strontium amount in $Ba_{2-x}Sr_xMgMoO_6$ ($0 \leq x \leq 2$) materials.

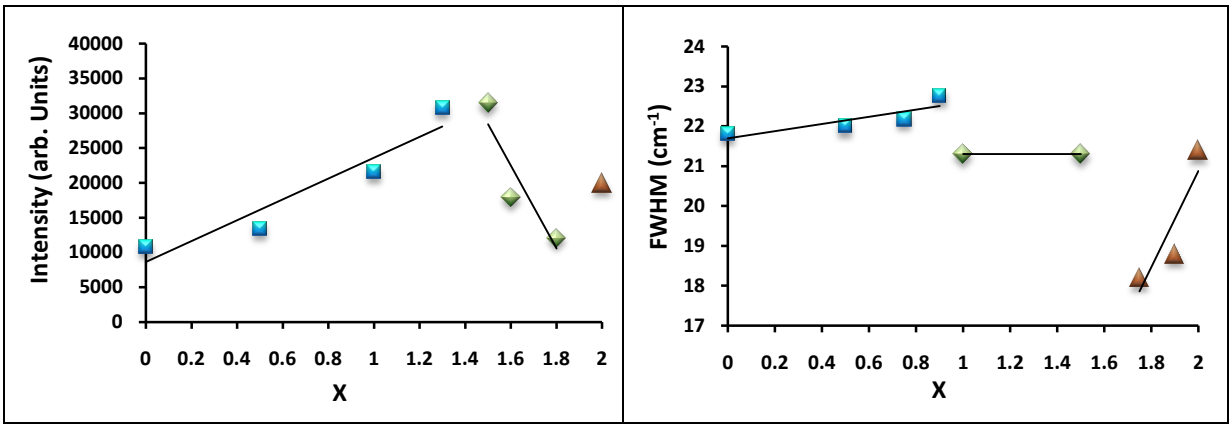

Figure III.11: Evolution of the Intensity and the FWHM for 800cm^{-1} modes of $Ba_{2-x}Sr_xNiMoO_6$ and $Ba_{2-x}Sr_xMgMoO_6$ successively, as a function of the strontium amount in the compositions.

4.3 Temperature study of $Ba_{2-x}Sr_xNiMoO_6$ ($0 \leq x \leq 2$) double perovskites

Raman spectra of $Ba_{2-x}Sr_xNiMoO_6$ ($0 \leq x \leq 2$) were collected in situ at room pressure and elevated temperatures, up to 565°C. The Raman spectra obtained at several temperatures are presented in Figure III.12. In Figure III.13 we illustrate an enlargement of the modes centered at 800 cm^{-1} for different compositions (x=1,5 ; x=1,6 ; x=1,8 and x=2). Clear changes were observed in the curves showing the tetragonal to the cubic phase transition for the compositions of x=1,5 ; x=1,6 and x=1,8 and the monoclinic to the tetragonal and cubic phases transitions for x = 2. The temperature dependence of the modes, the their intensity ratio and their Full Width at Half Maximum (FWHM) were presented in Figure III.14 and Figure III.15.

The strongest temperature changes in wavenumbers we observed are for modes recorded around 445cm^{-1}, 550cm^{-1} and 800cm^{-1}. All lattice modes show a monotonous change in wavenumbers while temperature is increased. The transition from the monoclinic phase to the tetragonal phase, on the one hand, and from the tetragonal phase to the cubic phase on the other hand, shows considerable changes in the temperature dependence of the modes observed around at 445cm^{-1}, 550cm^{-1} and 800cm^{-1}.

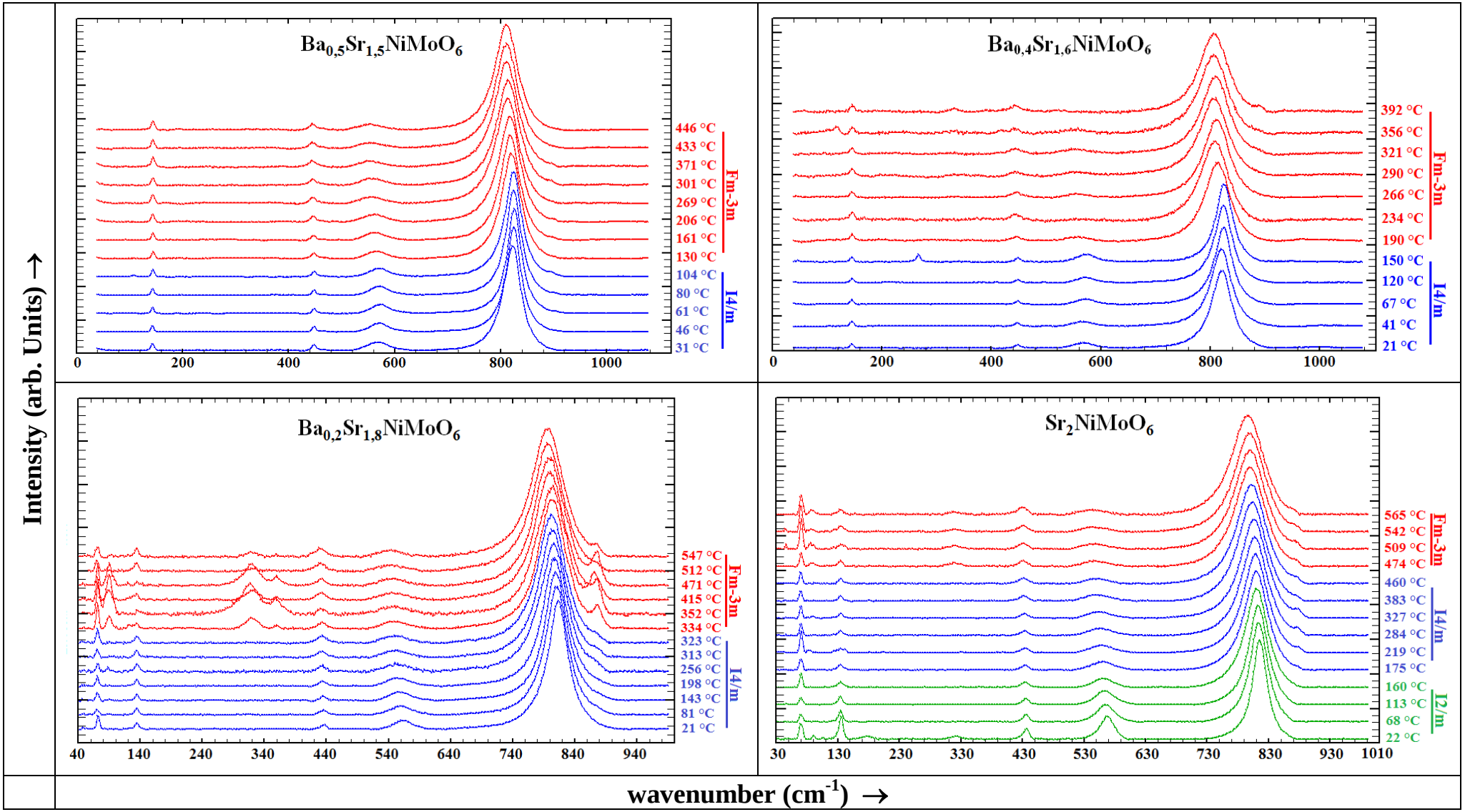

Figure III.12: The Raman spectra of $Ba_{2-x}Sr_xNiMoO_6$ (x=1,5; x=1,6; x=1,8 and x=2) obtained for selected temperatures, as indicated.

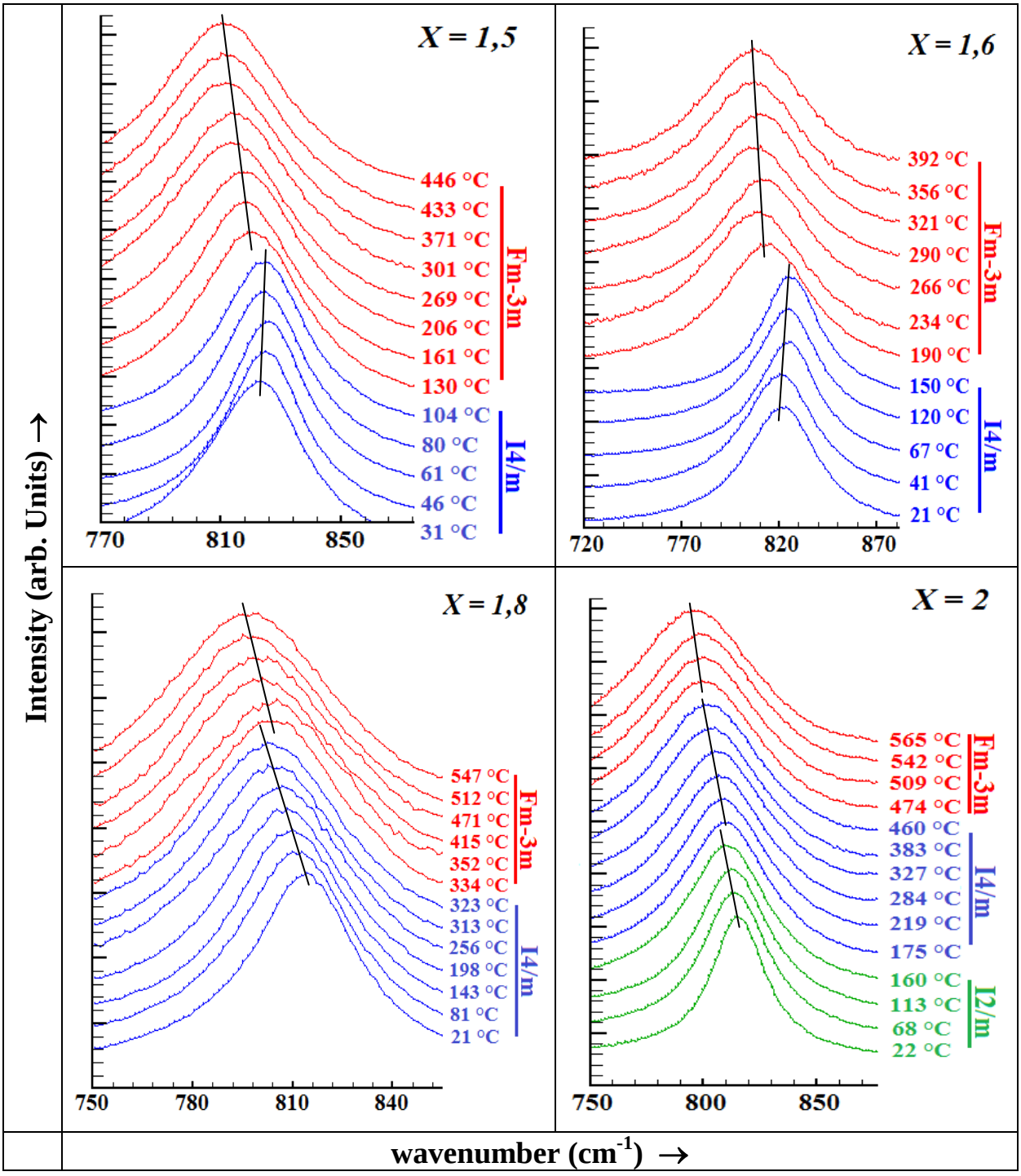

Figure III.13: Enlargement and discontinuous alteration of the slope of the Raman modes centered at 800cm^{-1} illustrating the phase transitions of $Ba_{2-x}Sr_xNiMoO_6$ (x=1,5; x=1,6; x=1,8 and x=2).

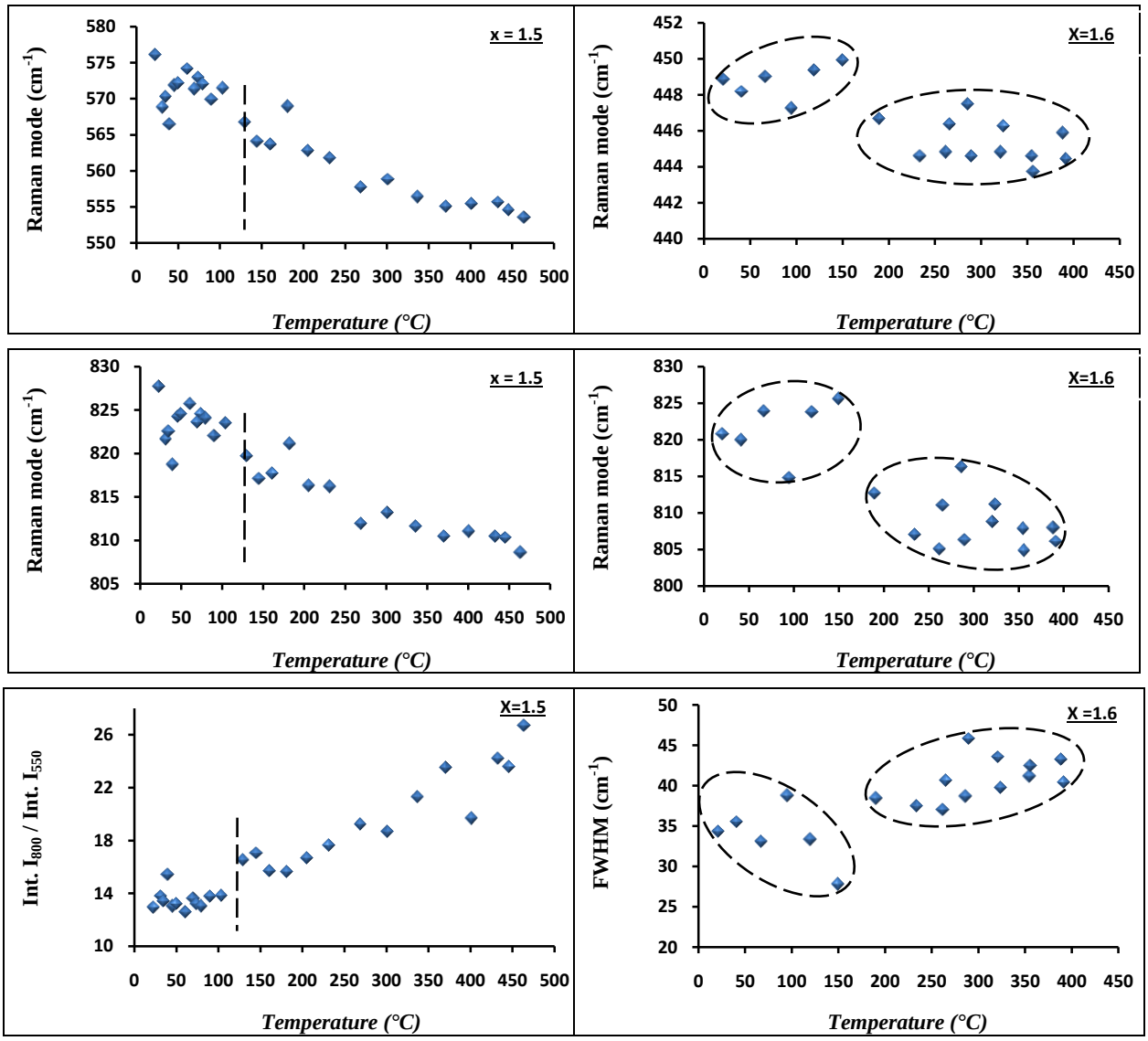

Figure III.14: Raman modes for 550 cm^{-1} and 800 cm^{-1} modes and the intensity ratio I_{800}/I_{550} of $Ba_{0.5}Sr_{1.5}NiMoO_6$ and Raman modes for 445 cm^{-1} and 800 cm^{-1} modes and the FWHM for 800cm^{-1} modes of $Ba_{0.4}Sr_{1.6}NiMoO_6$, as a function of temperature.

For $Ba_{0.5}Sr_{1.5}NiMoO_6$ and $Ba_{0.4}Sr_{1.6}NiMoO_6$ compounds, remarkable changes in the temperature dependence of the modes are observed; the positions of modes centered at 550cm^{-1} and at 800cm^{-1} of $Ba_{0.5}Sr_{1.5}NiMoO_6$ and the positions of modes centered at 445cm^{-1} and at 800cm^{-1} of $Ba_{0.4}Sr_{1.6}NiMoO_6$; The FWHM and the intensity ratio of Raman modes 800cm^{-1} and 550cm^{-1}, show a change in the slope at around 130°C for $Ba_{0.5}Sr_{1.5}NiMoO_6$ and at around 190°C for $Ba_{0.4}Sr_{1.6}NiMoO_6$, indicating the phase transition from the tetragonal (I4/m) to cubic (Fm-3m) structure.

For $Ba_{0.2}Sr_{1.8}NiMoO_6$ compound, remarkable changes in the temperature dependence of the modes are observed; the positions of modes centered at 800cm^{-1} and the FWHM for 550cm^{-1} modes show a change in the slope at around 334°C, indicating the phase transition from the tetragonal (I4/m) to cubic (Fm-3m) structure.

For Sr_2NiMoO_6, When the temperature reached around 175 °C, remarkable changes in the temperature dependence of the modes are observed; the positions of modes centered at 550cm^{-1} and the intensity ratio of Raman modes 800cm^{-1} and 550cm^{-1} show a first change in the slope at around 175°C, indicating the phase transition from the monoclinic (I2/m) to tetragonal (I4/m) structure. A second change in the slopes in the temperature dependence of the modes is noticed at around 474°C, which might be a sign of the second phase transition (I4/m → Fm-3m) in Sr_2NiMoO_6.

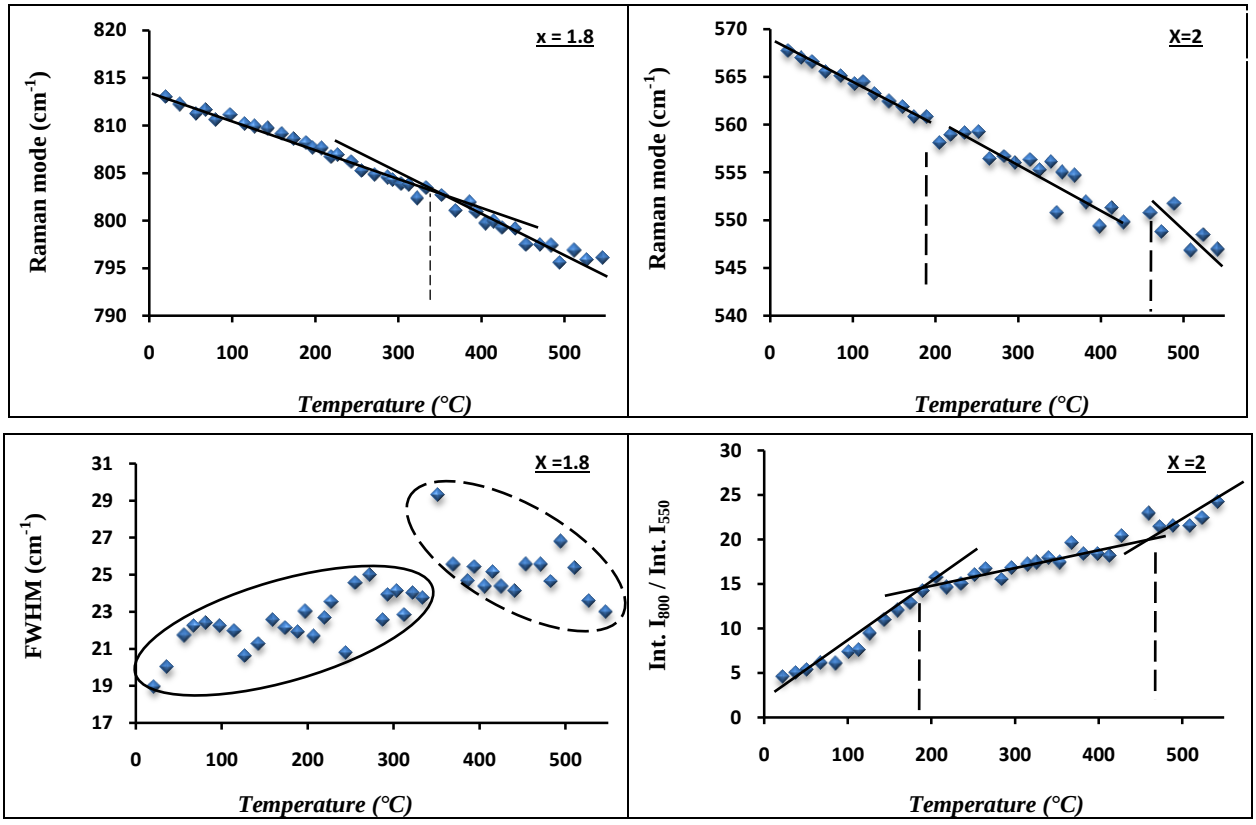

Figure III.15: Raman modes for 800 cm^{-1} and the FWHM for 550cm^{-1} modes of $Ba_{0.2}Sr_{1.8}NiMoO_6$ and Raman modes for 550 cm^{-1} and the intensity ratio I_{800}/I_{550} of Sr_2NiMoO_6, as a function of temperature.

The temperature phase transition as a function of the composition is plotted in Figure III.16. The main difference between the high temperature structure and the low temperature one is the rotation of the NiO_6 and MoO_6 octahedra around the monoclinic and tetragonal axes in the monoclinic and tetragonal phases, respectively. These distortions most likely occur due to the competing bonding preferences of the Ba/Sr and Ni site ions. At high temperatures, both the expanded cell and the greater thermal motion of the atoms, allow those to form a cubic cell. However, on cooling the increased bond strain drives the tetragonal distortion.

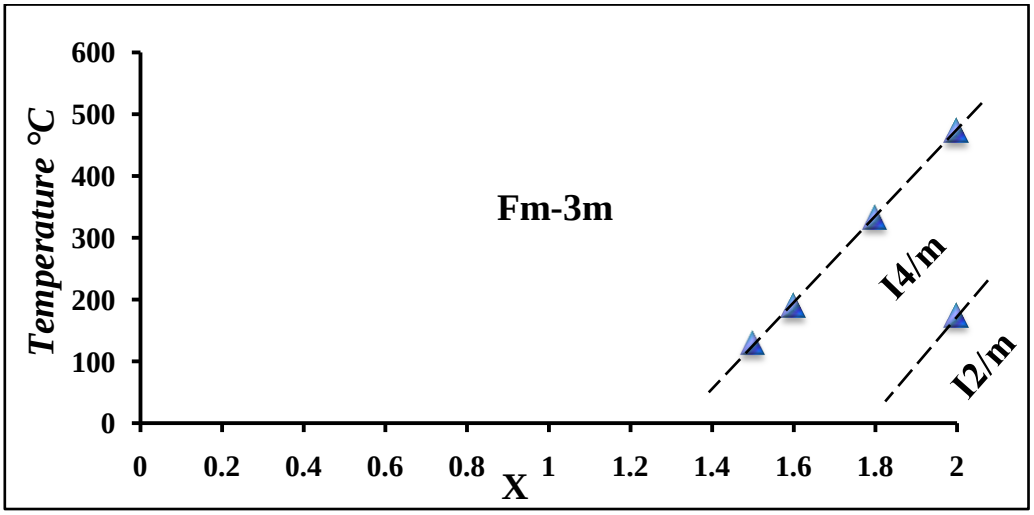

Figure III.16: Transition temperature as a function of the composition of strontium in $Ba_{2-x}Sr_xNiMoO_6$.

4.4 Temperature study of $Ba_{2-x}Sr_xMgMoO_6$ ($0 \leq x \leq 2$) double perovskites

Raman spectra of $Ba_{2-x}Sr_xMgMoO_6$ ($0 \leq x \leq 2$) were collected in situ at room pressure and elevated temperatures, up to 560°C. The Raman spectra obtained at several temperatures are presented in Figure III.17. In Figure III.18 we illustrate an enlargement of the modes centered at 800 cm-1 for the compositions x=1, x=1,5, and x=2, and an enlargement of the modes centered at 440 cm-1 for the composition x=1.75. Clear changes were observed in the curves showing the tetragonal to the cubic phase transition for the compositions of x=1 and x=1, 5 and the monoclinic to the tetragonal and cubic phases transitions for x=1,75 and x=2. The temperature dependence of the modes, the their intensity ratio and their Full Width at Half Maximum (FWHM) were presented in Figure III.19 and Figure III.20.

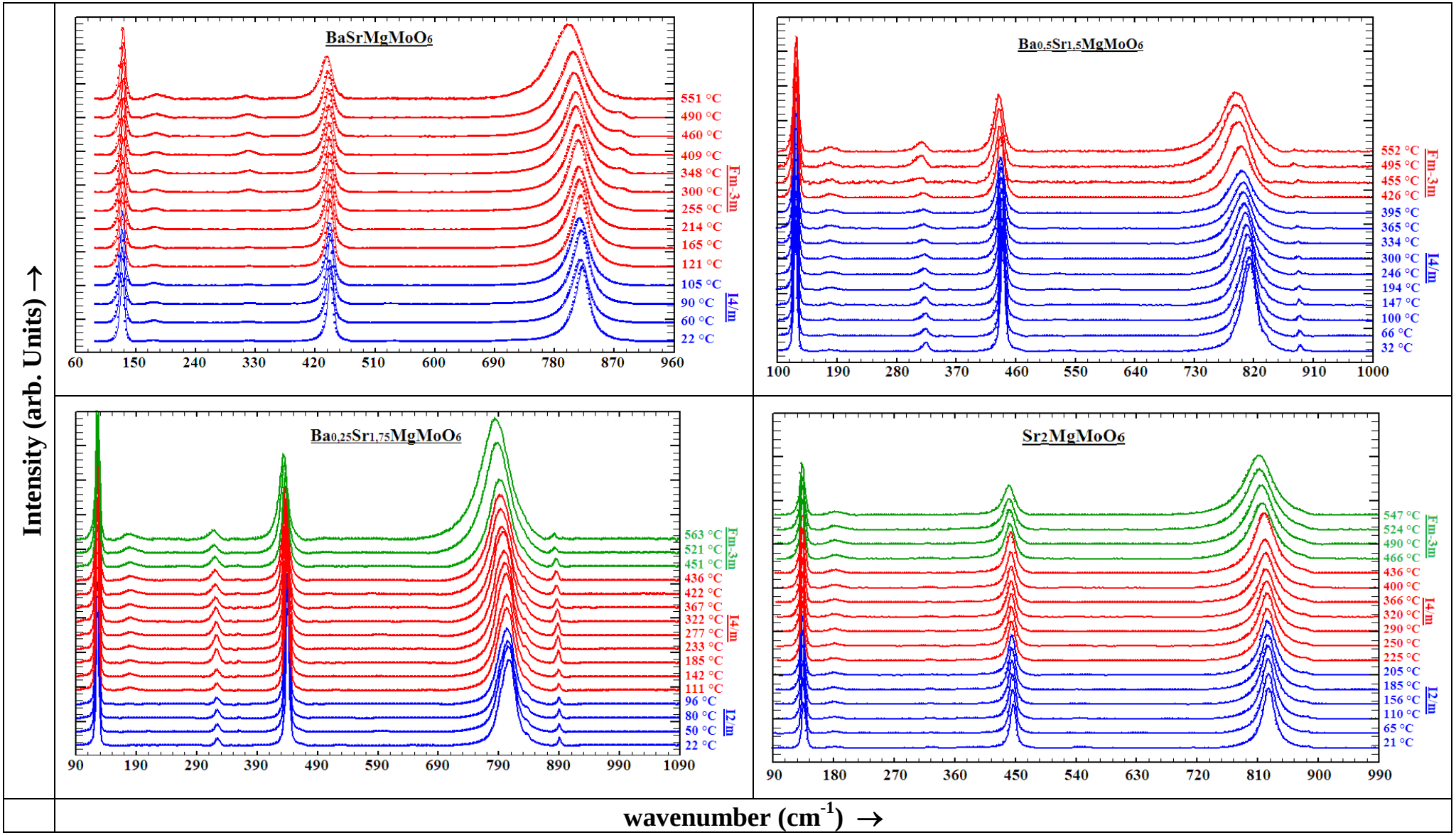

Figure III.17: The Raman spectra of $Ba_{2-x}Sr_xMgMoO_6$ (x=1, x=1,5, x=1,75 and x=2) obtained for selected temperatures, as indicated.

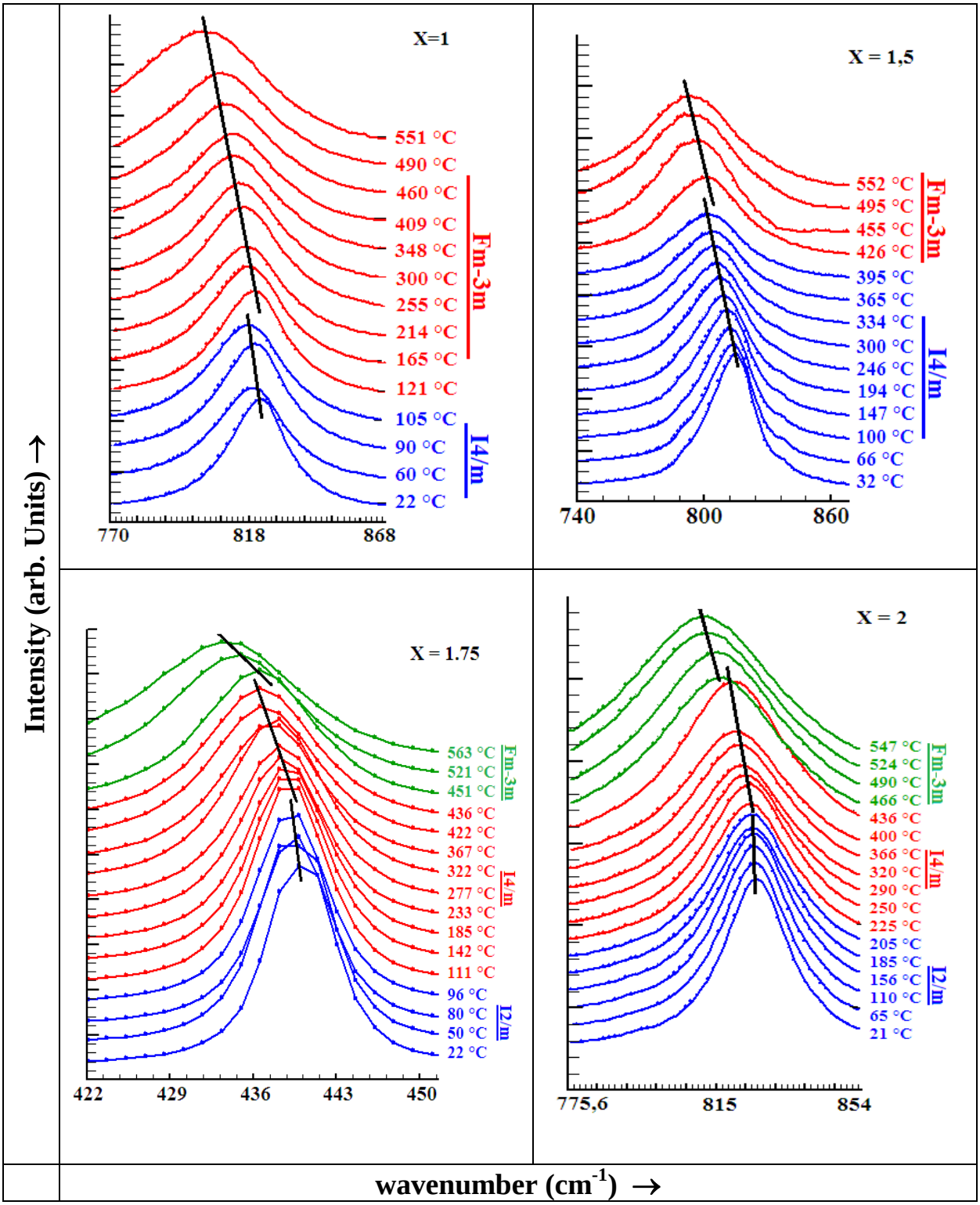

Figure III.18: Enlargement and discontinuous alteration of the slope of the Raman modes centered at 440 cm^{-1} and 800cm^{-1} and illustrating the phase transitions of $Ba_{2-x}Sr_xMgMoO_6$ (x=1, x=1,5, x=1,75 and x=2).

The strongest temperature changes in wavenumbers we observed are for modes recorded around 130cm^{-1}, 440cm^{-1} and 800cm^{-1}. All lattice modes show a monotonous change in wavenumbers while temperature is increased. The transition from the monoclinic phase to the tetragonal phase, on the one hand, and from the tetragonal phase to the cubic phase on the other hand, shows considerable changes in the temperature dependence of the modes observed around at 130cm^{-1}, 440cm^{-1} and 800cm^{-1}.

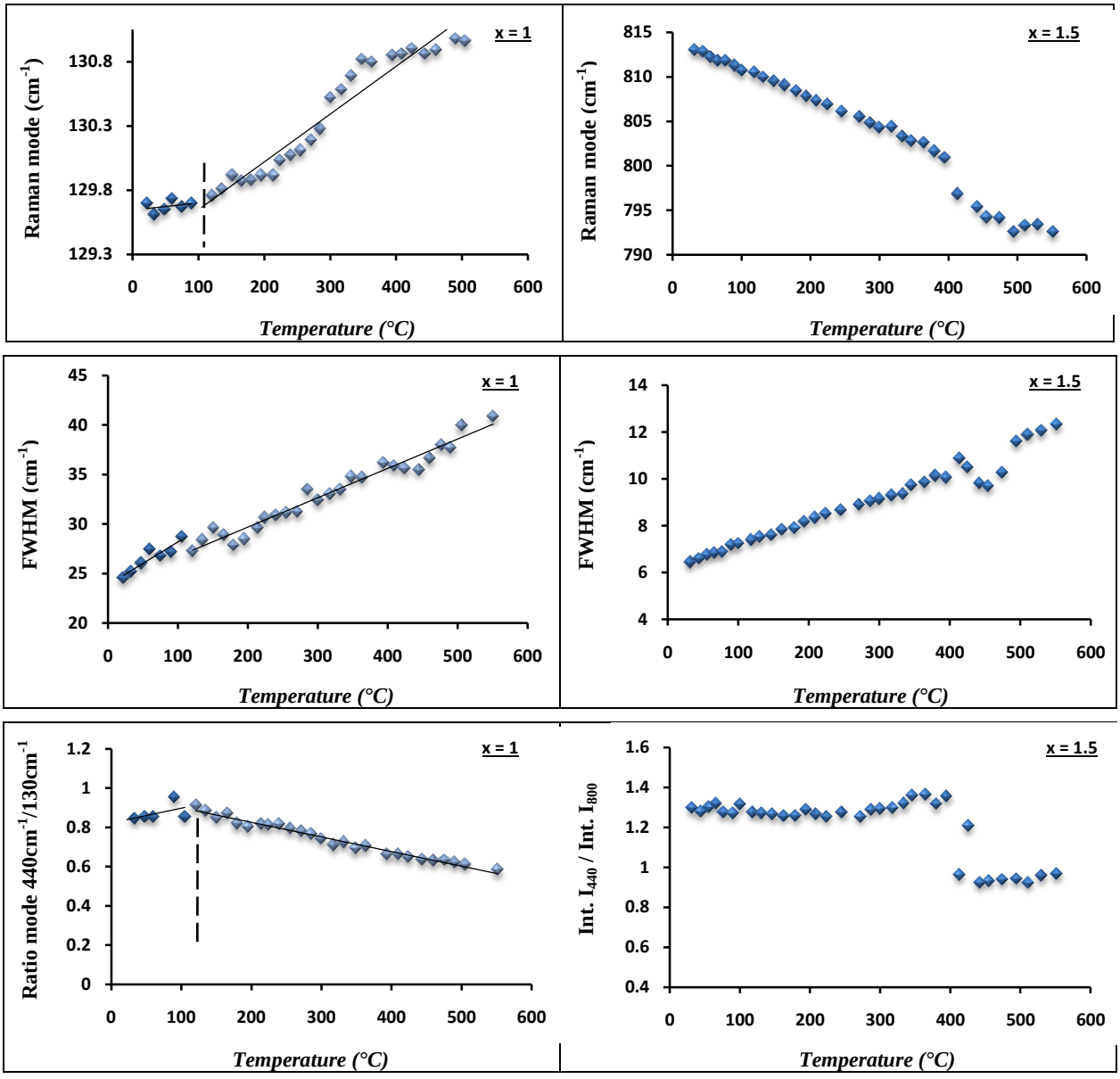

Figure III.19: Raman modes, the mode ratio, the intensity ratio and the FWHM of $Ba_{2-x}Sr_xMgMoO_6$ (x=1 and x=1,5), as a function of temperature.

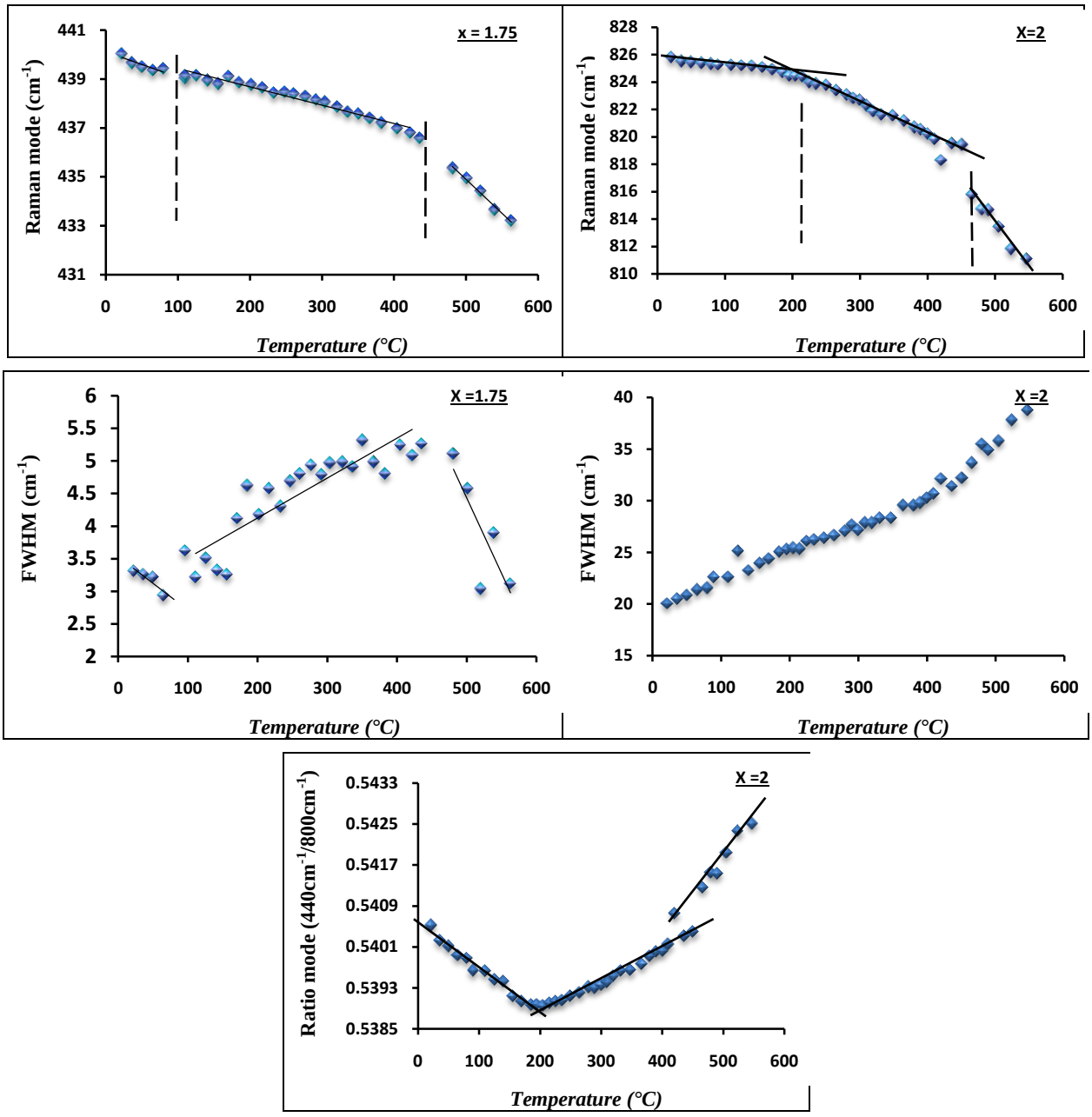

Figure III.20: Raman modes, Ratio Raman mode, and the FWHM of $Ba_{2-X}Sr_XMgMoO_6$ (x=1,75 and x=2), as a function of temperature.

For $BaSrMgMoO_6$ and $Ba_{0.5}Sr_{1.5}MgMoO_6$ compounds, remarkable changes in the temperature dependence of the modes are observed; the positions of modes centered at $130cm^{-1}$ of $BaSrMgMoO_6$ and the positions of modes centered at $800cm^{-1}$ of $Ba_{0.5}Sr_{1.5}MgMoO_6$; The modes ratio, the intensity ratio and the FWHM, show a change in the slope at around 105°C for $BaSrMgMoO_6$ and at around 395°C for $Ba_{0.5}Sr_{1.5}MgMoO_6$, indicating the phase transition from the tetragonal (I4/m) to cubic (Fm-3m) structure.

For $Ba_{0.25}Sr_{1.75}MgMoO_6$ compound, remarkable changes in the temperature dependence of the modes are observed; the positions of modes centered at 440cm^{-1} and the FWHM for 800cm^{-1} modes show a first change in the slope at around 96°C, indicating the phase transition from the monoclinic (I2/m) to tetragonal (I4/m) structure. A second change in the slopes in the temperature dependence of the modes is noticed at around 436°C, which might be a sign of the second phase transition (I4/m → Fm-3m) in $Ba_{0.25}Sr_{1.75}MgMoO_6$.

For Sr_2MgMoO_6, when the temperature reached around 205°C, remarkable changes in the temperature dependence of the modes are observed; the positions of modes centered at 800cm^{-1} and the ratio mode of Raman modes 800cm^{-1} and 440cm^{-1} show a first change in the slope at around 205°C, indicating the phase transition from the monoclinic (I2/m) to tetragonal (I4/m) structure. A second change in the slopes in the temperature dependence of the modes is noticed at around 466°C, which might be a sign of the second phase transition (I4/m → Fm-3m) in Sr_2MgMoO_6.

Figure III.21 shows the temperature phase transition as a function of the composition

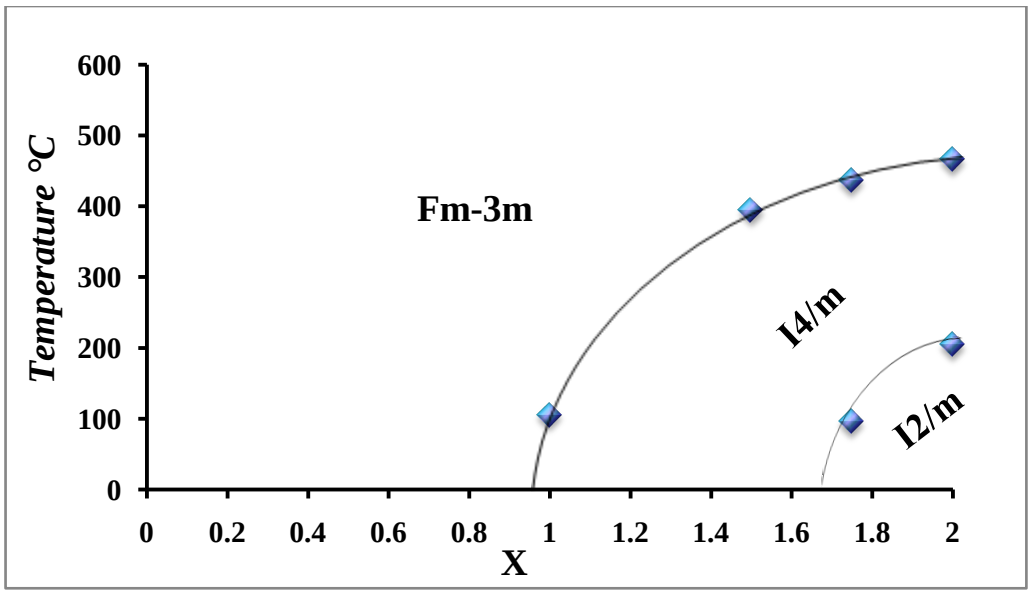

Figure III.21: Transition temperature as a function of the composition of strontium in $Ba_{2-x}Sr_xMgMoO_6$.

5. Conclusion:

In this study, using the X-ray diffraction and Raman spectroscopy techniques, we report on the composition and on the high temperature induced phase transition in $Ba_{2-x}Sr_xMeMoO_6$; $0 \leq x \leq 2$ (Me= Ni, Mg) double perovskite oxides. While increasing strontium amount at room temperature, two phase transition are observed as a function of composition. From cubic to tetragonal phase and from tetragonal to monoclinic phase; both Rietveld refinements and Raman studies showed that the first phase transition occurs between x =1.3 and x = 1.5 for the series $Ba_{2-x}Sr_xNiMoO_6$ and between x =0.9 and x = 1 for the series $Ba_{2-x}Sr_xMgMoO_6$; the second phase transition is observed in the range of $0.9 < x < 1$ for $Ba_{2-x}Sr_xNiMoO_6$ and in the range of $1.5 < x < 1.75$ for $Ba_{2-x}Sr_xMgMoO_6$.

Moreover, increasing the temperature:

- ✓ For the compositions $1,5 \leq x \leq 2$ of the series $Ba_{2-x}Sr_xNiMoO_6$, the tetragonal to cubic phase transition manifests itself for x =1,5, x=1,6 and x=1,8. The tetragonal to cubic phase transition is observed at around 130°C, 190°C and 334°C successively. For x =2, two phase transitions are observed as a function of temperature, the monoclinic-to-tetragonal transition occurs at around 175°C and the tetragonal-to-cubic transition at about 474°C.
- ✓ For the compositions $1 \leq x \leq 2$ of the series $Ba_{2-x}Sr_xMgMoO_6$, the tetragonal to cubic phase transition manifests itself for x =1 and x=1.5. The tetragonal to cubic phase transition is observed at around 105°C and 395°C successively. For the compositions $1,75 \leq x \leq 2$, two phase transitions are observed as a function of temperature, the monoclinic-to-tetragonal transition occurs at about 96°C and around 205°C for x =1,75 and x=2 successively, and the tetragonal-to-cubic transition at about 436°C and around 466°C successively.

For these series, structural symmetry changes are clearly revealed by changes in the compositional and temperature linear dependencies of the modes which exhibit a discontinuous alteration of their slopes upon the transition.

References:

[1] S. Nomura, T. Nakagawa., J. Phys. Soc. Jpn. ; 21 (1966) 1068-1071

[2] B. Manoun, A. Ezzahi, P. Lazor; J. Molec. Str., 1045 (2013) 1–14

[3] Y. Tamraoui, B. Manoun, F. Mirinioui, R. Haloui, P. Lazor. ; J. Alloys Compd. 603 (2014) 86–94

[4] Q. Zhou, B.J. Kennedy, C.J. Howard, M.M. Elcombe, A.J. Studer, Chem. Mater. 17 (2005) 5357

[5] Zhou Q, Kennedy BJ, Elcombe MM. J Solid State Chem ; 180 (2007) 541–548

[6] Mclaughlin AC, de Vries MA, Bos J-WG. Phys Rev B ; 82:94424 (2010).

[7] C.J. Howard, B.J. Kennedy, P.M. Woodward, Acta Crystallogr. B: Struct. Crystallogr. Cryst. Chem. B 59 (2003) 463.

[8] Maria J., Martinez-Lope, José A. Alonso, and Maria T. Casais - Eur. ; J. Inorg. Chem. (2003) 2839-2844.

[9]Q. Zhang, T. Wei, Y.H. Huang ; J. Power Sources 198 (2012) 59.

[10] L. Zhang, Q. Zhou, Q. He, T. He ; J. Power Sources 195 (2010) 6356.

[11] A.K. Eriksson, S.-G. Eriksson, S.A. Ivanov, C.S. Knee, J. Eriksen, H. Rundlöf, M. Tseggai ; Mater. Res. Bull. ; 41 (2006) 144–157

[12] L. Brixner ; J. Phys. Chem. 64 (1960) 165

[13] M. F. Kupriyanov and E. G. Fesenko ; Kristallogr 7 (1962) 451

[14] A. K. Eriksson, S. -G. Eriksson, S. A. Ivanov, C. S. Knee & H. Rundlöf; Ferroelectrics, 339:1 (2006), 235-243 (DOI: 10.1080/00150190600740317)

[15] A.K. Eriksson, S.G. Eriksson, S.A. Ivanov, C.S. Knee, J. Eriksen, H. Rundlöf, M. Tseggai, Mater. Res. Bull. 41 (2006) 144–157

[16] Michael W Lufaso, René B Macquart, Yongjae Lee, Thomas Vogt, Hans-Conrad zur Loye. J. Phys. Condens. Matter 18 (2006) 8761–8780

[17] A. Prasatkhetragarn, S. Kaowphong, R. Yimnirun. Appl. Phys. A 107:1 (2012) 17–121

[18] Shoichiro Nomura1, Takehiko Nakagawa1. J. Phys. Soc. Jpn. 21(1966) 1068-1071

[19] S.A. Ivanov, S.G. Eriksson, R. Tellgren, H. Rundlöf, M. Tseggai, Mater. Res. Bull. 40 (2005) 840

[20] Shaoan Zhang, Yihua Hu, Li Chen, Xiaojuan Wang, Guifang Ju, and Yan Fan; J. Mater. Res.; 28:22 (2013) 3130-3136

[21] Yasutake Teraoka, Ming-Deng Wei and Shuichi Kagawa, J. Mater. Chem.; 8:11 (1998) 2323–2325. (DOI: 10.1039/A806442C).

[22] Y. Tamraoui, B. Manoun, F. Mirinioui, R. Haloui, P. Lazor. Journal of Alloys and Compounds 603 (2014) 86–94

[23] B. Manoun, Y. Tamraoui, P. Lazor, W. Yang, Applied Physics Letters 103, 261908 (2013)

[24] A.M.Glazer, Acta Cryst. A 31 (1975) 756.

[25] A.M. Glazer, Acta Crystallogr. B 28 (1972) 3384.

[26] E. Kroumova, M.I.Aroyo, J.M.Perez-Mato, A.Kirov, C.Capillas, S.Ivantchev, H. Wondratschek, Phase Transit.76(2003)155.

Chapter IV

Synthesis, structural phase transitions induced by chemical composition in $Ba_{2-x}Sr_xCdWO_6$ ($0 \leq x \leq 2$) double perovskite, X-Ray diffraction and Raman spectroscopy study

In this chapter we will present the results obtained in this study concerning the solid solutions $Ba_{2-x}Sr_xCdWO_6$; ($0 \leq x \leq 2$).

First, we will present the results of analyzes carried out as well as the characterisation of different solid solutions synthesized by X-ray diffraction technique.

In a second step, we will also present a description of the crystallographic behavior of the phases as a function of the strontium composition.

Thirdly, we will present the results concerning the Raman spectroscopy analysis at ambient temperature of the different solid solutions, as well as the effect of the strontium composition on the crystallographic behavior of these solutions.

Finally, we will conclude this chapter with an analysis and a discussion of the results obtained.

1. Introduction :

The Perovskites crystals represent a large family of compounds, which have been extensively studied so far due to their interesting properties and applications.

For simple perovskites of the general formula ABO_3 (Space group Fm-3m, N°.225), their structure is cubic with the B cations (located at the centers of the oxygen octahedra) are six-fold coordinated. These octahedra form the backbone of the crystal structure of the ordinary perovskites; the A cations are located in the voids in between the oxygen octahedra. While for the double perovskites $A_2BB'O_6$, their structure can be not only cubic, but tetragonal, orthorhombic and monoclinic [1].

A variety of crystalline structures is obtained following the addition of the second cation B', which is due to a main possibility of occupation of different sites. The A^{2+} cations are 12-fold coordinated, where as the B^{2+} and B'^{6+} are 6-fold coordinated. The structure of these doubles perovskites can be thought of as a sequence of alternating BO_6 and $B'O_6$ octahedra [2], with the A^{2+} cations located between these octahedra. If the ionic size of the A^{2+} cation is small to fit the 12-fold coordinated position, the BO_6 and $B'O_6$ octahedra can tilt indifferent ways, leading to lower symmetry of the crystal structure.

Recently the research on double perovskites has been particularly renewed after the discovery of metallic and ferromagnetic characteristics in Sr_2FeMoO_6 and Sr_2FeReO_6 by Kobayashi et al. [3,4] and especially the room temperature colossal magneto-resistance (CMR) discovery in Sr_2FeMoO_6 [5,6].

The modification of structural and magnetic properties by changing the A, B and/or B'-site cations in double perovskites of type $A_2BB'O_6$ has also gained interest in order to better understand the mechanism of colossal magneto resistance and other unusual physical and chemical properties.

The stability of double perovskite materials with $A_2BB'O_6$ or $AA'BB'O_6$ stochiometry are shown to depend on how the B and B' cations are distributed over the octahedral sites, degree of cation inversion as well as on the size and electronic structure of transition metal cations B and B' [7].

Theoretically, when the tolerance factor is t = 1, perovskite adopts a cubic symmetry. For t>1 or t<1, the structure is deformed, which gives a symmetry lower than the cubic symmetry.

It has been shown that the dielectric properties of the materials depend strongly on the degree of ordering and on the ionic size which determine the symmetry of the structure [8]. Colla et al. [9] and Reaney et al. [10] have shown that temperature stability in Ba and Sr based complex perovskites is fundamentally related to the onset and degree of octahedral tilting. Therefore, understanding the complex relationships between composition, structure, and properties in perovskites remains a significant challenge in materials chemistry.

To contribute to the studies undertaken in the field of phase transitions in this type of compounds, we have undertaken the synthesis by solid state method of a series of oxides $Ba_{2-x}Sr_xCdWO_6$ ($0 \leq x \leq 2$) that we studied by the X-ray diffraction and Raman spectroscopy.

We report in this chapter:

- a detailed study of the crystal structure of new solid solutions $Ba_{2-x}Sr_xCdWO_6$ ($0 \leq x \leq 2$).
- the effect of Sr substitution in site A on phase transitions induced by the composition in $Ba_{2-x}Sr_xCdWO_6$ ($0 \leq x \leq 2$).
- a contribution to the search for structural phase transitions in materials based on metal oxides having a double-perovskite structure.
- the A-cation-size effect on the possible appearance of phase transitions in $Ba_{2-x}Sr_xCdWO_6$ ($0 \leq x \leq 2$) double perovskite oxides.

2. Previous work on A_2CdWO_6 (A=Ba, Sr) double perovskites

Recently, various studies have been performed on Ba_2MWO_6 [11,12] (M= Mg, Ni, Zn) which are all formed in a cubic Fm-3m space group with a ≈ 8,3Å and Sr_2MWO_6 [13,14] (M = Ni, Zn, Co, Cu) materials. The Sr_2CdWO_6 is synthesized by solid state reaction and its crystal structure was determined by high-resolution X-ray diffraction [15], this compound has a monoclinic structure (space group $P2_1/n$) with lattice parameters, a=5,7463 Å, b=5,8189 Å, c=8,1465 Å, β=90,071°.

3. Description of the structure

The X-ray powder diffraction patterns of $Ba_{2-x}Sr_xCdWO_6$ ($0 \leq x \leq 2$) in the 15–100° 2Θ range are showed in Figure IV.1. Indexing of X-ray powder diffraction patterns for these compositions was performed by means of the computer program Dicvol [16]. The first 15 peak positions, with a maximal absolute error of 0.03°(2θ), were used as input data.

We can already notice that the peaks positions shift to higher 2θ degree when increasing the value of x, which means the cell volume decreases with increasing x, this is due to the substitution of Ba^{2+} by Sr^{2+} whose ionic rays are 1.61Å and 1.44Å successively. The X-ray diffraction patterns were assigned to :

- A cubic symmetry with the space group Fm-3m for the composition range ($0 \leq x \leq 0.6$).
- A tetragonal symmetry with the space group I4/m for the composition range ($0.8 \leq x \leq 1$).
- A monoclinic symmetry with the space group I2/m for the compositions range ($1.2 \leq x \leq 1.6$)
- A monoclinic symmetry with the space group $P2_1/n$ for the compositions range ($1.8 \leq x \leq 2$)

Given that, according to the X-ray diffraction analysis, the samples show a small amount of impurities in the form of $Ba/SrWO_4$ and CdO. In order to reduce the impact of the intensities associated with these impurities on the values of the reliability factors, we took into account their crystalline structures throughout the refinement of the powder XRD pattern of this series. $Ba/SrWO_4$ crystallizes in a tetragonal lattice, with space group $I4_1/a$ at room temperature [17] and the unit cell parameters are: a = b = 5.5568 Å and c = 12.504869. While the CdO crystallizes in a cubic lattice, with space group Fm-3m [18] and the unit cell parameters are a = b = c = 4.6973 Å.

The lattice parameters that were refined using the complete powder diffraction data sets are listed in Table IV.1. The variation of the unit cell parameters of the cubic, tetragonal and monoclinic phases in the studied composition range in $Ba_{2-x}Sr_xCdWO_6$ ($0 \leq x \leq 2$) is shown in Figure IV.2. While Figure IV.3 show the evolution of the volume of the cell with increasing strontium concentration.

The considerable changes in the trend of evolution of the lattice parameters correspond to the cubic–tetragonal, tetragonal–monoclinic I2/m and monoclinic (I2/m)–monoclinic ($P2_1/n$) phase transitions. The cubic to tetragonal transition is observed between x=0.6 and x=0.8, the

tetragonal to monoclinic (I2/m) transition is observed between x=1 and x=1.2, while the monoclinic (I2/m) to monoclinic ($P2_1/n$) transition is observed between x=1.6 and x=1,8.

However, the volume of the cell displayed an approximately linear reduction as the Sr content was increased in the series $Ba_{2-x}Sr_xCdWO_6$, which is due to the chemical substitution of Ba^{2+} by relatively smaller Sr^{2+} ions. As a consequence the volume of the octahedral space decreases which reflects the decrease of the lattice parameters.

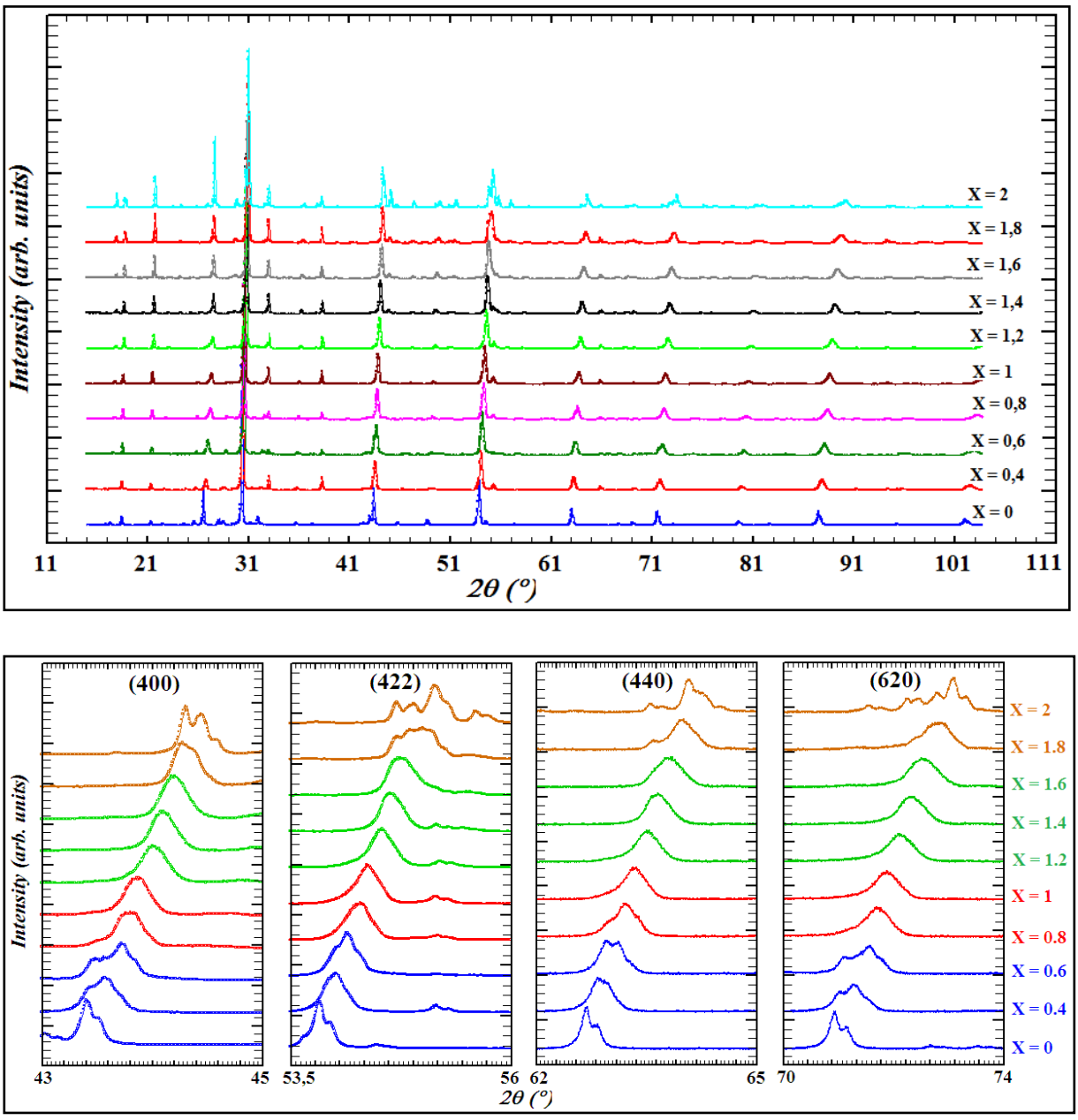

Figure IV.1: X-ray powder diffraction patterns for $Ba_{2-x}Sr_xCdWO_6$ ($0 \leq x \leq 2$). The Enlarged sections show the evolution of the basic (400), (422), (440) and (620) reflections.

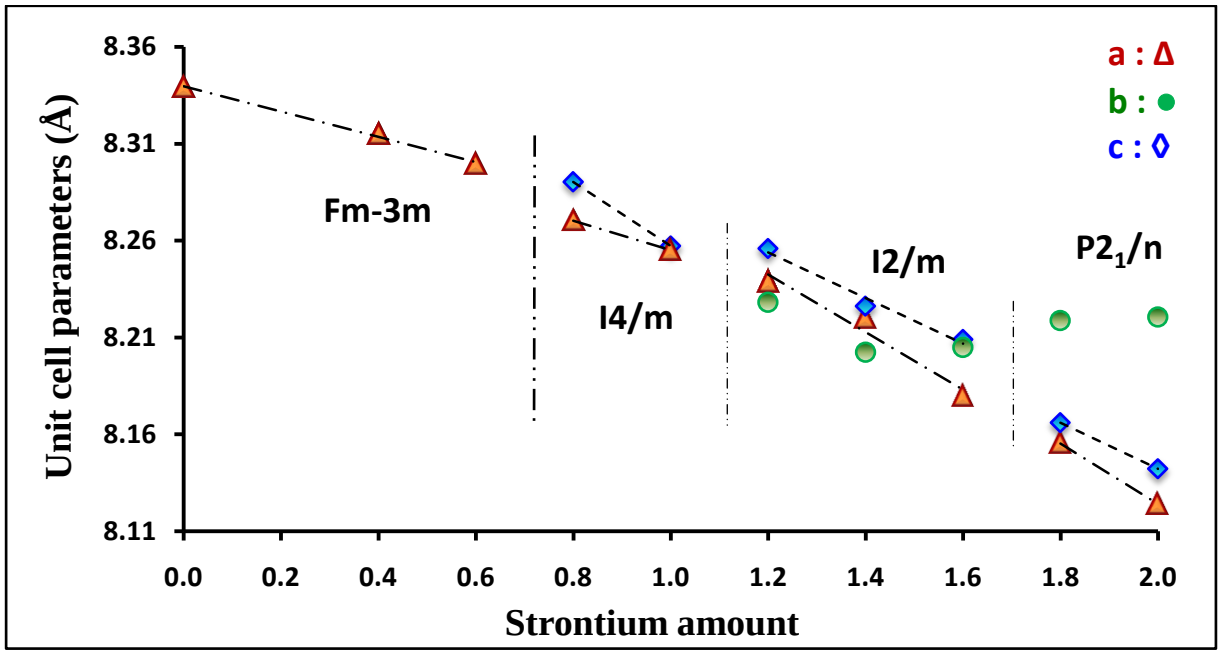

Figure IV.2: Variation of the lattice parameters as a function of composition for the series $Ba_{2-x}Sr_xCdWO_6$. The *a* and *b* values in the tetragonal and monoclinic cells have been multiplied by $2^{1/2}$ for clarity. The cubic to tetragonal transition is observed between x=0.6 and x=0.8, the tetragonal to monoclinic I2/m transition is observed between x=1 and x=1.2, while the monoclinic I2/m to monoclinic $P2_1/n$ is observed between x=1.6 and x=1.8.

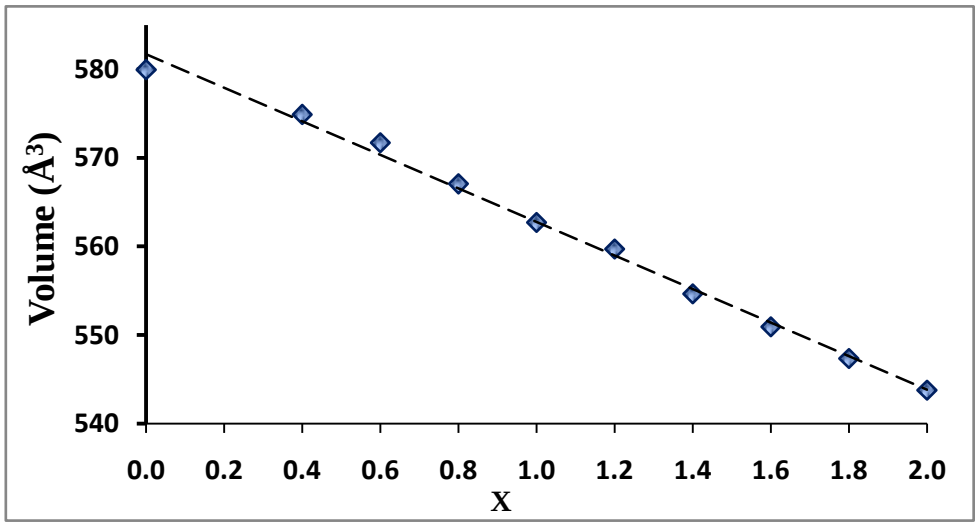

Figure IV.3: Variation of the volume of the cell with increasing strontium concentration in the studied composition range in $Ba_{2-x}Sr_xCdWO_6$ ($0 \leq x \leq 2$).

Note that, in Figure IV.2 and Figure IV.3, the “a” and "b" parameters values in the tetragonal and monoclinic cells have been multiplied by $2^{1/2}$ for clarity.

Table IV.1: Unit cell parameters of $Ba_{2-x}Sr_xCdWO_6$ ($0 \leq x \leq 2$).

x	a(Å)	b(Å)	c(Å)	β(°)	V(Å^3)	Symmetry
0	8.3393(1)				579.950	Cubic Fm-3m
0,4	8.3150(2)				574.890(21)	
0,6	8.2991(3)				571.595(36)	
0,8	5.8480(3)		8.2904(8)		283.527(36)	Tetragonal I4/m
1	5.8372(5)		8.2573(14)		281.349(60)	
1,2	5.8259(6)	5.8183(6)	8.2560(4)	90.1978(52)	279.846(44)	Monoclinic I2/m
1,4	5.8125(5)	5.7999(7)	8.2262(8)	89.923(21)	277.323(49)	
1,6	5.7838(5)	5.8017(4)	8.2090(6)	89.7758(64)	275.459(35)	
1,8	5.7667(2)	5.8116(2)	8.1660(2)	90.1415(27)	273.670(13)	Monoclinic $P2_1/n$
2	5.7447(1)	5.8128(1)	8.1422(2)	90.0790(21)	271.890(11)	

Three types of symmetry with four space group are used for the refinement of the powder XRD pattern for $Ba_{2-x}Sr_xCdWO_6$. Firstly, the space group Fm-3m in a cubic lattice for the compositions of $0 \leq x \leq 0.6$ with starting model taken from Ref. [19]. In this model Ba^{2+}/Sr^{2+}, Cd^{2+} and W^{6+} are placed at 8c(1/4, 1/4, 1/4), 4a(0,0,0) and 4b(1/2, 1/2,1/2) sites respectively; the oxygen atoms occupy 24e(x,0,0) sites.

Secondly, the space group I4/m in a tetragonal lattice for the compositions of $0.8 \leq x \leq 1$ with starting model taken from Ref. [20]. In this model Ba^{2+}/Sr^{2+}, Cd^{2+} and W^{6+} are placed 4d(0, 1/2, 1/4), 2a(0, 0, 0) and 2b(0, 0, 1/2) sites, respectively. The oxygen atoms occupy 4e(0, 0, z) and 8h(x, y, 0) positions.

Thirdly, the space group I2/m in a monoclinic lattice for the compositions of $1.2 \leq x \leq 1.6$ with starting model taken from Ref. [21]. In this model Ba^{2+}/Sr^{2+}, Cd^{2+} and W^{6+} are placed 4i(x, 1/2, z), 2c(1/2, 0, 0) and 2b(0, 1/2, 0) sites, respectively. The oxygen atoms occupy 4i(x, 0, z) and 8j(x, y, z) positions.

At last, the space group $P2_1/n$ in a monoclinic lattice for the compositions of $1.8 \leq x \leq 2$ with starting model taken from Ref. [22,23]. In this model, Ba^{2+}/Sr^{2+}, Cd^{2+} and W^{6+} are placed at 4e(x, y, z), 2c(0, 1/2, 0) and 2d(1/2, 0, 0) sites, respectively; the oxygen atoms occupy 4e(x, y, z) positions. Figure IV.4 shows the typical Rietveld refinement patterns along with the difference plot at ambient temperature for $Ba_{2-x}Sr_xCdWO_6$ ($0 \leq x \leq 2$).

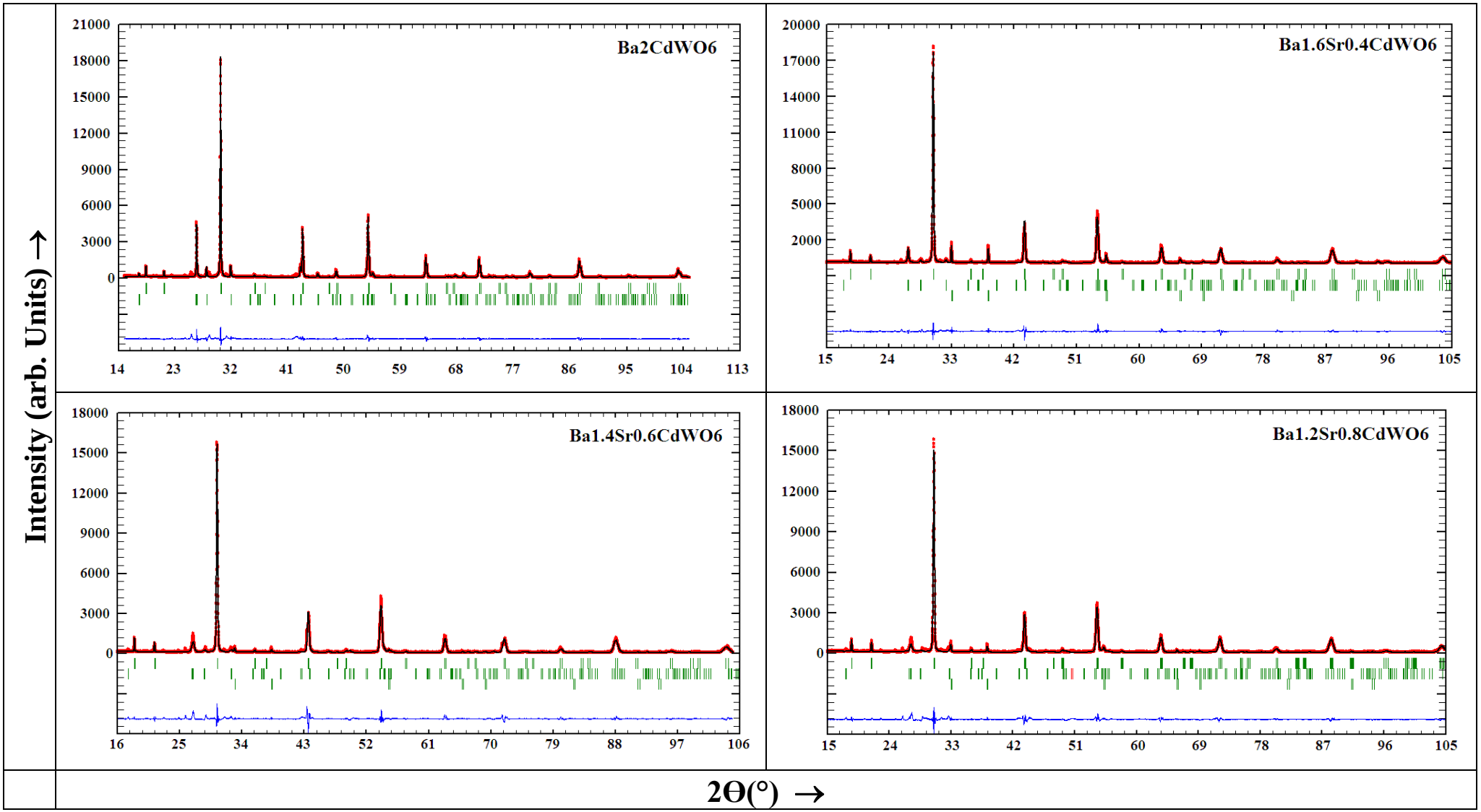

Figure IV.4: Final Rietveld plots for compounds $Ba_{2-x}Sr_xCdWO_6$. The upper symbols illustrate the observed data (circles) and the calculated pattern (solid line). The vertical markers show calculated positions of Bragg reflections. The lower curve is the difference diagram. (1/3)

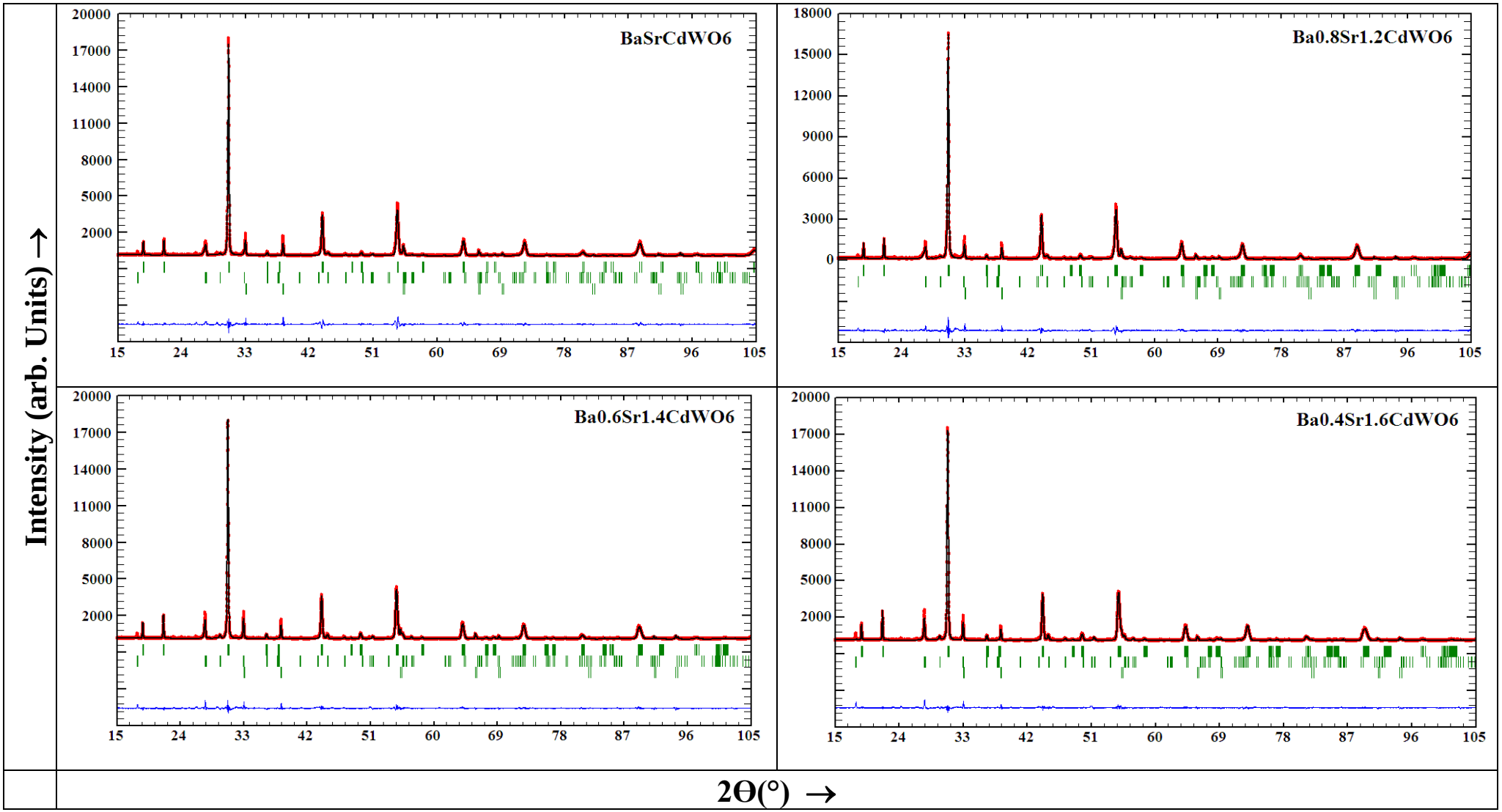

Figure IV.4: Final Rietveld plots for compounds $Ba_{2-x}Sr_xCdWO_6$. The upper symbols illustrate the observed data (circles) and the calculated pattern (solid line). The vertical markers show calculated positions of Bragg reflections. The lower curve is the difference diagram. (2/3)

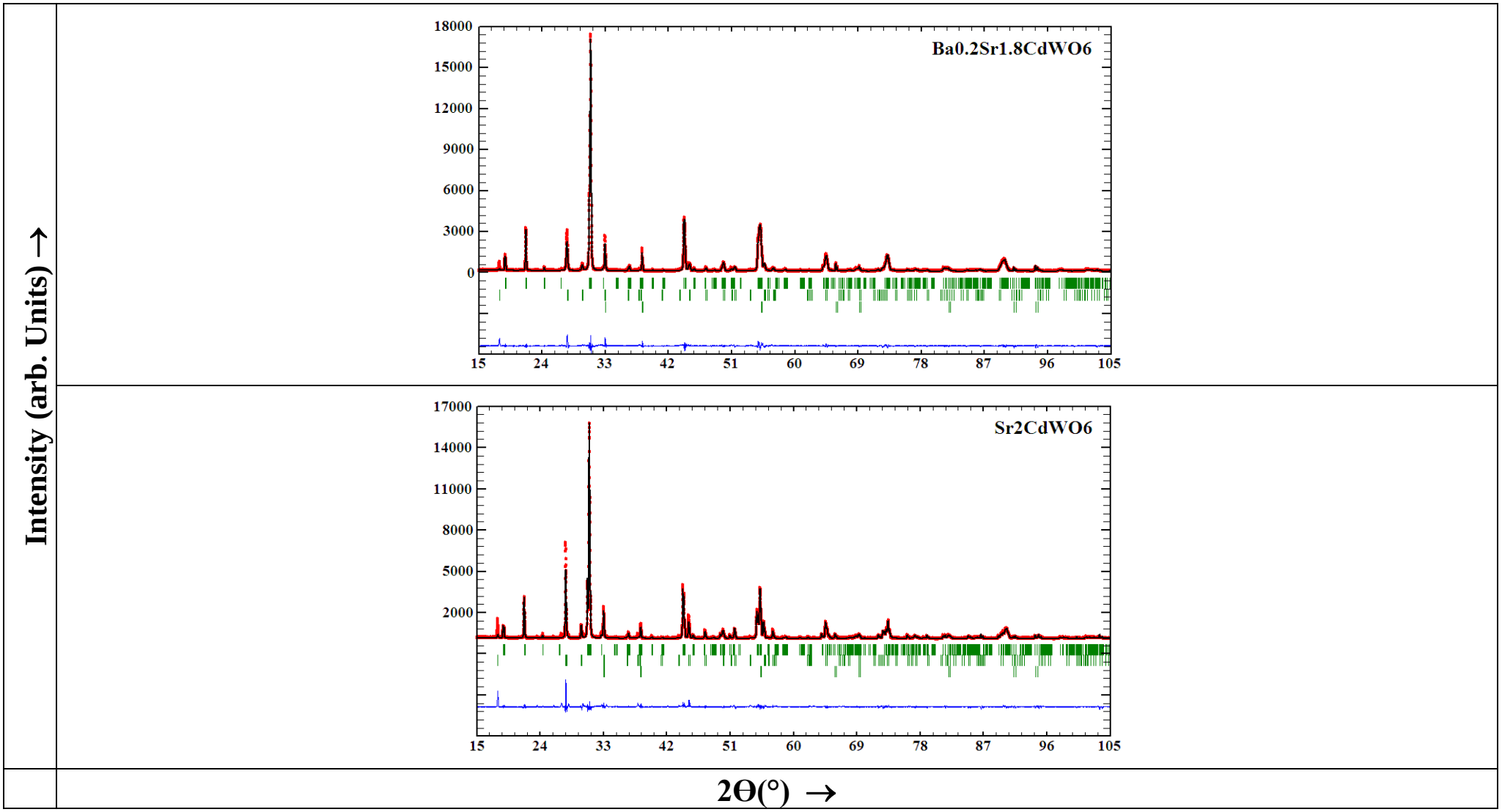

Figure IV.4: Final Rietveld plots for compounds $Ba_{2-x}Sr_xCdWO_6$. The upper symbols illustrate the observed data (circles) and the calculated pattern (solid line). The vertical markers show calculated positions of Bragg reflections. The lower curve is the difference diagram. (3/3)

x	**x = 0**	**x = 0,4**	**x = 0,6**	**x = 0,8**	**x = 1**
Zero point (°2θ)	0.0484(18)	0.0197(14)	0.0484(23)	0.0409(23)	-0.0038(14)
Pseudo-Voigt function PV = η L + (1 − η) G	η= 0.724(10)	η=0.4565(57)	η=0.3823(74)	η=0.4045(80)	η=0.4659(59)
Caglioti parameters	U= 0.0579(48) V= -0.0024(46) W= 0.0056(9)	U=0.2960(96) V=0.0048(77) W=0.0003(14)	U=0.407(16) V= 0.0093(23) W=-0.0016(22)	U=0.3699(71) V=-0.0197(33) W=0.0064(24)	U=0.3393(25) V=0.0047(98) W=0.0034(18)
No. of reflections	66/2	70/2	70/2	210/2	210/2
N°. of refined parameter	28	34	31	35	35
Space group	***Fm-3m***	***Fm-3m***	***Fm-3m***	***I4/m***	***I4/m***
a (Å) **c (Å)** **V ($Å^3$)**	8.3393(1) 579.950(13)	8.3150(2) 574.890(21)	8.2991(3) 571.595(36)	5.8480(3) 8.2904(8) 283.527(36)	5.8372(5) 8.2573(14) 281.349(60)
Z	4	4	4	4	4
Atom number	4	5	5	5	5
R_F **R_B** **R_p** **R_{wp}** **cR_p** **cR_{wp}**	0.0518 0.0343 0.0978 0.146 0.156 0.199	0.0266 0.0276 0.0902 0.125 0.142 0.170	0.0314 0.0379 0.123 0.0172 0.201 0.240	0.0311 0.0341 0.118 0.170 0.198 0.241	0.0206 0.0239 0.0930 0.130 0.151 0.181
Wavelength (Å): λkα1 = 1.5406, **2θ range (°)**: 15-105, **Step scan increment (°2θ)** : 0.010142, **Program**: FULLPROF					

Table IV.3: Details of Rietveld refinement conditions of the monoclinic (I2/m and $P2_1/n$) compositions in $Ba_{2-x}Sr_xCdWO_6$ ($1.2 \leq x \leq 2$).

X	**X = 1,2**	**X = 1,4**	**X = 1,6**	**X = 1,8**	**X = 2**
Zero point (°2θ)	0.0668(15)	0.0239(13)	0.0201(14)	0.0294(11)	0.0009(11)
Pseudo-Voigt function PV = η L + (1 − η) G	η=0.7409(55)	η=0.5180(3)	η=0.4489(87)	η=0.5449(90)	η=0.6014(19)
Caglioti parameters	U=0.1793(32) V=-0.00002(36) W=0.00333(48)	U=0.2139(52) V= -0.0046(77) W=0.0042(14)	U=0.2117(27) V=-0.0073(85) W=0.0062(15)	U=0.0945(83) V=0.0075(60) W=0.0025(10)	U=0.0329(38) V=0.0029(33) W=0.0035(6)
No. of reflections	411/2	410/2	410/2	704/2	656/2
No. of refined parameter	41	39	41	46	47
Space group	**I2/m**	**I2/m**	**I2/m**	**$P2_1/n$**	**$P2_1/n$**
a (Å)	5.8259(6)	5.8125(5)	5.7838(5)	5.7667(2)	5.7447(1)
b (Å)	5.8183(6)	5.7999(7)	5.8017(4)	5.8116(2)	5.8128(1)
c (Å)	8.2560(4)	8.2262(8)	8.2090(6)	8.1660(2)	8.1422(2)
β(°)	90.1978(52)	89.9230(8)	89.7758(64)	90.1415(27)	90.0790(21)
V (Å3)	279.846(44)	277.323(49)	275.459(35)	273.670(13)	271.890(11)
Z	4	4	4	4	4
Atom number	5	5	5	5	4
R_F	0.0292	0.0281	0.0232	0.0345	0.0519
R_B	0.0267	0.0311	0.0167	0.0263	0.0360
R_p	0.0887	0.0809	0.0744	0.0762	0.0875
R_{wp}	0.123	0.120	0.114	0.110	0.135
cR_p	0.151	0.138	0.124	0.122	0.144
cR_{wp}	0.178	0.172	0.162	0.153	0.191
Wavelength (Å): λkα1 = 1.5406**, 2θ range (°):** 15-105**, Step scan increment (°2θ) :** 0.010142**, Program:** FULLPROF					

For all the compositions, the details of the Rietveld refinement conditions were classified in Table IV.2 (for $0 \leq x \leq 1$) and Table IV.3 (for $1.2 \leq x \leq 2$).

The structural details at room temperature, the refined position coordinates, isotropic displacement parameters and sites occupancy of $Ba_{2-x}Sr_xCdWO_6$ ($0 \leq x \leq 2$) series in the cubic and the tetragonal compositions, are given in Table IV.4 and for the monoclinic compositions I2/m and $P2_1/n$ in Table IV.5.

The analysis of refined crystallographic parameters for the cubic compositions in $Ba_{2-x}Sr_xCdWO_6$ ($0 \leq x \leq 0.6$) indicates that the ions Cd^{2+} and W^{6+} are octahedrally coordinated with the oxygen atoms. These octahedra are alternatively connected and extended in three dimensions.

The oxygen atoms connect the CdO_6 and WO_6 octahedra along the three directions. The typical Cd–O–W angle for all compounds is constrained to 180° by Fm-3m space group and oxygen position coordinates (x, 0, 0), indicating no tilt with respect to a, b and c-axes, and corresponds to the a°a°a° in Glazer's notation [24,25]. A [0 0 1] projection of the $Ba_{1,4}Sr_{0,6}CdWO_6$ unit cell indicating the typical polyhedral arrangement is shown in Figure IV.5-(a).

For the tetragonal compounds with I4/m as space group in $Ba_{2-x}Sr_xCdWO_6$ ($0.8 \leq x \leq 1$), the analysis of refinement crystallographic illustrates that Cd^{2+} and W^{6+} are octahedrally coordinated with the oxygen atoms. The CdO_6 and WO_6-octahedra are alternatively connected and extended in three dimensions. The O(1) atoms connect CdO_6 and WO_6-octahedra along the c-axis. In ab-plane CdO_6 and WO_6 octahedra are connected through the O(2) atoms. The appreciable tilt of the octahedra is observed for the Cd–O(2)–W bond angle (around 159.2°) (for $Ba_{1,2}Sr_{0,8}CdWO_6$ as an example). In this case, the tilt pattern of the octahedral units satisfies the $a^0a^0c^-$ tilt system in Glazer's notation [24, 25]. A [0 0 1] projection of the $Ba_{1,2}Sr_{0,8}CdWO_6$ unit cell indicating the typical polyhedral arrangement and the tilt pattern is shown in Figure IV.5-(b).

While for the monoclinic compounds with I2/m as space group in $Ba_{2-x}Sr_xCdWO_6$ ($1.2 \leq x \leq 1.6$), the CdO_6 and WO_6 octahedra are alternatively connected and extended in three dimensions. The O(1) atoms connect the CdO_6 and WO_6 octahedra along the c-axis and O(2) atoms connect them along the a and b axes.

Table IV.4: Positional and thermal parameters of the cubic and tetragonal compositions in $Ba_{2-x}Sr_xCdWO_6$ ($0 \leq x \leq 1$) after Rietveld refinement from XRD data collected at room temperature.

System	X	Atom	x	y	z	B(Å^2)	Occ.
Fm-3m	x = 0	W	0,5	0,5	0,5	0.260(56)	1
		Cd	0	0	0	0.521(81)	1
		Ba	0,25	0,25	0,25	0.798(53)	2
		O1	0.2722(11)	0	0	1.477(54)	6
	x = 0.4	W	0,5	0,5	0,5	0.062(35)	1
		Cd	0	0	0	0.004(0)	1
		Ba/Sr	0,25	0,25	0,25	0.706(29)	1,6/0,4
		O1	0.2760(80)	0	0	1.928(91)	6
	x = 0.6	W	0,5	0,5	0,5	0.064(48)	1
		Cd	0	0	0	0.464(67)	1
		Ba/Sr	0,25	0,25	0,25	0.797(45)	1,4/0,6
		O1	0.2777(11)	0	0	3.363(01)	6
I4/m	x = 0.8	W	0	0	0,5	0.133(87)	1
		Cd	0	0	0	-0.017(95)	1
		Ba/Sr	0	0,5	0,25	0.563(46)	1,2/0,8
		O1	0	0	0.2923(38)	-2.393(04)	2
		O2	0.3174(51)	0.2257(41)	0	0.874(51)	4
	x = 1	W	0	0	0,5	0.733(02)	1
		Cd	0	0	0	-0.081(86)	1
		Ba/Sr	0	0,5	0,25	0.842(35)	1/1
		O1	0	0	0.2977(43)	2.412(99)	2
		O2	0.3221(30)	0.2204(25)	0	-3.564(70)	4

Table IV.5: Positional and thermal parameters of the monoclinic compositions in $Ba_{2-x}Sr_xCdWO_6$ ($1.2 \leq x \leq 2$) after Rietveld refinement from XRD data collected at room temperature.

System	X	Atom	x	y	z	B(Å^2)	Occ.
I2/m	x = 1.2	**W**	0	0,5	0	0.560(03)	1
		Cd	0,5	0	0	0.097(32)	1
		Ba	0.5045(18)	0,5	0.2536(17)	1.043(49)	0,8/1,2
		O1	0.5736(59)	0	0.2896(39)	1.164(99)	2
		O2	0.2196(40)	0.2587(56)	0.0404(19)	0.239(41)	4
	x = 1.4	**W**	0	0,5	0	0.295(60)	1
		Cd	0,5	0	0	0.597(96)	1
		Ba/Sr	0.5021(27)	0,5	0.2582(25)	1.372(53)	0,6/1,4
		O1	0.6105(48)	0	0.2868(40)	-0.508(99)	2
		O2	0.2339(50)	0.2779(61)	0.0345(20)	-0.926(56)	4
	x = 1.6	**W**	0	0,5	0	0.480(67)	1
		Cd	0,5	0	0	0.123(80)	1
		Ba/Sr	0.4935(19)	0,5	0.2479(92)	1.375(41)	0,4/1,6
		O1	0.5984(50)	0	0.2780(47)	1.622(62)	2
		O2	0.2269(32)	0.2824(44)	0.0410(21)	0.022(04)	4
$P2_1/n$	x = 1.8	**W**	0,5	0	0	0.317(40)	1
		Cd	0	0,5	0	0.360(56)	1
		Ba/Sr	0.5090(9)	0.5320(3)	0.2478(7)	0.767(37)	0,2/1,8
		O1	0.2356(36)	0.1855(30)	0.0024(27)	0.202(13)	2
		O2	0.3042(35)	0.7425(32)	-0.0534(24)	0.202(13)	2
		O3	0.4089(32)	-0.0109(20)	0.2187(27)	-0.233(59)	2
	x= 2	**W**	0,5	0	0	0.276(51)	1
		Cd	0	0,5	0	0.288(71)	1
		Sr	0.5100(23)	0.5382(3)	0.2502(7)	0.576(49)	2
		O1	0.2485(40)	0.1864(36)	-0.0135(38)	0.703(01)	2
		O2	0.3104(39)	0.7441(37)	-0.0536(26)	-0.802(43)	2
		O3	0.4166(32)	0.0061(26)	0.2262(30)	0.983(36)	2

The tilt of the octahedra is observed from the Cd–O(1)–W bond angle (144.5°) and from the Cd–O(2)–W bond angle (164.1°) (for $Ba_{0,6}Sr_{1,4}CdWO_6$ as an example). The tilt pattern of the octahedral units satisfies the $a^0b^-b^-$ tilt system in Glazer's notation [24, 25]. A [1 1 0] projection of the $Ba_{0,6}Sr_{1,4}CdWO_6$ unit cell indicating the typical polyhedral arrangement and the tilt pattern is shown in Figure IV.5-(c).

Lastly, for the monoclinic compositions with $P2_1/n$ as space group in $Ba_{2-x}Sr_xCdWO_6$ ($1.8 \leq x \leq 2$), the O(1) and O(2) atoms connect the CdO_6 and WO_6 octahedra along the a and b axes and the O(3) atoms connect them along the c-axis. The tilt of the octahedra is observed from the Cd–O(1)–W bond angle (163.8°), from the Cd–O(2)–W bond angle (151.4°) and from the Cd–O(3)–W bond angle (153.3°) (for Sr_2CdWO_6 as an example).

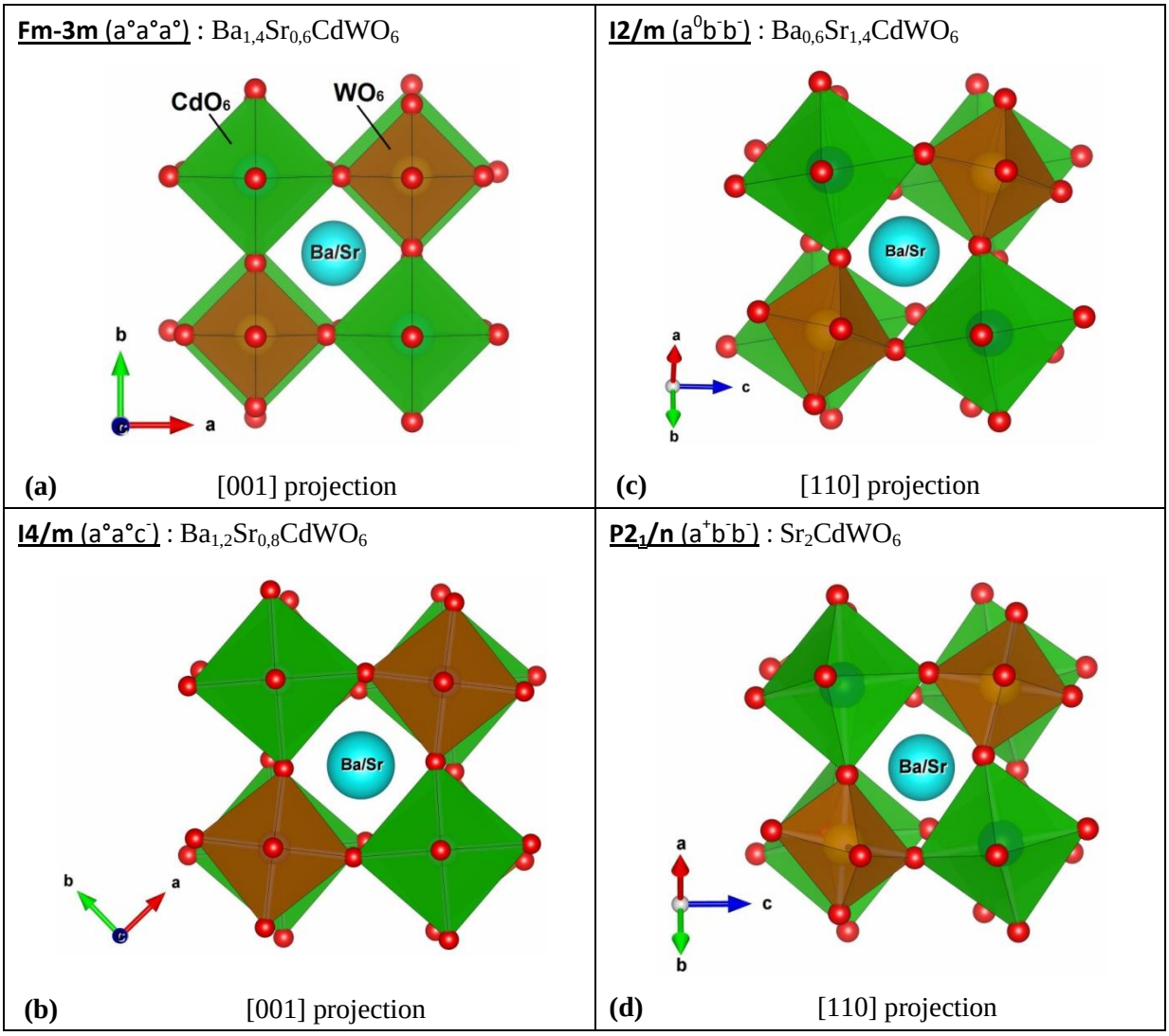

Figure IV.5: Illustrations of the tilting and rotation effect of the $(Cd/W)O_6$ octahedra for tetragonal and monoclinic symmetries (b, c and d) in $Ba_{2-x}Sr_xCdWO_6$ ($0 \leq x \leq 2$).

The tilt pattern of the octahedral units satisfies the $a^+b^-b^-$ tilt system in Glazer's notation [24, 25]. A [1 1 0] projection of the Sr_2CdWO_6 unit cell indicating the typical polyhedral arrangement and the tilt pattern is shown in Figure IV.5-(d).

On the other hand, the analysis of various inter-atomic distances (Table IV.6, 7, 8 and 9) shows that Ba and/or Sr atoms form Ba/SrO_{12} polyhedra with the Ba/Sr–O bond lengths around 2.9413Å for cubic compound ($0 \leq x \leq 0,6$), 2.9432Å for tetragonal (I4/m) compounds ($0.8 \leq x \leq 1$), 2.9298Å for monoclinic (I2/m) compounds ($1.2 \leq x \leq 1.6$) and 2.9213Å for monoclinic ($P2_1/n$) compounds ($1.8 \leq x \leq 2$). The Cd^{2+} and W^{6+} have octahedral coordination with the Cd–O bond lengths around 2.2867, 2.3313, 2.3137 and 2.3074 Å and the W–O bonds around 1.8620, 1.8533, 1.8793 and 1.8765 Å for cubic, tetragonal (I4/m), monoclinic (I2/m) and monoclinic ($P2_1/n$) structures, respectively.

Note that, the values taken for inter-atomic distances are means of inter-atomic distances of all the points of the same space group.

It seems that during the substitution of Barium by Strontium, notable variations in the values of these distances are noticed, this is due to the difference of the atomic rays of Ba^{2+} and Sr^{2+}, which causes a contraction of the crystalline structure and subsequently causes phase transitions. Indeed, it is possible to attribute some of these variations in inter-atomic distances, when they are considerable, to phase transitions, which is well noticed in the case of Cd-O distances. However, this contraction is less marked with respect to the monoclinic I2/m to monoclinic $P2_1/m$ transition.

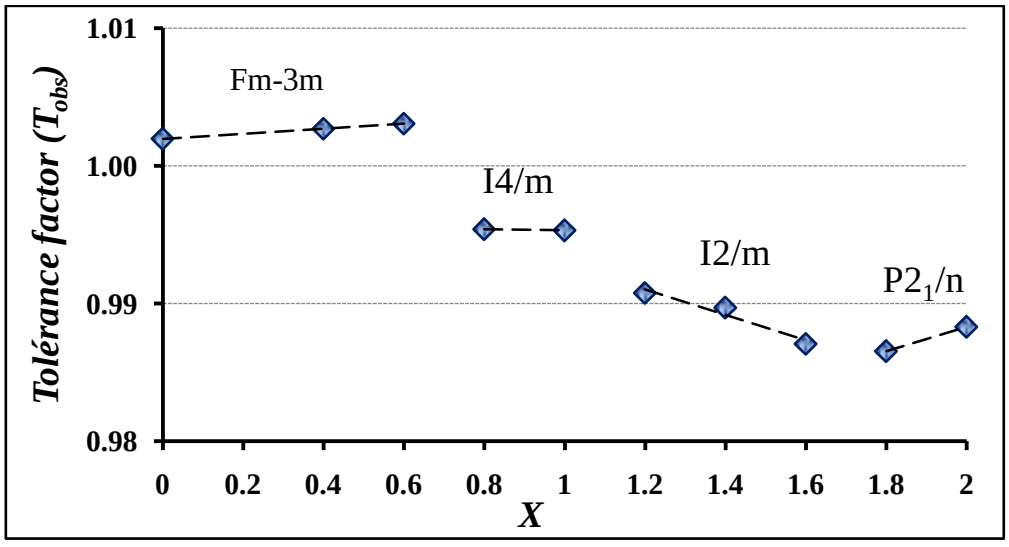

Figure IV.6: Observed tolerance factor (calculated from the distances obtained from the Rietveld refinements) as a function of the strontium amount in $Ba_{2-x}Sr_xCdWO_6$ ($0 \leq x \leq 2$).

Figure IV.6 shows the observed tolerance factor (calculated from the distances obtained from the Rietveld refinements) as a function of the strontium amount in $Ba_{2-x}Sr_xCdWO_6$. The phase transition from cubic to tetragonal, from tetragonal to monoclinic I2/m and from monoclinic I2/m to monoclinic $P2_1/n$, is well illustrated in the figure between the compositions $0.6 \leq x \leq 0.8$, $1 \leq x \leq 1.2$ and $1.6 \leq x \leq 1.8$ successively.

Table IV.6: Selected inter-atomic distances (Å) and [O-W-O] angles (°) for the cubic compositions in $Ba_{2-x}Sr_xCdWO_6$ ($0 \leq x \leq 0.6$) series at room temperature.

Cubic Fm-3m	**x = 0**	**x = 0.4**	**x = 0.6**
6× W-O	1.8997(27)	1.8626(16)	1.8449(22)
6× Cd-O	2.2700(22)	2.2949(16)	2.3047(22)
12× Ba/Sr-O	2.9542(15)	2.9477(11)	2.9432(15)
3× O-W-O	180	180	180
12× O-W-O	90	90	90

Table IV.7: Selected inter-atomic distances (Å) and [O-W-O] angles (°) for the tetragonal compositions in $Ba_{2-x}Sr_xCdWO_6$ ($0.8 \leq x \leq 1$) series at room temperature.

Tetragonal I4/m	**x = 0.8**	**x = 1**
2× W-O1	1.7244(32)	1.6680(30)
4× W-O2	1.9270(28)	1.9367(75)
<W-O>	1.8594(26)	1.8471(97)
2× Cd-O1	2.4208(32)	2.4606(30)
4× Cd-O2	2.2767(28)	2.2764(75)
<Cd-O>	2.3247(26)	2.3378(97)
4 × Ba/Sr-O1	2.9447(39)	2.9454(45)
4 × Ba/Sr-O2	3.2093(34)	3.2350(35)
4 × Ba/Sr-O2	2.6810(97)	2.6439(09)
<Ba/Sr-O>	2.9450(50)	2.9414(30)
1× O1-W-O1	180	180
8× O1-W-O2	90	90
4× O2-W-O2	90	90
2× O2-W-O2	180	180

Table IV.8: Selected inter-atomic distances (Å) and [O-W-O] angles (°) for the monoclinic I2/m compositions in $Ba_{2-x}Sr_xCdWO_6$ ($1.2 \leq x \leq 1.6$) series at room temperature.

Monoclinic I2/m	**x = 1.2**	**x = 1.4**	**x = 1.6**
2× W-O1	1.7880(32)	1.8663(25)	1.9064(01)
4× W-O2	1.9280(99)	1.8940(16)	1.8548(03)
<W-O>	1.8813(27)	1.8848(30)	1.8720(16)
2× Cd-O1	2.4313(31)	2.4484(27)	2.3536(05)
4× Cd-O2	2.2465(90)	2.2511(20)	2.2976(05)
<Cd-O>	2.3081(24)	2.3168(32)	2.3163(17)
2 × Ba/Sr-O1	2.9524(62)	2.9780(78)	2.9737(72)
1 × Ba/Sr-O1	3.3882(65)	3.5828(39)	3.4280(10)
1 × Ba/Sr-O1	2.4831(65)	2.2792(40)	2.3720(10)
2 × Ba/Sr-O2	2.7913(67)	2.7364(98)	2.6228(02)
2 × Ba/Sr-O2	3.2343(53)	3.1260(83)	3.1320(96)
2 × Ba/Sr-O2	3.0713(58)	3.0954(90)	3.2120(00)
2 × Ba/Sr-O2	2.6248(74)	2.7208(05)	2.6995(06)
<Ba/Sr-O>	2.9350(76)	2.9313(81)	2.9233(60)
1 × O1-W-O1	180	180	180
4 × O1-W-O2	90	96(2)	92(2)
4 × O1-W-O2	90	84(2)	88(2)
2 × O2-W-O2	180	180	180
2 × O2-W-O2	93(2)	94(2)	94(14)
2 × O2-W-O2	86.7(18)	86(2)	86(16)

Table IV.9: Selected inter-atomic distances (Å) and [O-W-O] angles (°) for the monoclinic $P2_1/n$ compositions in $Ba_{2-x}Sr_xCdWO_6$ ($1.8 \leq x \leq 2$) series at room temperature.

Monoclinic P21/n	**x = 1.8**	**x = 2**
2× W-O1	1.8672(13)	1.8052(31)
2× W-O2	1.9218(95)	1.8968(98)
2× W-O3	1.8661(40)	1.9019(40)
<W-O>	1.8850(89)	1.8680(91)
2× Cd-O1	2.2765(96)	2.3215(32)
2× Cd-O2	2.2932(09)	2.3192(11)
2× Cd-O3	2.3535(42)	2.2810(42)
<Cd-O>	2.3077(88)	2.3072(93)
<4 × Ba/Sr-O1>	2.9131(52)	2.9086(17)
<4 × Ba/Sr-O2>	2.9217(33)	2.9213(35)
<4 × Ba/Sr-O3>	2.9398(43)	2.9235(23)
<Ba/Sr-O>	2.9248(56)	2.9178(68)
1 × O1-W-O1	180	180
2 × O1-W-O2	91.6(17)	90.2(17)
2 × O1-W-O2	88.4(14)	89.8(16)
2 × O1-W-O3	77.3(15)	81.1(18)
2 × O1-W-O3	102.7(18)	98.9(19)
1 × O2-W-O2	180	180
2 × O2-W-O3	91.3(15)	95.4(17)
2 × O2-W-O3	88.7(15)	84.6(15)
1 × O3-W-O3	180	180

4. Group theory analysis of structural Raman-active modes

4.1 Raman-active modes in $Ba_{2-x}Sr_xCdWO_6$, ($0 \leq x \leq 2$) solid solutions

The site symmetry group analysis performed for the cubic structures Fm-3m, tetragonal I4/m and monoclinic I2/m and $P2_1/n$ leads to the following irreducible representations [26]:

- For the cubic structures Fm-3m:

$$\mathbf{\Gamma} = A_{1g}\,(R) + E_g\,(R) + 2F_{2g}\,(R) + 4F_{1u}\,(IR) + F_{1u}\,(ac)$$

- For the tetragonal structures I4/m:

$$\mathbf{\Gamma} = 1A_g\,(R) + 1B_g\,(R) + 2\,{}^1E_g\,(R) + 2\,{}^2E_g\,(R) + 3A_U\,(IR) + 3\,{}^1E_u\,(IR) + 3\,{}^2E_u\,(IR) + A_u\,(ac) + {}^1E_u\,(ac) + {}^2E_u\,(ac)$$

- For the monoclinic structures I2/m:

$$\mathbf{\Gamma} = 5A_g\,(R) + 4B_g\,(R) + 5A_u\,(IR) + 7B_u\,(IR) + A_u\,(ac) + 2B_u\,(ac)$$

- For the monoclinic structures $P2_1/n$:

$$\mathbf{\Gamma} = 3A_g\,(R) + 3B_g\,(R) + 8A_u\,(IR) + 7B_u\,(IR) + A_u\,(ac) + 2B_u\,(ac)$$

Where the notation stands for: R: Raman-active modes, IR: infrared active modes and ac: acoustic modes.

Among all of these modes predicted by the theory, only A_g, B_g, E_g, A_{1g}, ${}^1E_g$, ${}^2E_g$ and T_{2g} are Raman-active modes. Thus, at room temperature there are four expected active Raman modes for the cubic symmetry, six active Raman modes are expected for the tetragonal symmetry I4/m, nine active Raman modes are expected for the monoclinic symmetry I2/m, finally six active Raman modes are expected for the monoclinic symmetry $P2_1/n$. Most of the bands are weak; there are three strong bands and they are observed around $118cm^{-1}$, $419cm^{-1}$ and $858cm^{-1}$ for Ba_2CdWO_6 and around $140cm^{-1}$, $450cm^{-1}$ and $836cm^{-1}$ for Sr_2CdWO_6.

4.2 Raman spectroscopy analysis at room temperature of $Ba_{2-x}Sr_xCdWO_6$; ($0 \leq x \leq 2$)

The Raman spectra of $Ba_{2-x}Sr_xCdWO_6$ ($0 \leq x \leq 2$) recorded at ambient conditions are illustrated in Figure IV.7. In Figure IV.8-(a) the enlarged section show the modes centered at $135cm^{-1}$ for the monoclinic symmetries. For all the composition ranges (cubic tetragonal and monoclinic), the observed Raman modes can be classified into three general families of lattice vibrations: Ba^{2+}/Sr^{2+} translations, as well as translational and rotational modes of the WO_6-

octahedra, at frequencies below 200cm^{-1}; O-W-O bending vibrations, in the 200-500 cm^{-1} region; and W–O stretching modes, at frequencies over 500cm^{-1}.

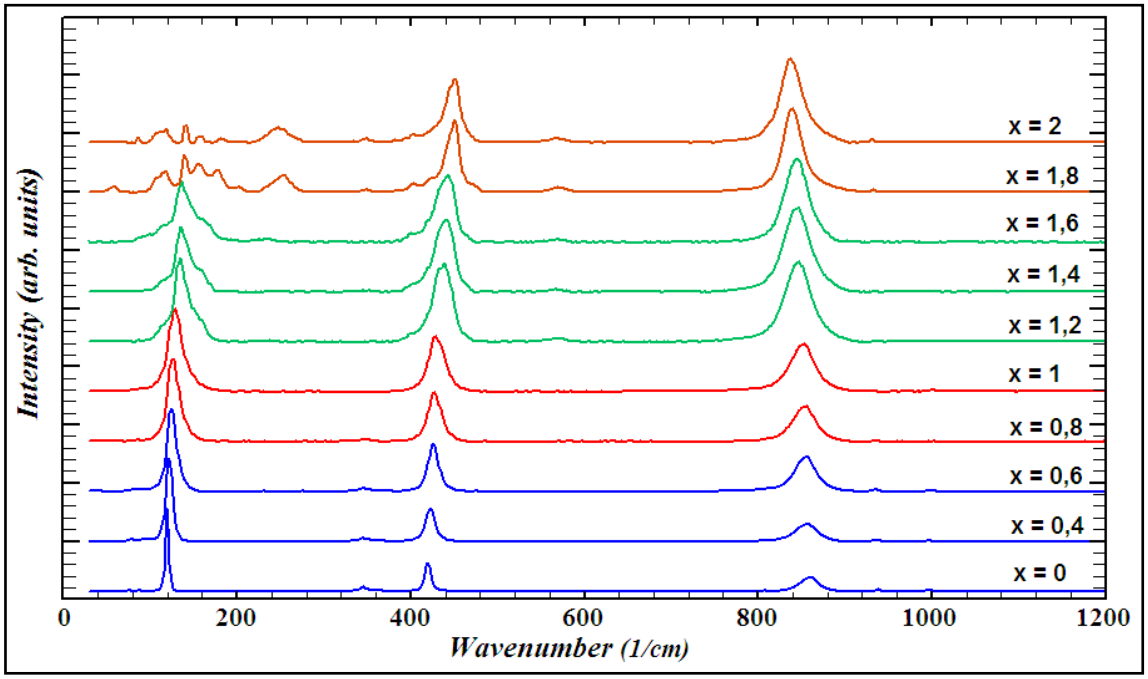

Figure IV.7: Raman spectra of $Ba_{2-x}Sr_xCdWO_6$ ($0 \leq x \leq 2$) recorded at ambient conditions.

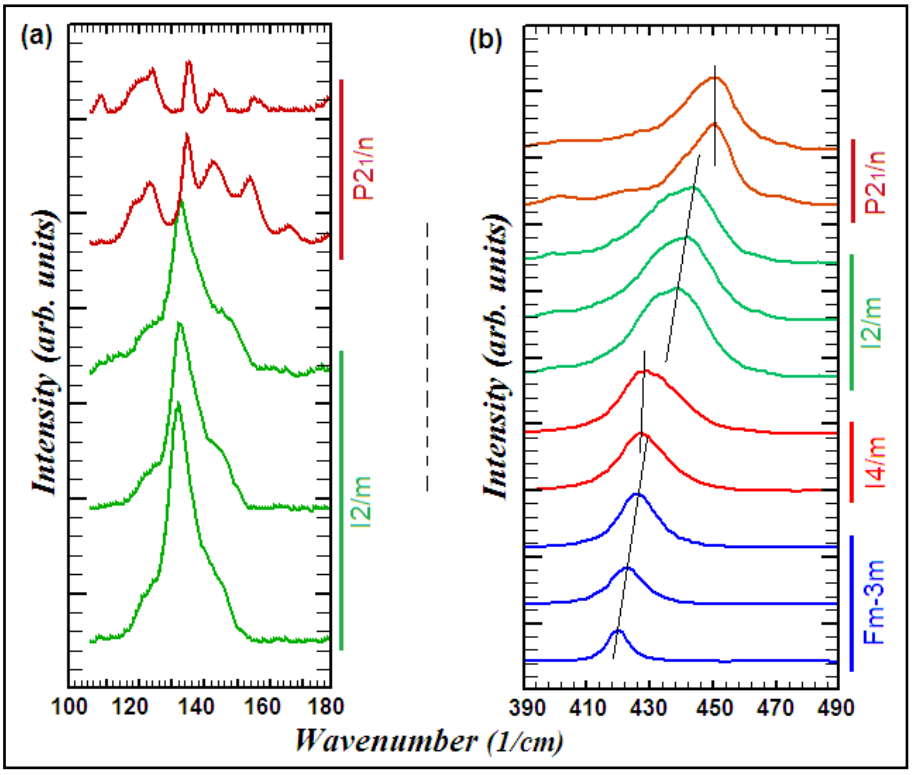

Figure IV.8: Enlargement of the modes centered at 135 cm^{-1} for the monoclinic symmetries I2/m and $P2_1/n$ (a) and discontinuous alteration of the slope of the modes centered at 435cm^{-1} corresponding to the phase transitions (b).

The analysis of Raman spectra recorded at room condition of double perovskite compounds $Ba_{2-x}Sr_xCdWO_6$ ($0 \leq x \leq 2$) shows, as a function of the composition, three phase transitions. In Figure IV.8-(b) we illustrated the changes of the slope of the Raman modes centred at 435cm^{-1}, while their positions as a function of the amount of strontium in the compositions have been presented in Figure IV.9-(a).

The intensity of the modes centred at 435 cm^{-1}, the Full Width at Half Maximum (FWHM) of the modes centred at 845 cm^{-1} and the intensity ratio I_{845}/I_{130} were presented in Figure IV.9-(b, c, d).

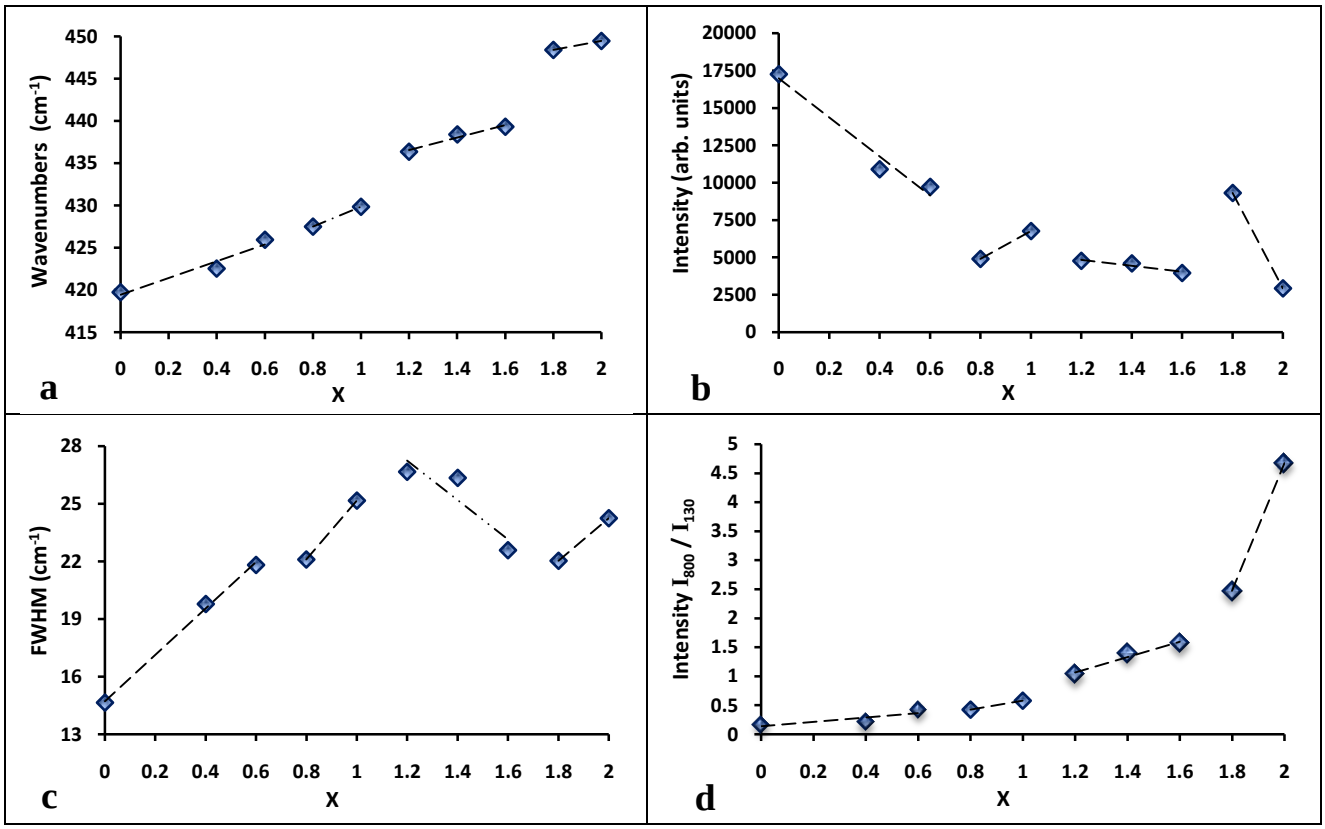

Figure IV.9: Raman modes (a) and Intensity of the modes centered at 435cm^{-1} (b), the FWHM of the modes centered at 845 cm^{-1} (c) and Intensity ratio I_{800}/I_{130} (d) as a function of the composition x of $Ba_{2-x}Sr_xCdWO_6$ ($0 \leq x \leq 2$). The symmetry transition shows considerable changes in composition dependence of the modes.

In Figure IV.9-(b, c, d), clear changes were observed in the curves showing the cubic to tetragonal phase transition between x = 0.6 and 0.8, the tetragonal to monoclinic I2/m phase transition between x=1 and x=1.2 and the monoclinic I2/m to monoclinic $P2_1/n$ phase transition between x=1.6 and x=1.8 and thus confirming the Rietveld refinements studies.

5. Conclusion

In this study, using the X-ray diffraction and Raman spectroscopy techniques, we report on the composition induced phase transition in $Ba_{2-x}Sr_xCdWO_6$ ($0 \leq x \leq 2$) double perovskite oxides. While increasing strontium amount at room temperature, three phase transition are observed as a function of composition. From cubic Fm-3m to tetragonal I4/m phase, from tetragonal I4/m to monoclinic I2/m phase and from monoclinic I2/m to monoclinic $P2_1/n$ phase; both Rietveld refinements and Raman studies showed that the first phase transition occurs between x=0.6 and x=0.8; the second phase transition is observed between x=1 and x=1.2 and the third phase transition is observed between x=1.6 and x=1.8. For these series, structural symmetry changes are clearly revealed by changes in the compositional linear dependencies of the modes which exhibit a discontinuous alteration of their slopes upon the transition.

References

[1] P.W. Barnes, M.W. Lufaso, P.M. Woodward, Acta Crystallogr. B 62 (2006) 384.

[2] S. Meenakshi, V. Vijayakumar, S.N. Achary, A.K. Tyagi, J. Phys. Chem. Solids 72 (2011) 609.

[3] K.-I. Kobayashi, T. Kimura, H. Sawada, K. Terakura, Y. Tokura, Nature 395 (1998) 677.

[4] K. -I. Kobayashi, T. Kimura, H. Sawada, K. Terakura, Y. Tokura, Phys. Rev. B59 (1999), 11159.

[5] T. Burnus, Z. Hu, H. H. Hsieh, V. L. J. Joly, P. A. Joy, M. W. Haverkort, H. Wu, A. Tanaka, H.-J. Lin, C. T. Chen and L. H. Tjeng, Physical Review B 77 (2008) 125-124.

[6] J. J. Capponi, C. Chaillout, A. W. Hewat, P. Lejay, M. Marezio, N. Nguyen, B. Raveau, J. L. Soubeyroux, J. L. Tholence and R. Tournier. Europhys. Lett. 3 (1987) 1301.

[7] J. Rodriguez-Carvajal, Collected Abstracts of Powder Diffraction Meeting, (Toulouse, France), 127 (1990).

[8] Digvijay N. Singha, T. P. Sinhab, D. K. Mahato, Mater. Today 4 (2017) 5640–5646.

[9] T. Roisnel, J. Rodriguez-Carvajal, Mater. Sci. Forum 378-381 (2001) 118.

[10] A.Boultif, D.Louër, J.Appl.crystallogr. 24 (1991) 987.

[11] D.D. Khalyavin, Jiaping Han, A.M.R. Senos, P.Q. Mantas, J. Mater. Res. 18 (2003) 2600.

[12] O. Sahnoun, H. Bouhani-Benziane, M. Sahnoun, M. Driz, C. Daul, Comput. Mater. Sci. 77 (2013) 316–321.

[13] M. Gateshki, J.M. Igartua, E. Hernandez-Bocanegra, J. Phys.: Cond. Matter 15 (2003) 6199–6217.

[14] Bouchaib Manoun, Josu M. Igartua, Peter Lazor, Amine Ezzahi, J. of Molecular Structure 1029 (2012) 81–85.

[15] M. Gateshki, J.M. Igartua, A. Faik, J. Solid State Chem. 180 (2007) 2248–2255.

[16] A. Boultif, D. Louër, J. Appl. Crystallogr. 24 (1991) 987.

[17] J.C. Sczancoski, L.S. Cavalcante, M.R. Joya, J.W.M. Espinosa, P.S. Pizani, J.A. Varela, E. Longo. Journal of Colloid and Interface Science 330 (2009) 227–236.

[18] Purohit, A., Chander, S., Patel, S. L., Rangra, K. J., & Dhaka, M. S. Physics Letters A, 381(22) (2017) 1910–1914.

[19] Y. Tamraoui, B. Manoun, F. Mirinioui, R. Haloui, P. Lazor. Journal of Alloys and Compounds 603 (2014) 86–94.

[20] R. Haloui, Bouchaib Manoun, Y. Tamraoui, S. Louihi, M. Jahid, A. El Hachmi, R. Abkar, M. A. El aamrani, O. Ait Sidi Ahmed, L. Bih and P. Lazor. J. Appl. Surf. Interface 1 (1-3) (2017) 35-48.

[21] W.T. Fu, S. Akerboom, D.J.W. IJdo. J. Alloys Compd. 476 (2009) L11–L15.

[22] W.T. Fu, Y.S. Au, S. Akerboom, D.J.W. IJdo. Journal of Solid State Chemistry 181 (2008) 2523–2529.

[23] F. Mirinioui, Bouchaib Manoun, Y. Tamraoui, P. Lazor. Journal of Solid State Chemistry 232 (2015) 182-192.

[24] A.M. Glazer, Acta Cryst. A 31 (1975) 756.

[25] A.M. Glazer, Acta Crystallogr. B 28 (1972) 3384.

[26] E. Kroumova, M.I. Aroyo, J.M. Perez-Mato, A. Kirov, C. Capillas, S. Ivantchev, H. Wondratschek, Phase Transit. 76 (2003) 155-170.

General conclusion

Perovskite-type oxides belong to the Family of mixed metal oxides; they are of considerable importance with respect to both practical application and basic researches. Two types of perovskite are found:

That represented by the formula ABO_3, wherein two or more metal cations are randomly distributed in sites A or B. For that effect, they are called disordered perovskite.

That represented by the formula $A_2BB'O_6$ or $AA'BB'O_6$, are called as ordered perovskites because they have distinct ordering in sublattice of metal cations.

So far, the investigations on physical and chemical properties of ordered perovskites are very limited as compared with disordered perovskites. For this reason, the systematic investigation on ordered perovskites with respect to synthesis, structure and properties will greatly contribute to enlarge the chemistry and physics of perovskite-type oxides. This present work complements continuing efforts undertaken by the scientific community to improve our knowledge about the perovskite-type oxides of the formula $AA'BB'O_6$.

In the present study, a systematic series of W- and Mo-containing perovskites have been synthesized and their crystal structures have been investigated using X-ray diffraction technique. Moreover, using this technique and Raman spectroscopy analysis at ambient and at high temperature, a description of the crystallographic behavior of the phases obtained as a function of composition and as a function of temperature was detailed.

In Chapter I, the crystal structure, physical and structural properties of perovskite type oxides published in the bibliography, have been summarized. The purposes of the present study have been also described.

In Chapter II, we have detailed the experimental procedure followed during the synthesis of the samples, as well as the experimental techniques, the different structural characterization method and the corresponding material used in this study.

In Chapter III, new solid solutions $Ba_{2-x}Sr_xMeMoO_6$; $0 \leq x \leq 2$ (Me= Ni, Mg) of double perovskite type were synthesized by the high temperature solid state reaction and firing

methods, and characterized using techniques of X-ray diffraction and Raman spectroscopy. The crystal structures were determined by Rietveld refinement method laboratory using X-Ray powder diffraction data. As a function of composition, up on increasing the strontium content, the samples exhibit a sequence of two phase transitions: from cubic (Fm-3m) to tetragonal (I4/m) to monoclinic structural phases (I2/m):

- For $Ba_{2-x}Sr_xNiMoO_6$; $0 \leq x \leq 2$: the first phase transition (Fm-3m $\rightarrow$ I4/m) occurs between x =1.3 and x = 1.5, while the second phase transition (I4/m $\rightarrow$ I2/m) is observed in the range of x between x =1.8 and x = 2.

- For $Ba_{2-x}Sr_xMgMoO_6$; $0 \leq x \leq 2$: the first phase transition (Fm-3m $\rightarrow$ I4/m) is revealed in the range of x between x =0.9 and x = 1. The second phase transition (I4/m $\rightarrow$ I2/m) occurs between x =1.5 and x = 1.75.

Furthermore, increasing the temperature for the tetragonal and monoclinic compositions of the solution $Ba_{2-x}Sr_xMeMoO_6$; $0 \leq x \leq 2$ (Me= Ni, Mg), manifests the I2/m to I4/m and the I4/m to Fm-3m phase transitions:

- For $Ba_{2-x}Sr_xNiMoO_6$; the tetragonal to cubic phase transition is observed at around 130°C, 190°C, 334°C and 474°C for x =1,5, x=1,6, x=1,8 and x=2 successively. However, for the solution solid of x=2, a second phase transition (the monoclinic I2/m to tetragonal I4/m) is observed at about 175°C.

- For $Ba_{2-x}Sr_xMgMoO_6$; the tetragonal to cubic phase transition is observed at around 105°C, 395°C, 436°C and 466°C for x =1, x=1,5, x=1,75 and x=2 successively. The phase transition monoclinic to tetragonal is revealed at 96°C and at around 205°C for the compositions of x=1.75 and x=2 successively.

In Chapter IV, we have studied the effect of the composition on the phase composition of the new solid solutions $Ba_{2-x}Sr_xCdWO_6$; ($0 \leq x \leq 2$) of double perovskite type, synthesised by the high temperature solid state reaction and firing methods. The Rietveld refinements, using

the X-ray powder diffraction (XRD) data at ambient temperature, shows that, as a function of composition, up on increasing the strontium content, the samples exhibit a sequence of tree phase transitions: from cubic (Fm-3m) to tetragonal (I4/m) to monoclinic (I2/m) to monoclinic structural phases ($P2_1/n$). All the results attained by Rietveld refinements and confirmed by Raman spectroscopy at ambient temperature showed that the first phase transition occurs between x=0.6 and x=0.8; the second phase transition is observed between x=1 and x=1.2 and the third phase transition is observed between x=1.6 and x=1.8.

It remains to be noted that all the results obtained in this work represent a solid and fundamental basis for other studies related to physical and chemical properties of perovskite-type oxides. Although, the understanding of such a physical or chemical property and of all the factors that can influence it, always requires an intensive analysis of crystalline structure.

The results obtained in this study will hopefully contribute to the further development of chemistry of perovskite-type oxides, solid-state chemistry and other related fields.

For the future works, they will be focused on the understanding the relationship between the structure and physical properties. We will study the physical properties for all our compounds of the series involved in this thesis.

Publications and Communications list_____

❖ **Publications** :

1. **M.A. EL aamrani**, B. Manoun, R. Abkar, Y. Tamraoui, F. Mirinioui, A. El Hachmi, M. Azrour, S. Benmokhtar and P. Lazor. Synthesis, crystal structure and temperature induced phase transition in $Ba_{1/5}Sr_{4/5}NiMoO_6$ double perovskite oxide: Study by X-ray diffraction and Raman spectroscopy. Journal of Applied Surfaces and Interfaces 2 (1-3) (2017) 27-33
2. Abdelhadi El hachmi, Bouchaib Manoun, Y. Tamraoui, F. Mirinioui, R. Abkar, **M.A. EL aamrani**, M. Sajieddine and P. Lazor. Temperature induced structural phase transition in $Sr_{3-x}Ca_xFe_2TeO_9$ ($0 \leq x \leq 1$) probed by Raman and Mossbauer techniques. Journal of Molecular Structure 1141 (2017) 484-494
3. R. Haloui, B. Manoun, Y. Tamraoui, S. Louihi, M. Jahid, A. El Hachmi, R. Abkar, **M. A. El aamrani**, O. Ait Sidi Ahmed, L. Bih and P. Lazor. Crystal structure and phase transitions in new series of double perovskite oxides $Ba_{2-x}Sr_xCaTeO_6$ ($0 \leq x \leq 2$): X-ray diffraction and Raman spectroscopy studies. Journal of Applied Surfaces and Interfaces 1(1-3) (2017) 35-48
4. Abdelhadi El Hachmi, Y. Tamraoui, Bouchaib Manoun, R. Haloui, **M.A. Elaamrani**, I. Saadoune, L. Bih, and P. Lazor. Synthesis and Rietveld refinements of new ceramics $Sr_2CaFe_2WO_9$ and $Sr_2PbFe_2TeO_9$ perovskites. Powder Diffraction 33 (2018) (2)
5. **M.A. Elaamrani,** Bouchaib Manoun, Y. Tamraoui, F. Mirinioui, A. El Hachmi, and P. Lazor. Investigations of crystal structure in new series of Molybdenum double perovskites oxides $Ba_{2-x}Sr_xNiMoO_6$ ($0 \leq x \leq 2$): X-ray diffraction and Raman spectroscopy studies of temperature and composition induced phase transitions. Submitted to Journal of molecular structure.
6. **M.A. El aamrani**, Bouchaib Manoun, R. Haloui, Y. Tamraoui, F. Mirinioui, A. El Hachmi, and P. Lazor. Crystal structure and phase transition in the new series of double perovskites oxide $Ba_{2-x}Sr_xCdWO_6$ ($0 \leq x \leq 2$), X-ray diffraction and Raman spectroscopy studies. Submitted to journal of alloys and compounds.

❖ **Communications:**

1. M. A. El Aamrani, Bouchaib Manoun, R. Abkar, Y. Tamraoui, F. Mirinioui, and P. Lazor, X-Ray Diffraction and Raman spectroscopy studies of composition induced phase transitions in $Ba_{2-x}Sr_xCdWO_6$, 5eme édition de la journée Doctorant, CEDoc Sciences et Techniques, Université Hassan 1er, FST Settat, **30 Mars 2017**.

2. M. A. El Aamrani, Bouchaib Manoun, F. Mirinioui, Y. Tamraoui, R. Abkar, A. Elhachmi, S. Benmokhtar and P. Lazor, Raman investigation of $Ba_{2-x}Sr_xNiMoO_6$ double perovskite oxides, EST-Berrechid, **11 Mai 2016**.

3. F. Mirinioui, B. Manoun, Y. Tamraoui, R. Haloui, A. Elhachmi, M. A. EL Aamrani, R. Abkar and P. Lazor, x-ray diffraction and raman spectroscopy studies of temperature and nickel substitution effects on the phase transitions in the $Co_{3-x}Ni_xTeO_6$ double perovskites oxides, Journée scientifique sur les matériaux avancés : Applications et Devenir, Faculté polydisciplinaire de Khouribga, **2 Juin 2016**.

4. M. A. El Aamrani, Bouchaib Manoun, F. Mirinioui, Y. Tamraoui, R. Abkar, A. Elhachmi, S. Benmokhtar and P. Lazor, crystal structure stability of the series $Ba_{2-x}Sr_xNiMoO_6$ double perovskite oxides, Journée scientifique sur les matériaux avancés : Applications et Devenir, Faculté polydisciplinaire de Khouribga, **2 Juin 2016**.

5. A. Elhachmi, B. Manoun, Y. Tamraoui, F. Mirinioui, M. A. Elaamrani, R. Abkar, S. Louihi and P. Lazor, crystal structure of $Sr_2CaFe_2MO_9$ (M=W, Mo) probed by x ray diffraction and raman spectroscopy studies, Journée scientifique sur les matériaux avancés : Applications et Devenir, Faculté polydisciplinaire de Khouribga, **2 Juin 2016**.

6. R. Abkar, B. Manoun, F. Mirinioui, Y. Tamraoui, A. ELHachmi, M. A. El Aamrani, S. Benmokhtar and P. Lazor, crystal structure stability and phase transitions in $Ba_{2-x}Sr_xMgMoO_6$ ($0 \leq x \leq 2$) double perovskite oxides. Journée scientifique sur les matériaux avancés : Applications et Devenir, Faculté polydisciplinaire de Khouribga, **2 Juin 2016**.

7. Abdelhadi El Hahimi, Bouchaib Manoun, Y. Tamraoui, F. Mirinioui, R. Abkar, S, Louihi, M.A. El Aamrani and P. Lazor. Ca-doped double perovskite $Sr_2CaFe_2WO_9$ investigated by x-ray diffraction and Raman spectroscopy, International meeting on Nano and Smart Materials for Renewable Energy NASMERE, **28-29 Avril 2016.**

8. Moulay Abdelaziz El Aamrani, B. Manoun, A. Elhachmi , R. Abkar, Y. Tamraoui, F. Mirinioui, S. Benmokhtar and Lazor, Raman investigation of $Ba_{2-x}Sr_xNiMoO_6$ double perovskite oxides, 4eme édition de la journée Doctorant, CEDoc Sciences et Techniques, Université Hassan 1er, FST Settat, **20-21 Avril 2016**.

9. Abdelhadi Elhachmi, B. Manoun, Y. Tamraoui, F. Mirinioui, R. Abkar, S. Louihi, M. A. El Aamarni and P. Lazor, X-Ray Diffraction and Raman spectroscopy studies of Ca-Substituted double perovskite compound $Sr_2CaFe_2MoO_9$, 4eme édition de la journée Doctorant, CEDoc Sciences et Techniques, Université Hassan 1er, FST Settat, **20-21 Avril 2016**.

10. M. A. El Aamrani, Bouchaib Manoun, F. Mirinioui, Y. Tamraoui, R. Abkar, A. Elhachmi, S. Benmokhtar and P. Lazor, Raman investigation of $Ba_{2-x}Sr_xNiMoO_6$ double perovskite oxides, Journée scientifique des doctorants LS3M, Faculté polydisciplinaire de Khouribga, **3 Mars 2015**.

11. Abdelhadi Elhachmi, Bouchaib Manoun, Y. Tamraoui, F. Mirinioui, R. Abkar, M.A. EL aamrani and P. Lazor, X-Ray Diffraction and Raman spectroscopy studies of temperature induced phase transitions in $Sr_{2,5}Ca_{0,5}Fe_xTeO_9$ triple perovskite, Journée scientifique des doctorants LS3M, Faculté polydisciplinaire de Khouribga, **3 Mars 2015**.

12. R. Abkar, Bouchaib Manoun, A. El Aamrani, A.Elhachimi, Y. Tamraoui, F. Mirinioui, S.Benmokhtar and P. Lazor, vibrational spectroscopy study of $Ba_{2-x}Sr_xMgMoO_6$, Journée scientifique des doctorants LS3M, Faculté polydisciplinaire de Khouribga, **3 Mars 2015**.

13. A. EL Aamrani. Bouchaib Manoun, R. Abkar. Y. Tamraoui. F. Mirinioui. S. Benmokhtar and P. Lazor, X-ray diffraction and Raman spectroscopy studies of temperature induced phase transition in $Ba_{0.2}Sr_{1.8}NiMoO_6$, $4^{ème}$ Journée Argile et Développement Durable, Faculté des Sciences Tétouan, **04 Juin 2015**.

14. M. A. El Aamrani, Bouchaib Manoun, F. Mirinioui, Y. Tamraoui, R. Abkar, A. Elhachmi, S. Benmokhtar and P. Lazor, X-ray diffraction and Raman spectroscopy studies of temperature induced phase transition in $Ba_{0.2}Sr_{1.8}NiMoO_6$, $2^{ème}$ Journée de l'environnement. Impact de la Pollution (Eau, Air et Sol) sur la Population (JEIPP), Chambre de commerce Kénitra, **23 Mai 2015**.

15. A. EL Aamrani. Bouchaib Manoun, R. Abkar. Y. Tamraoui. F. Mirinioui. S. Benmokhtar and P. Lazor, X-ray diffraction and Raman spectroscopy studies of temperature and composition induced phase transitions in $Ba_{0.4}Sr_{1.6}NiMoO_6$, Crystallography for the next generation-The legacy of IYCR, Hassan II Academy, **22-24 Avril 2015**.

16. Abdelhadi Elhachmi, Bouchaib Manoun, Y. Tamraoui, F. Mirinioui, R. Abkar, M.A. EL aamrani and P. Lazor, Phase transition in heated $Sr_2CaFe_2TeO_9$ perovskite oxides probed by X-Ray diffraction and Raman spectroscopy, IIIèmes Journées Internationales «Matériaux et Environnement», FSTS **18-19 mars 2015**.

17. A. EL Aamrani. Bouchaib Manoun, R. Abkar. Y. Tamraoui. F. Mirinioui. S. Benmokhtar and P. Lazor, X-ray diffraction and Raman spectroscopy studies of temperature and composition induced phase transitions in $Ba_{0.4}Sr_{1.6}NiMoO_6$, IIIèmes Journées Internationales «Matériaux et Environnement», FSTS **18-19 mars 2015**.

18. R. Abkar, Bouchaib Manoun, A. El Aamrani, A.Elhachimi, Y. Tamraoui, F. Mirinioui, S.Benmokhtar and P. Lazor, x-ray diffraction and raman spectroscopy studies of $Ba_{0.5}Sr_{1.5}MgMoO_6$, IIIèmes Journées Internationales «Matériaux et Environnement», FSTS **18-19 mars 2015**.

19. El Aamrani, Bouchaib Manoun, R. Abkar, Y. Tamraoui, F. Mirinioui, S. Benmokhtar, and P. Lazor. X-ray diffraction and Raman spectroscopy studies of temperature and composition induced phase transitions in $Ba_{2-x}Sr_xNiMoO_6$. Congrès international "Functionam Materials and their Technological Aapplications (**CIMFAT 2014**)". Ecole Nationale Supérieur de Casablanca **24-25 octobre 2014**.

20. Bouchaib Manoun, A. Elaamrani, R. Abkar, F.Mirinioui and Y. Tamraoui. Structural investigation of $BaSrMgMoO_6$ double perovskite oxide. 1er Congrès de Génie Civil, Ingénierie Structurelle & Environnement. FST de Settat, **25-26 Juin 2014.**

21. R. Abkar, B. Manoun, A. Elaamrani, F.Mirinioui and Y. Tamraoui. Crystal structure as determined by the Rietveld refinement of $BaSrNiMoO_6$. 1er Congrès de Génie Civil, Ingénierie Structurelle & Environnement. FST de Settat, **25-26 Juin 2014.**